UNIVERSITE DE LIEGE
FACULTE DES SCIENCES APPLIQUEES
Département ArGEnCo

The use of *a priori* information in electrical resistivity tomography for salt water intrusion studies at the Belgian coast

HERMANS Thomas

Master thesis presented to obtain the master's degree of

Ingénieur civil des Mines et Géologue

Supervisor

NGUYEN Frédéric

Data contained in this master thesis are confidential. Each consultation must be submitted to the supervisor's approval.

Les données contenues dans ce travail sont confidentielles. Toute consultation doit être soumise au consentement du promoteur.

Academic year 2009–2010

Acknowledgments

First of all, I would like to thank my promoter, Professor Frédéric Nguyen, for the interest shown for this master thesis. He permitted me to accomplish an interesting work on a very exciting subject. Since the beginning, he has always followed the advance of the work and has given lots of advices and suggestions. I also thank him for his applied proofreading.

I also want to thank all the members of the jury, Professor Alain Dassargues, Serge Brouyère, Professor Luc Lebbe and Alexander Vandenbohede for the attention expressed, before, during and after the accomplishment of this master thesis. More particularly, I am very grateful to MM. Lebbe and Vandenbohede for accepting my internship at Ghent University and helping me to discover the issue of salt water intrusion in the Nature Reserve the Westhoek. I think that this collaboration has allowed me to provide a better work.

I thank "IVA Maritieme Dienstverlening en Kust, Afdeling Kust" and "Agentschap Natuur en Bos" for giving their permission to do the fieldwork and use the already collected data.

I would also like to thank the whole team of applied geophysics, Jean Beaujean, David Caterina and Tanguy Robert for their help, their advices, their explanations and their interest in my work.

I have to say my biggest "thank you very much" to Olivier Bouhon, Carolien Courtens, Jean Beaujean and Alexander Vandenbohede. They came on the field with me to collect the data. Without their help, this master thesis would have remained a project.

It was also very kind of the research team of Professor Andreas Kemna (University of Bonn) to let me use their high-performance equipment. In addition, they allowed me to use their inversion code and to modify it for my specific case. I thank Roland Martin for his help to solve the convergence problems.

I also thank Mr. Godard for the proofreading of the English language.

Last but not least, I want to thank all my family, especially Kim for supporting and encouraging me during the last five years.

Abstract

Two artificial sea inlets were built in the nature reserve "The Westhoek". Consequently, sea water infiltrated in the dune aquifer filled with fresh water and exploited by a water company. Due to the presence of a clayey layer with a low hydraulic conductivity, the vertical flow of salt water was stopped, leading to a horizontal flow outside the infiltration ponds. Electrical resistivity tomographies were carried out, in addition to borehole electromagnetic measurements. The latter were used to calculate a vertical variogram, characteristic of the study site. Then, a geostatistical constraint was imposed as a regularization tool to solve the inverse problem, with a covariance matrix based on the variogram. The important points of this type of regularization were first highlighted by several synthetic cases. The main conclusions were that the choice of a homogeneous prior model seemed judicious in this case, whereas the lack of information to determine the horizontal variogram was not a major issue. Inversion results enabled to determine the extension of the salt water plume laterally, in depth, but also in terms of total dissolved solid content (TDS). These observations are in agreement with the hydrogeological situation of the site. A comparison with borehole data showed that the results are much more satisfying than a traditional smoothness constraint used as a regularization tool. Prior information included in the inversion process enabled to improve the resolution, even if traditional image appraisal tools failed to quantify this contribution.

Keywords : salt water intrusion, Belgian coast, electrical resistivity, electromagnetic method, geostatistical constraint, inversion process, resolution.

Résumé

Deux bras de mer artificiels ont été creusés dans les dunes de la réserve naturelle du Westhoek. Par conséquent, de l'eau de mer s'est infiltrée dans l'aquifère d'eau douce située au sein des dunes et exploitée pour la production d'eau potable. A cause de la présence d'une couche argileuse peu perméable, le mouvement vertical de l'eau salée a été stoppé, entrainant un flux horizontal vers l'extérieur du bassin d'infiltration. Des tomographies électriques ont été réalisées en complément de mesures électromagnétiques en forage. Ces dernières ont été utilisées pour calculer un variogramme vertical caractéristique du site. Ensuite, une contrainte géostatistique a été imposée comme outil de régularisation pour résoudre le problème inverse, par l'intermédiaire de la matrice de covariance basée sur le variogramme. Les points majeurs d'une telle régularisation ont d'abord été mis en évidence par plusieurs cas synthétiques. Il en est ressorti principalement que le choix d'un modèle *a priori* homogène semblait judicieux dans ce cas et que l'absence d'information sur le variogramme horizontal est un moindre mal. Les résultats d'inversion ont permis de déterminer l'extension du plume d'eau salée que ce soit latéralement, en profondeur ou en termes de contenu solide dissous (TDS). Ces observations sont en accord avec la situation hydrogéologique. Une comparaison avec les données de forage a montré que les résultats sont beaucoup plus satisfaisants qu'une régularisation traditionnelle par lissage du modèle (smoothness constraint). L'information *a priori* utilisée dans le processus d'inversion a permis d'améliorer la résolution, même si les outils traditionnels d'évaluation de la qualité de l'image ne sont pas capables de quantifier cette contribution.

Mots-clés : intrusion d'eau salée, côte belge, résistivité électrique, méthode électromagnétique, contrainte géostatistique, processus d'inversion, résolution.

Contents

List of Figures

List of Tables

Chapter 1

Introduction

The overall objective of this master thesis is to develop and apply electrical resistivity tomography (noted hereafter ERT) algorithms in the Belgian coastal area to map the relative positions of fresh and sea water in order to obtain a better knowledge of hydrogeological conditions.

The field site is the Westhoek, a natural reserve in Flanders, situated at the French border, where the quaternary geology leads to particular hydrogeological conditions. The coastal area was first invaded by the sea, and aquifers were filled with sea water. Then, the dune belt developed forming a barrier for the sea, and sea water was replaced by fresh water. Part of this fresh water now flows towards the sea. Because of infiltration during high tides, a salt water lens exists under the beach. In 2004, two artificial tidal inlets were made to enhance biodiversity in the area. These inlets permit sea water to enter the dunes in two infiltration ponds. However, the fresh water of the dunes is extracted for consumption. It is thus very important to monitor this infiltration. At present, a monitoring plan has been developed by the Ghent University (Dr. A. Vandenbohede and Pr. L. Lebbe) to follow the evolution of the infiltration plume in the dune area. Twenty boreholes have been drilled and conductivity measurements were monitored with an electromagnetic logging device (EM39 from Geonics©).

ERT images allow to characterize the subsurface with a higher lateral resolution (metric scale) compared to a borehole network. However, ERT rely on the resolution of a regularized inverse problem, where the initial ill-posed problem is constrained by a smoothness operator not always reflecting the heterogeneity of a site. The EM39 borehole measurements contain important information on the vertical heterogeneity of the bulk electrical resistivity distribution.

A first specific objective of this work is to use these measurements to constrain the inversion process. First, we could impose resistivity values at some locations either as a starting model for the inversion or as an additional regularization operator. However, this would only affect the resistivity values at the boreholes. To allow this constraint in the whole image plane, we will use a regularization operator in the form of a covariance matrix, which can be computed in the vertical direction using the EM39 data.

A second objective of this master thesis is to perform new borehole measurements. These results will be used to determine quantitatively the resolution of ERT. This "true" resolution assessment will be compared with image appraisal tools adopted from the linear inverse theory such as the analysis of the sensitivity matrix, the depth of investigation index (DOI) or the resolution matrix.

Finally, the last objective of the master thesis is to verify if the predictions based on the first EM39 monitoring phase and modeling results remain correct.

First, a short review of bibliography will be presented. Salt water intrusion issues will be placed in a general context and the usefulness of geophysical methods will be highlighted in several specific cases. Chapters 2 and 3 give the theoretical tools necessary to understand the geophysical methods used in this study. Chapter 4 sums up the synthetic benchmarking to highlight the characteristics of the regularization process based on the covariance matrix.

In chapter 5, the geology of the Belgian coastal area will be investigated. This work focus on the Quaternary deposits as they represent the deposits of the investigated zone. Then, a presentation of the Westhoek nature reserve is undertaken in chapter 6, with a description of the deposits, the hydrogeological conditions and the evolution of the intrusion before 2010. Chapter 7 explains the methodology followed to carry out this investigation; preliminary modeling and choice of the profiles to investigate are discussed.

The knowledge of chapter 4 is then applied to characterize at best salt water intrusion occurring in the Westhoek nature reserve. Chapter 8 contains new EM39 measurements, ERT inversion results, their interpretation in terms of total dissolved solid (noted hereafter TDS) content and a comparison with modeling results. At the end of chapter 8, a comparison between image appraisal tools and borehole based resolution assessment is presented. Finally, chapter 9 will draw the conclusions and perspectives linked with this master thesis.

1.1 Salt water intrusion issues

Sea water intrusion (noted hereafter SWI) problems concern many countries around the world. Coastal areas provide inhabitants with places very well situated for economical development and life quality. It is estimated that 44% of the world's population (more people than inhabited the entire globe in 1950) live within 150 kilometers of the coast (Columbia University CCSR, 2006), this number is expected to increase in the future and will contribute to further stress groundwater resources in coastal areas.

Generally, equilibrium exists between fresh and salt water in coastal aquifers (Todd & Mays, 2005). However, this equilibrium is easily broken by human activities. Each activity which tends to decrease the fresh water level will have as a consequence to increase salt water intrusion since the salt water situation (seaside) remains unchanged. The two main activities in coastal areas responsible for a decrease in the fresh groundwater level are land drainage and pumping activities (Goldman & Kafri, 2006).

The latter may cause also severe geotechnical damage according to Terzaghi's law (equation 1.1) :

$$\sigma_{tot} = \sigma_{eff} + \sigma_w \tag{1.1}$$

where σ_{tot} is the total stress $[Pa]$, σ_{eff} the effective stress $[Pa]$ and σ_w the water pressure $[Pa]$. Pumping leads to a decrease of the water pressure and, since the total stress remains constant, the effective stress increases which may produce soil subsidence (Todd & Mays, 2005). This problem is well known in a great number of coastal zones where the so called "sinking cities" are found (e.g. Shanghaï and Venice). In addition, this problem can enhance more salt water intrusion issues.

In arid and semi-arid regions, this problem becomes more worrying since there are few precipitations to renew fresh water. In addition, irrigations in arid regions can lead to an increase in salinity of the groundwater resources (Replogle *et al.*, 1996).

Sea water intrusions can also be generated on purpose to increase the salinity of specific environments. This is the case in the study site, at the Belgian coastline, where two artificial sea inlets were built in the coastal dune belt near De Panne to enhance biodiversity. The consequence is an infiltration of salt water within a fresh water aquifer. It is important to control the extent of this artificial salt water intrusion, because water pumping activities take place in the dune area (Vandenbohede *et al*, 2008a).

1.2 The role of geophysical methods

To control and manage SWI, hydrogeological information is needed. In many cases, borehole and drilling data provide too sparse coverage. Geophysical techniques (gravimetry, magnetism, seismic, electric or electromagnetic methods) are available to complement borehole information to investigate the Earth's subsurface with a higher lateral resolution.

In SWI, electric (DC) and electromagnetic methods are the most commonly used due to their high sensitivity to water salinity. Time domain electromagnetic methods (TDEM) provide typically 1D information at the scale of a few 100's meters whereas DC resistivity measurements are often used to gather a 2D or 3D model of the subsurface or to monitor area down to $\sim$80 meters. They are also more robust in terms of urban environments and practical set-up.

Geophysical exploration may have several objectives. A first and fundamental one is to determine geometrical features such as the depth of unconsolidated sediments or the limit between fresh and salt water. Site specific petrophysical relationships may allow to retrieve properties such as the porosity of sediments or the salt content of water. However, it is much more difficult to obtain successful quantitative results due to the non-uniqueness of bulk electrical resistivity-water salinity law. The clay content, for example, will change the relationship between resistivity and porosity or salinity (Goldman & Kafri, 2006).

1.3 Geophysical studies in cases of salt water intrusion

In the last years, several studies were conducted in the context of salt water intrusions. We will attempt to review them briefly hereafter in order to provide the reader with a state-of-the-art overview with an emphasis on how borehole information is being currently used together with geophysical inversion. De Franco *et al.* (2009) monitored a salt water intrusion by electrical resistivity tomography in the Venice lagoon in Italy where the geological sequence is constituted of sandy and silty layers dating from the late Pleistocene and the Holocene. In this region, several phenomena are acting together: land subsidence, flooding during storms and sea water intrusions. Since the process in this zone is dynamic, due to river interactions, they used time-lapse tomographies (using Wenner arrays) to obtain a better understanding of the evolution of the intrusion over a period of 9 months in 2005. Borehole observations were used to constrain interpretation after standard inversion and a seasonal fluctuation of the salt-water intrusion was observed with the monitoring system, which is one of the first long term time-lapse system.

Carter *et al.* (2008) studied the variation in salinity in a tidal salt marsh basin in South Carolina, USA. Salt marshes are an interface between terrestrial and marine environments. In such environments, groundwater flow plays a great role in several processes such as geochemical exchanges and ecology. This marsh was influenced by tidal and seasonal fluctuations and storm events. A dipole-dipole array was used monthly to investigate the upper 3 m. Salinity measurements in boreholes were used to test the sensitivity of the resistivity models obtained by inversion. Geophysical data allowed to confirm previous data collected in piezometers with much more details.

Martínez *et al.* (2009) studied sea water intrusion in the coastal aquifer of the river Vélez delta in Spain. In this case, the seawater intrusion is enhanced by human fresh water consumption and irrigation. In this study, a Wenner-Schlumberger array was used with a depth of investigation about 90 to 100m. However, during the inversion, RMS error remained quite high (8 to 54% according to different profiles) and no data error analysis was presented. Qualitative comparison was made between ERT results and boreholes. It confirms that ERT was able to detect the depth of the water level. Changes in resistivity were also well correlated with lithological and salinity variations observed in boreholes.

Unlike the cases above, fresh water lenses may be found where salt water is expected. Manheim *et al.* (2004) tried to find fresh water lenses in the Delmarva coastal bays using electrical resistivity streamers and laboratory (water and bulk resistivity measurements made on borehole samples) derived petrophysics. The aim was to show the importance of fresh water discharge in coastal environments. From a geophysical point of view, fresh lenses are more difficult targets since current lines tend to focus in low resistivity areas, yielding less coverage of the anomaly.

This brief overview of the literature shows that electrical resistivity measurements are able to detect fresh-salt water transitions in different types of coastal areas. Nevertheless, a slightly different distribution is expected in the study area, as transition fresh-salt-fresh water will be observed. This case is not so far from the study presented by De Franco *et al.* (2009). Thus, it seems that this method is adequate to investigate salt water infiltration in the Belgian dune area. However, in most cases, ERT data is only used in a qualitative way. We will review below a few papers where geophysical results are used in a quantitative way.

Nguyen *et al.* (2009) proposed a methodology to analyze ERT images in order to select areas where resolution is sufficient to be used for hydrogeological model calibration. The authors used numerical simulations to define zones where a cumulative sensitivity index was indicative of a high correlation between targeted and imaged property value (salt concentration). They applied it to real data sets where boreholes were available and showed that the methodology was successful but also that the representativeness of the petrophysics could be a major difficulty to overcome. They also pointed out the possibility to use ground-truth data when it is available to define the index threshold.

Amidu & Dunbar (2008) tried to evaluate the potential of electrical-resistivity inversion methods for water-reservoir salinity studies at greater depths. They used a calibrated model to evaluate the optimum inversion parameters (mainly the damping factor), and then they used them to invert the real data sets. The study site was the Lake Whitney in Texas, with high salinity values for a fresh water environment (salinity about 3‰). The data was taken with a dipole-dipole electrode array by mobile electrodes on a streamer moved by a boat. In addition, they used water conductivity measurements to constrain the resistivity of the water column during the inversion (by applying measured values on corresponding cells) and to interpret the inversion results (relation between resistivity and salinity). A temperature correction was also used. Constrained inversion led to better results. The advantage in this water reservoir study was that resistivity only depended on salinity and temperature, not on the type of rock or sediment.

Goldman & Kafri (2006) described a methodology to calculate porosity from TDEM and electrical measurements, based on Archie's law (1942) (see chapter 2). They applied this method to different coastal aquifers in Israël.

Electrical resistivity tomography is not the only method used to detect sea water intrusion. For example, Nielsen *et al.* (2007) used transient electromagnetic soundings in the Keta Barrier in Ghana. The transmitter loop was $40m$ by $40m$ with the receiver coil in the center. This method enabled them to map the depth of the low resistivity sediments, certainly filled with salt water. They assumed a depth of investigation of about $50m$ (depending on the depth of the low-conductivity salt-water filled sediments).

For more information on geophysical studies[1] related to sea water intrusion, the readers may

---

[1] Differences in resistivity between salt and fresh water can also be used to calibrate hydrogeological parameters (transport velocity, porosity, dispersivity, preferential flow paths, etc.) of groundwater reservoirs by carrying out tracer experiments. For example, Kemna *et al.* (2002) implemented a salt tracer experiment in heterogeneous sand and gravel aquifer and used a convection-dispersion model to represent the aquifer. Cassiani *et al.* (2006a) studied the possible connection between two aquifers with this method. A big advantage is that the plume of salt water can be followed without a lot of boreholes, even if it remains necessary to take water samples. Belligoi *et*

found detailed information and references in Nguyen *et al.* (2009), Goldman & Kafri (2006) or Cheng & Ouazar (2004).

The different studies reviewed above indicated that, salt water intrusions occur in a lot of contexts and that electrical resistivity methods are able to detect limits between salt and fresh water. Most common arrays (dipole-dipole, Wenner and Wenner-Schlumberger) have been used for these different targets, but a justification is rarely given. So, as for many geophysical studies, it is important to choose the best array for a particular site. In this master thesis, modeling was done, based on EM39 measurements, to estimate the best electrode configuration. The results are developed in chapter 7.

We can also highlight the fact that borehole data is often necessary to interpret inversion results more accurately or to convert resistivity into salinity. However, in most cases, borehole information is only used in this aim; few studies go further in the use of borehole data. In this master thesis, boreholes are widely available to help in the interpretation, but also to assess the quality of the inversion process (chapter 8, section 8.5), like in Nguyen *et al.* (2009) and to constrain it (chapter 8) (example of inversion constraint is explained in Amidu & Dunbar (2008)). In addition, we will develop a method to incorporate such *a priori* information in the inversion procedure and attempt to demonstrate it using synthetic and field cases (chapter 2 for the theory, chapters 4 and 8 for the applications). This procedure is based on the covariance matrix and has already been successfully applied in gravity inversion problems (Chasseriau & Chouteau, 2003). Incorporating geostatistical constraints in non-linear inversion problems is not a new idea, but few studies have explored it (Johnson *et al.*, 2007), especially in electrical resistivity tomography.

---

al. (2008) used a NaCl solution to detect preferential flow paths in a fractured limestone aquifer, using time-lapse electrical resistivity tomography.

Chapter 2

Theory : Electrical methods

2.1 Generalities

Electrical methods in geophysics aim at determining the bulk electrical resistivity (or conductivity) of the subsurface. This is done by measuring electrical potentials (order of mV) on the surface or in boreholes using electrodes resulting from the injection of a controlled electrical current (order of mA). These measurements are then interpreted in terms of bulk electrical resistivity ($Ohm.m$) geometrical distribution and subsequently in terms of lithology and/or fluid chemistry (e.g. salinity). As it will be presented later on, the conductivity of rocks depends on several parameters such as fluid and mineral content, porosity and saturation.

The fundamental physical law governing current flows in the ground is one of Maxwell equations, the Ampère-Maxwell equation (2.1) (Telford *et al.*, 1990)

$$\nabla \times \vec{H} = \vec{J} + \frac{\partial D}{\partial t} + \vec{J_s} \tag{2.1}$$

where $\vec{H}$ is the magnetic field intensity $[A/m]$, $\vec{J}$ is the current density $[A/m^2]$, $\vec{D}$ is the electric displacement $[C/m^2]$ and $\vec{J_s}$ is the current density due to a source $[A/m^2]$.

When equation 2.1 is coupled with the constitutive equation of Ohm's law (2.2)

$$\vec{J} = \sigma \vec{E} \tag{2.2}$$

where $\vec{E}$ is the electric field intensity $[V/m]$ and σ is the conductivity of the medium $[S/m]$, i.e. the inverse of the resistivity $\rho = \frac{1}{\sigma}$ $[Ohm.m]$, it yields the well-known Poisson equation for quasi-static fields (equation 2.4), knowing that the electric field is linked with the electrical potential ϕ $[V]$ (equation 2.3)

$$\vec{E} = -\nabla \phi \tag{2.3}$$

and that current displacements may be neglected under the quasi-static assumption.

$$\nabla \cdot \vec{J_s} = -\nabla \cdot (\sigma \nabla \phi) \tag{2.4}$$

In a homogenous half-space, the electrical Poisson equation (2.4) can be solved analytically to find the distribution of the potential due to one current source (injected current I $[A]$) at the distance r $[m]$ from the source (Telford *et al.*, 1990)

$$\phi = \frac{\rho I}{2\pi r} \tag{2.5}$$

In the more common case of a general survey, 4 electrodes are used for one measurement. The potential difference between two points caused by current I injected by two current electrodes

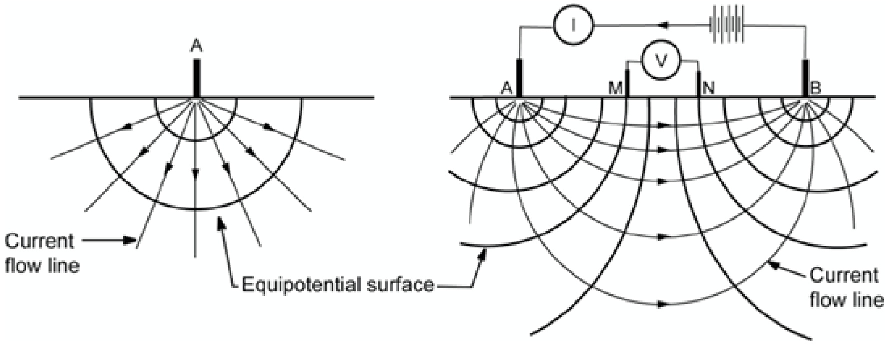

Figure 2.1: Current flow lines and equipotential surfaces for a single current source (left) and a set of current electrode (right) (Møller *et al.*, 2006).

(a positive current source and a negative one) is measured. Using the principle of superposition, the potential difference is then given by

$$\Delta\phi = \frac{\rho I}{2\pi}\left(\frac{1}{|r_A - r_M|} - \frac{1}{|r_A - r_N|} - \frac{1}{|r_B - r_M|} + \frac{1}{|r_B - r_N|}\right) \tag{2.6}$$

where r_X is the position of electrode X. Figure 2.1 shows the current flow lines and the equipotential surfaces for a single source and a four electrode configuration.

In the general case, the medium does not display a homogeneous resistivity. In this case, this is not the true resistivity which is measured, but an apparent resistivity $[Ohm.m]$

$$\rho_a = \frac{K\Delta\phi}{I} \tag{2.7}$$

where K is the so-called geometrical factor $[m]$, equal to

$$K = \frac{2\pi}{\frac{1}{|r_A - r_M|} - \frac{1}{|r_A - r_N|} - \frac{1}{|r_B - r_M|} + \frac{1}{|r_B - r_N|}} \tag{2.8}$$

However, a measuring instrument normally deduces the resistance R $[Ohm]$ from the injected current I and the potential difference $\Delta\phi$

$$R = \frac{\Delta\phi}{I} = \frac{\rho_a}{K} \tag{2.9}$$

For real heterogeneous media, equation 2.4 does not have an analytical solution, but a numerical solution can be routinely obtained by finite difference or finite element methods (Sasaki, 1994).

One important consequence of the hypothesis used in the derivation of the Poisson equation, is that if the medium is assumed to be linear, with respect to Ohm's law

$$\frac{\Delta\phi_{MN}}{I_{AB}} = \frac{\Delta\phi_{AB}}{I_{MN}} \tag{2.10}$$

The medium is linear if the conductivity distribution σ is independent of ϕ, then we fulfill the reciprocity theorem (equation 2.10; Parasnis, 1988).

This theorem signifies that the resistance has to be the same for normal and reciprocal measurements. The latter is practically achieved by swapping current and potential electrodes and is used as an estimation of the error level of a measured data set.

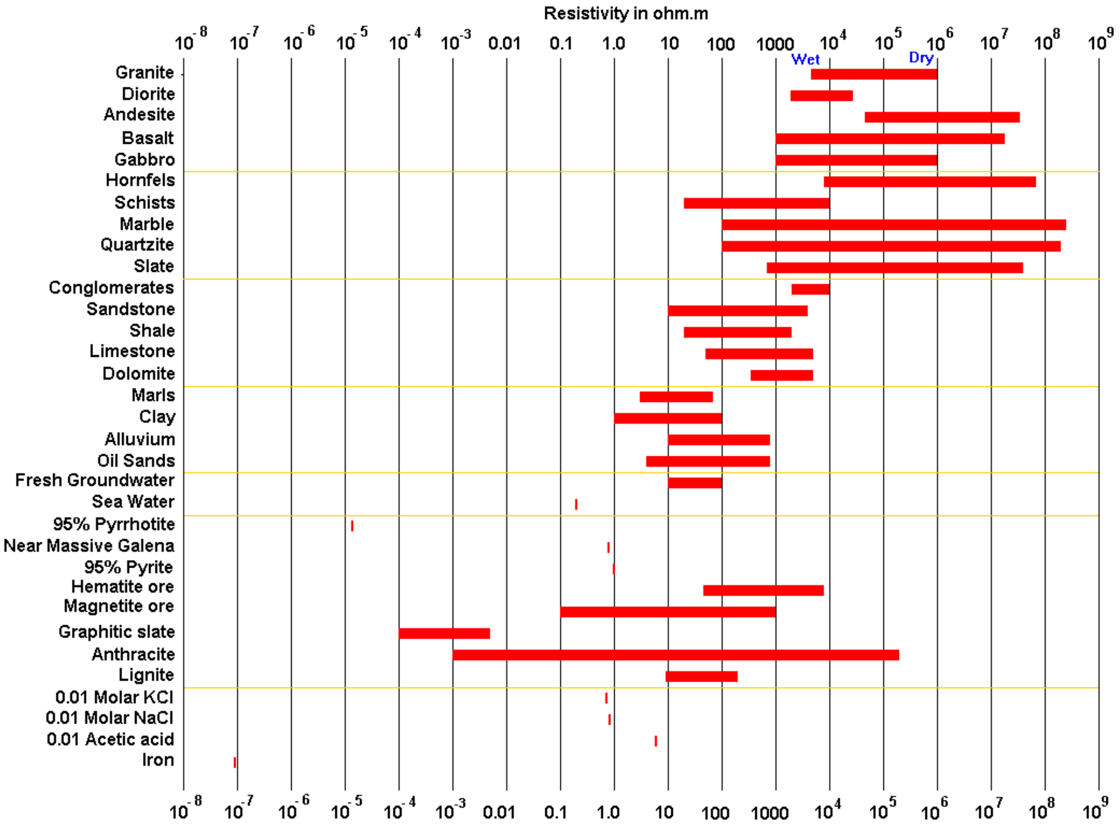

Figure 2.2: Resistivity range for different types of rocks and water (Loke, 2004).

2.2 Electrical properties of rocks

The electrical current can flow in the soil/rock in three ways. The first one is electronic conduction but occurs rarely in usual subsurface materials. This phenomenon occurs in metals or minerals such as sulfides where the current is composed of free electrons. The second one and most important one is the electrolytic conduction where the movement of ions induces the current flow. The third current is related to surface conductivity and occurs at the interface between grains and the interstitial fluid. It is mainly present where clays occur (Telford et al., 1990).

Figure 2.2 gives the (wide) range of resistivity generally encountered for typical rock types. As can be easily viewed, unconsolidated sediments and sedimentary rocks have much lower resistivity values than igneous and metamorphic rocks, mainly because of the difference of porosity.

We see that the interval value covers several orders of magnitude. In addition, a same value of resistivity can be shared by different kinds of rocks, according to the porosity, the fracturation, the salt content of the pore water, etc. It is thus very difficult to describe a resistivity section without other geological information, such as borehole data, geological map or a lithological description.

2.3 Petrophysical law

In porous rocks or sediments, the bulk electrical resistivity varies mainly with the resistivity of the fluid contained in the pores. Obviously, the resistivity depends on the nature of the fluid and the degree of saturation. Historically, the relation between rock and fluid resistivity was discovered by Archie (1942) within the context of log interpretation in petroleum exploration (Cassiani *et al.*, 2006b). The expression is

$$\sigma_b = \frac{\sigma_f}{F} \tag{2.11}$$

where σ_b is the bulk conductivity of the rock $[S/m]$, σ_f is the conductivity of the fluid $[S/m]$ and F is the formation factor.

In the general case of an unsaturated rock, equation 2.11 becomes

$$\sigma_b = \frac{\sigma_f}{F} S_f^n \tag{2.12}$$

where S_f is the fluid saturation and n an empirical exponent, with a value close to 2. This equation only takes into account the conductivity of the rock due to the fluid content. In some cases, the matrix conductivity is non-negligible. Clay, oxide and electrical double layer in contact with the fluid are responsible for a surface conductivity of grain coating. An additional term is needed in Archie's law to describe this effect (Waxman & Smits, 1968)

$$\sigma_b = \frac{\sigma_f}{F} S_f^n + \sigma_s \tag{2.13}$$

where σ_s is the surface conductivity $[S/m]$. Note that this assumes that fluid and solid act as conductors in parallel, which is not always the case (Cassiani *et al.*, 2006b).

The formation factor F is an empirical parameter defined by equation 2.14 (Cassiani *et al.*, 2006b)

$$F = \frac{a}{\phi^m} \tag{2.14}$$

where a is an empirical constant, theoretically equal to 1; m is an empirical exponent depending on the pore structure and cementation (tortuosity), it ranges from 1 to 2.5 in most cases and ϕ is the porosity of the rock.

In a lot of cases, equation 2.12 is used to describe the relation between fluid and rock conductivity. This assumption is acceptable if the clay and oxide contents are low enough. Just by analyzing the terms of Archie's law, we can determine several processes likely to change the conductivity of the subsurface.

In the case of unsaturated zones, a change of saturation in equation 2.12 will change the conductivity of rocks between t_1 and t_2, two measurement instants. We can write (Cassiani *et al.*, 2006b)

$$\frac{\sigma_{b,t1}}{\sigma_{b,t2}} = \frac{S_f^n(t_1)}{S_f^n(t_2)} \tag{2.15}$$

In the particular case of saturated zone, other phenomena can explain a conductivity variation. According to equation 2.13, an increase in clay content will also increase the conductivity of the rock.

A change in porosity, i.e. a variation of the formation factor, can also explain a variation of conductivity (Goldman & Kafri, 2006).

Another possibility is a variation in the fluid conductivity σ_f. Such a variation can be caused by a temperature variation or a difference in salinity. Two different models are generally used to explain the variation in water conductivity with water, an exponential one (equation 2.16) and a linear one (equation 2.17) (Hayley *et al.*, 2007)

$$\frac{\sigma_T}{\sigma_{25}} = e^{-\frac{A}{R}\left(\frac{1}{T}-\frac{1}{298}\right)} \tag{2.16}$$

$$\frac{\sigma_T}{\sigma_{25}} = m(T-25)+1 \tag{2.17}$$

where σ_T is the conductivity at temperature T $[S/m]$, σ_{25} is the conductivity at $25°C$ $[S/m]$, R is the universal gas constant $[J.mol^{-1}.K^{-1}]$, A is the activation energy of conduction $[J.mol^{-1}]$, T is the temperature expressed in degrees Kelvin in the exponential model and in degrees Celsius in the linear model, m is the fractional change in conductivity by degree Celcius, its value is around 0.02.

The surface conductivity of the rock also varies with temperature (Hayley *et al.*, 2007) and salinity.

The fact that water conductivity changes with the salt content is well known since pure water is a poor current conductor. Several relations have been described to link salinity and conductivity of salt water. The practical salinity scale (Perkin & Lewis, 1980) describes empirical equations defined to fit a lot of data collected and analyzed in several laboratories. These relations are quite complex and necessary to obtain a good precision. However, simplifications exist. The following relation between salinity and resistivity of water is often taken (Manheim *et al.*, 2004)

$$S = 7.042 \times \sigma_w^{1.0233} \tag{2.18}$$

where S is the salinity in ‰ and σ_w the conductivity of water in $[S/m]$.

However, in this master thesis, it was decided to use a relation between the conductivity and the total dissolved solid (TDS in mg/l) content(Van Meir & Lebbe, 2003), which is commonly used by Ghent University in salt water intrusion issues

$$TDS = 10F\sigma_b \tag{2.19}$$

where TDS is the total dissolved solid content $[mg/l]$, F is the formation factor and σ_b is the bulk conductivity of the soil $[mS/m]$. This relation is defined at $10°C$.

However, it is always better, when possible, to calibrate directly any relation on bulk resistivity (or conductivity). Figure 2.3 illustrates the calibration given by Goldman & Kafri (2006) for time domain electromagnetic method compared with salinity of groundwater samples. The measurements correspond to the Mediterranean Sea, Dead Sea and Read Sea coastal aquifers. We see that variations are bigger for fresh water. An on-site calibration is thus always preferable.

2.4 ERT measurements and electrode arrays

The choice of configuration used for a field campaign is very important as the different configurations also display different sensitivity profiles and signal to noise ratio (Loke, 2004 ; Dahlin & Zhou, 2004). Figure 2.4 shows the more common configurations used.

The signal to noise ratio can be linked with the geometric factor. Using the position of the current and potential electrodes, we can calculate the geometric factor corresponding to a homogeneous half-space for each configuration (equation 2.8). The results are summarized in table 2.1. A comparison of geometric factors is also given for an equal total length ($90m$).

It appears that the geometric factor changes over several orders of magnitude according to the array that is used. The effect of a high geometric factor can be explained by analyzing the effect of a small perturbation $d\phi$ on equation 2.7. This perturbation is measured simultaneously with the true potential difference $\Delta\phi$. If the factor geometric is high, it signifies that the value of $\Delta\phi$ is quite low for a same current injected and a same apparent resistivity. Thus, the small perturbation can represent a big part of the total signal measured $\Delta\phi + d\phi$ leading to a low

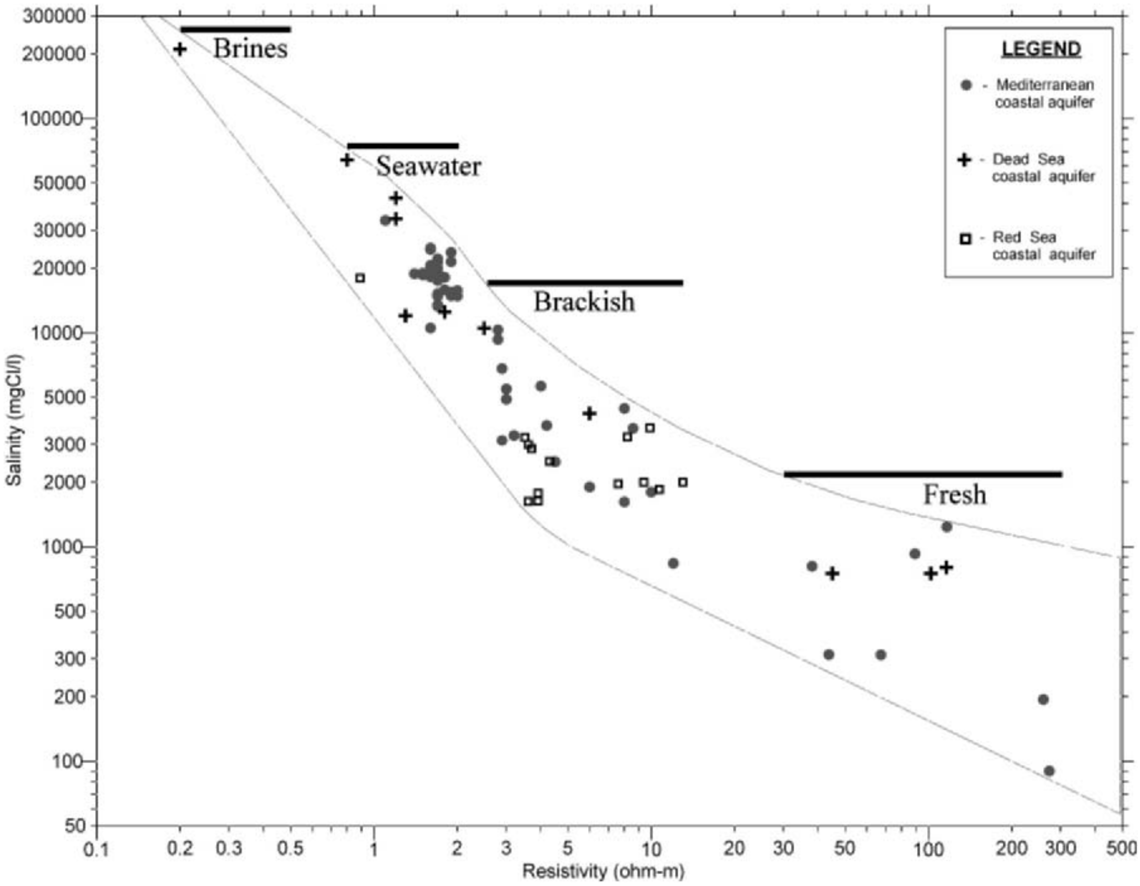

Figure 2.3: Relation between resistivity and salinity for TDEM measurements (Goldman & Kafri, 2006).

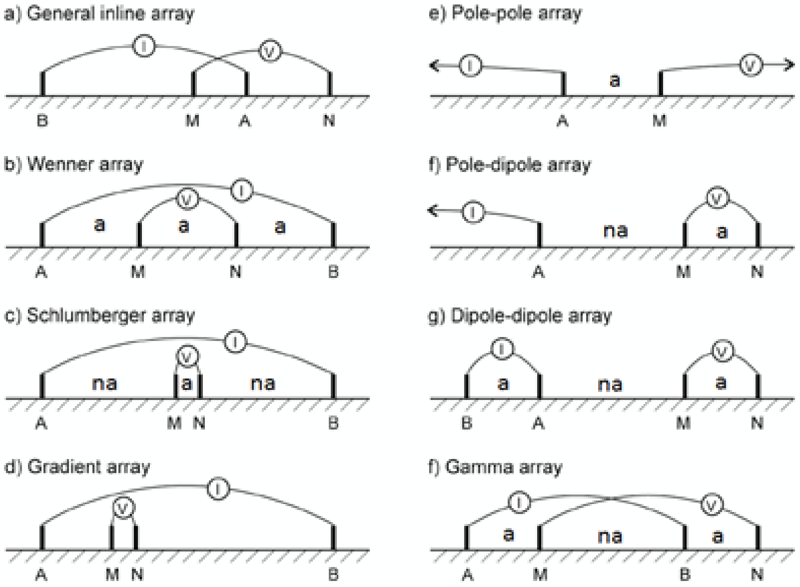

Figure 2.4: Electrode configurations (modified after Møller *et al.*, 2006).

Array	Geometric factor	a (m)	n	K (m)
Wenner-alpha	$K = 2\pi a$	30		188.5
Wenner-Schlumberger	$K = \pi n(n+1)a$	10	4	628.3
Dipole-dipole	$K = \pi n(n+1)(n+2)a$	11.25	6	11875.2
Pole-pole	$K = 2\pi a$	90		565.5
Pole-dipole	$K = 2\pi n(n+1)a$	10	8	4523.9
Gamma	$K = \frac{\pi an(n+2)}{n^2+n+1}$	11.25	6	41.4

Table 2.1: Electrode arrays and geometric factors.

signal to noise ratio. During the inverse problem, the noise can then produce artifacts in the resistivity distribution.

The dipole-dipole and pole-dipole arrays display a high geometric factor while the Wenner array leads to very low geometric factors. The Wenner-Schlumberger and the pole-pole arrays are intermediate. It signifies that the signal strength is smaller for the dipole-dipole and the pole-dipole arrays. The other ones are quite robust (Loke, 2004).

Dahlin & Zhou (2004) compared ten electrode arrays by numerical modeling to examine the surveying efficiency and the imaging capacities of each array. Their results allow them to highlight the main advantages and drawbacks of each array type. The three most used arrays are the Wenner, the dipole-dipole and the Wenner-Schlumberger.

The Wenner has generally less noise contamination but it has a poor spatial resolution compared with other arrays. In addition, its reciprocal array (switching current and potential electrodes) is more prone to pick up noise, which can cause some problems when analyzing the noise level on the field. Its main strength is the depth determination.

The dipole-dipole array has a better spatial resolution than other arrays, but is more sensitive to noise. It is well designed to find vertical and dipping structure compared to other ones. It is not advisable to use a n factor greater than 6 for this array.

The Wenner-Schlumberger array is quite similar to the Wenner array. However, it has a less good signal to noise ratio, but has the advantage of a higher spatial resolution that remains inferior to the one of the dipole-dipole.

It is why they recommend firstly the dipole-dipole array or the Wenner-Schlumberger array. Even if the Wenner array has the smallest noise contamination, it does not produce a good resolution image. Note that other arrays can also lead to good results such as the gradient or pole-dipole arrays.

The difference between the arrays can be explained by the difference in sensitivity between them. The sensitivity function shows how a change in resistivity in the section will influence the potential measurement. For example, equation 2.20 gives the 3D sensitivity function for a pole-pole array (a is the distance between potential and current electrodes). To obtain it for 4 electrodes array, we had to add the contribution of the other electrodes. For a 2D section, the sensitivity is obtained by integrating equation 2.20 along the direction y perpendicular to the section. This assumes, just as for the inversion process, that the subsurface is homogeneous in this direction, which means no 3D effect (Loke, 2004).

$$F_{3D}(x,y,z) = \frac{1}{4\pi^2}\frac{x(x-a)+y^2+z^2}{[x^2+y^2+z^2]^{1.5}[(x-a)^2+y^2+z^2]^{1.5}} \tag{2.20}$$

Negative values of sensitivity signify that a higher resistivity zone, compared to the rest of the section, located in the area of negative sensitivity, will induce a smaller apparent resistivity

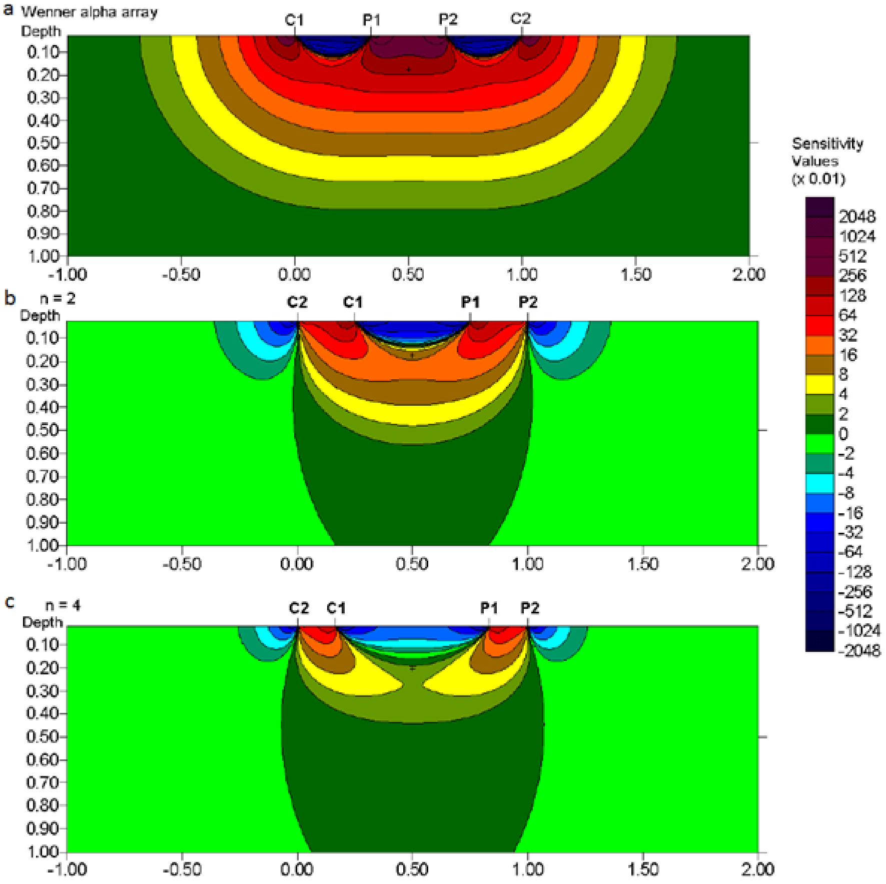

Figure 2.5: Sensitivity values for (a) the Wenner array (b) the dipole-dipole array (n=2) and (c) the dipole-dipole array (n=4) (modified after Loke, 2004).

(or resistance) value (Loke, 2004). It is why it is impossible to interpret electrical resistivity time-lapse data directly in terms of increase or decrease in resistivity.

Figure 2.5 shows the sensitivity distribution for the Wenner and the dipole-dipole arrays. The sensitivity distribution for the Wenner configuration has almost horizontal contours with sensitivity decreasing in depth. It is why this array is more sensitive to vertical changes in resistivity (horizontal structures) than to horizontal changes (Loke, 2004).

The dipole-dipole array has different sensitivity values according to n. We see that this array is very sensitive to changes below both electrode pairs. This effect increases with n. The dipole-dipole array is thus much more able to detect vertical structures than the Wenner configuration. In addition, it has better horizontal data coverage (Loke, 2004).

The Wenner-Schlumberger array displays intermediate sensitivities distribution between Wenner and dipole-dipole arrays (Loke, 2004).

2.5 Inversion

2.5.1 Introduction

In the case of ERT, the inverse problem consists in determining the conductivity (or resistivity) distribution of the soil from the resistance data collected. The forward problem does the contrary; it calculates the voltages from a conductivity distribution.

In a geophysical problem, it is not sufficient to find a mathematical solution to the problem; the solution has to be physically plausible. Inverse problems are often said to be ill-posed due to one of the following reasons: existence, non-uniqueness or instability (Aster *et al.*, 2005; Nguyen, 2009).

The solution **existence** is usually verified, but the data happens to contain too much noise or the mathematical model to be too approximate to find a model explaining the data. If a solution does exist, it may not be **unique**. It is often the case in potential field problems. For example, if a model different from zero is such that the data is equal to zero, this solution can be added to a solution of the true problem without possible discrimination. The solution may be **instable** when a small change in the data (for example due to the noise) can lead to big differences in the calculated model (Aster et al, 2005).

A common way to solve ill-posed problems is to regularize them by additional constraints on the possible solution. It leads to conditionally well-posed problems and the solution is unique in the sense of the regularized problem (Aster et al, 2005).

2.5.2 Forward problem

The forward problem is expressed by the Poisson equation (2.4). We can also express it on a general form

$$\mathbf{G}(\mathbf{m}) = \mathbf{d} \tag{2.21}$$

where **G** is the non-linear operator mapping the conductivities of the model **m** to the data set **d**. To solve the forward problem for a 2D-tomography with finite-element or finite difference, we have to consider boundary conditions

$$\begin{cases} \sigma\partial_n\phi + \beta\phi = 0 \; for\ the\ mixed\ BC \\ \partial_n\phi = 0 \; at\ the\ interface\ soil - air \end{cases} \tag{2.22}$$

where β defines the type of boundary condition and ϕ the electrical potential (Kemna, 2000).

We have also to assume that the bulk conductivity distribution is constant in the direction perpendicular to the profile. The general 3D problem becomes a 2.5D problem. A Fourier transform is then applied to the equation (for the variable y corresponding to the perpendicular direction) and the problem is solved in this space and is then transformed back at $y = 0$. The potential distribution is solved for each electrode and the potential at one node can be superposed for the right electrode configuration. It signifies that every time that this assumption is not verified (3D effect), it can lead to a certain degree of misinterpretation (Kemna, 2000).

The forward problem is not only used to carry out modeling, but it is also used during the inverse problem to evaluate the data misfit. Indeed, after each iteration, a forward problem is solved to compare the true data and the data coming from the model.

2.5.3 Inverse problem

During the regularized inverse problem, the aim is to minimize the objective function

$$\psi(\mathbf{m}) = \psi_d(\mathbf{m}) + \lambda\psi_m(\mathbf{m}) \tag{2.23}$$

where λ is the regularization parameter. It quantifies the compromise between the data misfit $\psi_d(\mathbf{m})$ expressed by a norm $\psi_d(\mathbf{m}) = ||\mathbf{G}(\mathbf{m}) - \mathbf{d}||$ and *a priori* model characteristics given by ψ_m (Kemna, 2000). **m** is the model, defined in electrical problem as $m_i = \ln$ or $\log\sigma_i$. Generally, two types of norms are used. The norm L_2 (equation 2.24) corresponds to a least-square solution and assumes a Gaussian distribution of the errors (the norm is the mean of the distribution).

The norm L_1 (equation 2.25) assumes a Laplace distribution of the errors and corresponds to the median of the distribution. It works better with outliers (Aster *et al.*, 2005).

$$||\mathbf{G}(\mathbf{m}) - \mathbf{d}||_2 = \sqrt{\sum_{i=1}^{n} (G_i(\mathbf{m}) - d_i)^2} \tag{2.24}$$

$$||\mathbf{G}(\mathbf{m}) - \mathbf{d}||_1 = \sum_{i=1}^{n} |(G_i(\mathbf{m}) - d_i)| \tag{2.25}$$

A traditional inversion process is the Occam's inversion which uses a smoothness constraint (Aster *et al.*, 2005). The objective function is defined as

$$\psi(\mathbf{m}) = ||\mathbf{W_d}(\mathbf{G}(\mathbf{m}) - \mathbf{d})||^2 + \lambda||\mathbf{W_m}\mathbf{m}||^2 \tag{2.26}$$

where $\mathbf{W}_d = diag(\frac{1}{\varepsilon_1}, \frac{1}{\varepsilon_2}, \ldots, \frac{1}{\varepsilon_n})$ gives an estimation of error (or noise) level and $\mathbf{W}_m$ is a matrix describing *a priori* information. Indeed, if we weight each misfit by its expected standard deviation ε such that

$$\psi_d(\mathbf{m}) = \sum_{i=1}^{n} \left(\frac{G_i(\mathbf{m}) - d_i}{\varepsilon_i} \right)^2 \tag{2.27}$$

the set of data is fitted with each term $G_i(\mathbf{m}) - d_i$ fitted to its error level ε_i and the final RMS error, given by

$$\varepsilon^{RMS}(\mathbf{m}) = \sqrt{\frac{\psi_d(\mathbf{m})}{n}} \tag{2.28}$$

where n is the number of parameters, should be equal to 1 (Kemna, 2000).

2.6 Regularization operators

2.6.1 First-order difference matrix

The first-order difference matrix is widely used in electrical inversion as it is the default method used in RES2DINV software (Geotomo software, 2005). It tends to produce smooth variation in resistivity values (Loke, 2004). This operator is defined by

$$\mathbf{L} = \begin{pmatrix} -1 & 1 & 0 & \cdots & 0 \\ 0 & -1 & 1 & \cdots & 0 \\ 0 & 0 & -1 & \cdots & 0 \\ \vdots & \vdots & \vdots & \ddots & \vdots \\ 0 & 0 & 0 & \cdots & 0 \end{pmatrix} \tag{2.29}$$

Anisotropy can be implemented by using different weights in the different directions of space

$$\mathbf{W_m} = \alpha_x \mathbf{L_x^T L_x} + \alpha_z \mathbf{L_z^T L_z} \tag{2.30}$$

In a lot of cases, assuming that there is some continuity in the subsoil and that the gradients are not too important is satisfactory. In other cases, sharp boundaries are expected and a smoothness constraint is not the best option. Robust or blocky model constraint has been developed. However, a drawback of these methods is that such an assumption is not always based on reliable data (hard data).

2.6.2 Geostatistical operators

Another way to include prior information on the model in the inverse problem is to use parameter covariance. Chasseriau & Chouteau (2003) give several ways to find parameter covariance such as experimental measurements of the properties of rocks, results from a previous inverse process, estimation by the data covariance, etc.

The method that will be used in this master thesis is based on a model of covariance parameters derived from a variogram model. The variogram model will be based on experimental variograms coming from borehole conductivity data. This method was used by Chasseriau & Chouteau (2003) within the context of gravimetric inverse problem. They defined 3D variogram models to find a covariance model and apply this regularization method on both synthetic and field data. It permits them to better retrieve the form of a dipping dyke for example.

Johnson *et al.* (2007) incorporated directly a variogram operator into the inversion process. In this way, they wanted to find a model matching both the data and the statistical parameters. They applied their method to radar velocity tomography data. The model does not directly appear in their objective function, but it is used to calculate the variogram which is compared to an *a priori* one.

This type of regularization was not used in this master thesis. However, the approach is very similar since we impose a geostatistical constraint on the model. The advantage of the method presented by Johnson *et al.* (2007) is that it enables to fit exactly the statistics at the end of the inversion (up to a level depending on the uncertainty). This approach can be extremely successful when there is a lot of information to estimate the variograms. However, as we will see in chapter 4 and 8, it can be very difficult to estimate the horizontal range of the variogram with only few boreholes. In such a case, it could be misleading to use an algorithm which imposes statistics. It is safer to have an algorithm which tries to fit the data and that uses a regularization parameter to impose the geostatistical constraints. In this way, at the end of the inversion process, we can have a horizontal range different from the one imposed.

Another difference in the two methods is the role of the prior model (equation 2.35). In the approach of Johnson *et al.* (2007), it does not appear. The role of the starting model is thus more important. At the end of inversion, zones of low sensitivity remain close to this starting model. It is the reason for which they realize a lot of inversions with different starting models. In this way, they obtain a mean value and a variance for each cell, but it costs a lot of computation time, in particular for 3D problems. In the method of Chasseriau & Chouteau (2003), similar to the algorithm developed in this master thesis, we use the prior model to give prior information which contributes to improve the solution in low sensitivity zones and to obtain reliable solution with one inversion only (see chapter 4 and 8).

The idea behind the variogram is that two observations located close to each other should look more alike than observations far away from each other. It signifies that the information about a parameter at a point X_1 could be used to have a better estimation of the value of this parameter at another point X_2 (Marcotte, 2009).

In a geostatistical approach, spatial parameters are considered as a realization of a random function Z. If we want to analyze this random function, it is needed to make the assumption of stationarity to simplify the process (Gneiting *et al.*, 2000).

The process Z is said to be second-order stationary if second moments exist and the expectation $E\left(Z(x)\right)$ and the covariance $Cov\left(Z(x), Z(x+h)\right)$ do not depend on $x \in R^d$ (Gneiting *et al.*, 2000). The covariance function is then defined as

$$C(h) = Cov\left(Z(x),\, Z(x+h)\right),\ h\ \in\ R^d \tag{2.31}$$

In some applications, a weaker assumption is sufficient, the intrinsic hypothesis. Each stationary process is also intrinsically stationary, but the converse is not true. The random function Z is intrinsically stationary if the increment process $I_h = \left\{Z(x) - Z(x+h) : x \in R^d\right\}$ is stationary for all lag vectors $h \in R^d$. Then, $E\left(Z(x) - Z(x+h)\right)$ and $E\left(Z(x) - Z(x+h)\right)^2$ do not depend on x (Gneiting *et al.*, 2000). The semi-variogram (or variogram as it will be said in the next sections) is then defined as

$$\gamma(h) = \frac{1}{2}E\left(Z(x) - Z(x+h)\right)^2,\ h\ \in\ R^d \tag{2.32}$$

If the variogram $\gamma(h)$ of an intrinsically stationary process is bounded, we can link the variogram and the covariance function $C(h)$ by the relation 2.33, where σ^2 is the variance of the process Z (Marcotte, 2009 ; Gneitling *et al.*, 2000)

$$\gamma(h) = \sigma^2 - C(h) \tag{2.33}$$

Unfortunately, it is impossible to demonstrate the stationarity of a process (Marcotte, 2009). Indeed, we have only access to one realization of the random function; we do not have access to the expectation value. It is the responsibility of the operator to decide if this assumption is acceptable or not.

An estimation of the variogram (the experimental variogram) for the variable Z is given by

$$\gamma(h) = \frac{1}{2N(h)}\sum_{i=1}^{N(h)}[Z(x_i) - Z(x_i + h)]^2 \tag{2.34}$$

where $N(h)$ is the number of the pairs of observation separated by a distance h. Several models are used to describe the experimental variogram. All of them are based on three different parameters (Chasseriau & Chouteau, 2003):

- the range a is the distance after which there is no more correlation;
- the sill C is the value of the variogram at a distance equal to the range, normally equal to the variance;
- the nugget effect C_0 is used to represent the small-scale variation and is generally combined with other models of variogram.

Marcotte (2009) gives five variogram models commonly used in geology. The corresponding expressions are presented in table 2.2. The power model is not bounded; it will thus not be used to determine the covariance matrix.

For a model with n parameters, the covariance matrix can be built by the relation 2.33. This matrix is a $n \times n$ matrix. The element $C_{(ni,nj)}$ represents the covariance between parameters i and j. The elements of the diagonal are thus equal to the variance of the variable. The value of the covariance then decreases until zero when there is no correlation between parameters anymore.

Once the covariance matrix $\mathbf{C_m}$ is known, it can be used to constrain the inversion to replace the smoothness constraint term. The objective function becomes

$$\begin{aligned}\psi(\mathbf{m}) &= ||\mathbf{W_d}(\mathbf{G}(\mathbf{m}) - \mathbf{d})||^2 + \lambda\mathbf{C_m^{-1}}||\mathbf{m} - \mathbf{m_0}||^2 \\ &= (\mathbf{G}(\mathbf{m}) - \mathbf{d})^T\mathbf{W_d^T}\mathbf{W_d}(\mathbf{G}(\mathbf{m}) - \mathbf{d}) + \lambda(\mathbf{m} - \mathbf{m_0})^T\mathbf{C_m^{-1}}(\mathbf{m} - \mathbf{m_0})\end{aligned} \tag{2.35}$$

where $\mathbf{m_0}$ is a prior model. In this way, the constraint on the model is to force it to verify the statistics that are expected. The bigger is the regularization parameter, the more the statistical

Model	Equation
Nugget Effect	$\gamma(h) = \begin{cases} 0 \; if \; h = 0 \\ C_0 \; if \; h > 0 \end{cases}$
Spherical	$\gamma(h) = \begin{cases} C\left[1.5\frac{h}{a} - 0.5\left(\frac{h}{a}\right)^3\right] \; if \; h < a \\ C \; if \; h \geq a \end{cases}$
Gaussian	$\gamma(h) = C\left[1 - e^{-3\left(\frac{h}{a}\right)^2}\right]$
Exponential	$\gamma(h) = C\left[1 - e^{-3\left(\frac{h}{a}\right)}\right]$
Power	$\gamma(h) = Ch^b \; (0 < b < 2)$

Table 2.2: Variogram models.

parameters are respected. Tarantola (2005) uses this expression, but gives the same weight to the data and the model misfit ($\lambda = 1$).

We adapted the calculation of the covariance matrix in the CRTOMO code (Kemna, 2000) to account for variogram parameters. This code permits to solve resistivity problem and is written in FORTRAN 90. The code developed permits to use Gaussian, exponential and spherical model for the variogram model. In addition the nugget effect can be directly taken into account in the expression of the model. The other parameters to enter are the sill value as well as the vertical a_z and horizontal a_x ranges.

Knowing the position of the center of the cell corresponding to a parameter, the algorithm calculates the distance h and the angle α (angle with the horizontal line). According to this angle, a "true" range is calculated by the same way than Chasseriau & Chouteau (2003). If we assume that the ranges are distributed on an ellipse, we find that the range in direction α, $a(\alpha)$ is equal to

$$a(\alpha) = \frac{a_x a_z}{(a_x^2 \sin^2 \alpha + a_z^2 \cos^2 \alpha)^{\frac{1}{2}}} \tag{2.36}$$

2.7 Inversion algorithm

The resolution of the inverse problem is based on the minimization of the objective function (Kemna, 2000). The problem can be expressed as

$$min(\psi(\mathbf{m})) \tag{2.37}$$

The way used to achieve this is to begin with a model $\mathbf{m}_0$ and to increment it by $\mathbf{\Delta m}$ to converge to the solution $\mathbf{m}$ that fits the equation above. Let us write the Taylor series decomposition of $\psi(\mathbf{m})$

$$\begin{aligned} \psi(\mathbf{m}) &= \psi(\mathbf{m}_0 + \mathbf{\Delta m}) \\ &\approx \psi(\mathbf{m}_0) + \frac{\partial\psi(\mathbf{m}_0)}{\partial\mathbf{m}}\mathbf{\Delta m} + \frac{1}{2}\frac{\partial^2\psi(\mathbf{m}_0)}{\partial\mathbf{m}^2} + \cdots \\ &\approx \psi(\mathbf{m}_0) + \mathbf{J}^T\mathbf{\Delta m} + \frac{1}{2}\mathbf{\Delta m}^T\mathbf{H}\mathbf{\Delta m} + \cdots \end{aligned} \tag{2.38}$$

where

$$\mathbf{J}^T = \begin{pmatrix} \frac{\partial\psi(\mathbf{m}_0)}{\partial m_1} & \cdots & \frac{\partial\psi(\mathbf{m}_0)}{\partial m_n} \end{pmatrix} \tag{2.39}$$

$$\Delta\mathbf{m}^T = \begin{pmatrix} \Delta m_1 & \cdots & \Delta m_n \end{pmatrix} \tag{2.40}$$

$$\mathbf{H} = \begin{pmatrix} \frac{\partial^2\psi(\mathbf{m}_0)}{\partial m_1^2} & \cdots & \frac{\partial^2\psi(\mathbf{m}_0)}{\partial m_1 \partial m_n} \\ \vdots & \ddots & \vdots \\ \frac{\partial^2\psi(\mathbf{m}_0)}{\partial m_n \partial m_1} & \cdots & \frac{\partial^2\psi(\mathbf{m}_0)}{\partial m_n^2} \end{pmatrix} \tag{2.41}$$

To minimize $\psi(\mathbf{m})$, the derivative with respect to $\mathbf{\Delta m}$ has to be equal to zero what leads to

$$\frac{\partial\psi(\mathbf{m}_0 + \mathbf{\Delta m})}{\partial\mathbf{\Delta m}} \approx 0 + \mathbf{J}^T + \mathbf{H\Delta m} \Leftrightarrow \mathbf{H\Delta m} = -\mathbf{J}^T \tag{2.42}$$

The algorithm to calculate this has three steps

1. Solve $\mathbf{H\Delta m} = -\mathbf{J}^T$
2. $\mathbf{m}_{k+1} = \mathbf{m}_k + \mathbf{\Delta m}$
3. $k = k + 1$

If the Gauss-Newton method is used to solve this equation, the expression becomes in the case of the smoothness constraint inversion

$$(\mathbf{J}_k^T \mathbf{W}_\mathbf{d}^T \mathbf{W}_\mathbf{d} \mathbf{J}_k - \lambda \mathbf{W}_\mathbf{m}^T \mathbf{W}_\mathbf{m}) \mathbf{\Delta m}_k = \mathbf{J}_k^T \mathbf{W}_\mathbf{d}^T \mathbf{W}_\mathbf{d} (\mathbf{d} - \mathbf{G}(\mathbf{m}_k)) - \lambda \mathbf{W}_\mathbf{m}^T \mathbf{W}_\mathbf{m} \mathbf{m}_k \tag{2.43}$$

If another regularization tool is used, we just have to replace each appearance of $\mathbf{W}_\mathbf{m}^T \mathbf{W}_\mathbf{m}$ by the new expression of the regularization operator ($\mathbf{C}_\mathbf{m}^{-1}$ for example) and to add the prior model in the expression.

The CRTOMO program (Kemna, 2000) used in this master thesis, tries to find the value of λ, at each iteration, that minimizes the data misfit. In addition, once the iterations find a model whose misfit is below the required noise level, λ is then increased to find the unique one corresponding to the exact noise level.

Chapter 3

Theory : electromagnetic method

3.1 Generalities

The general principle of an electromagnetic measurement is to record the response of the underground to an induced electromagnetic field. A system composed of - at least - two coils (a transmitter coil and a receiver coil) is generally used (Risch & Robinson, 2001). This principle is illustrated on figure 3.1.

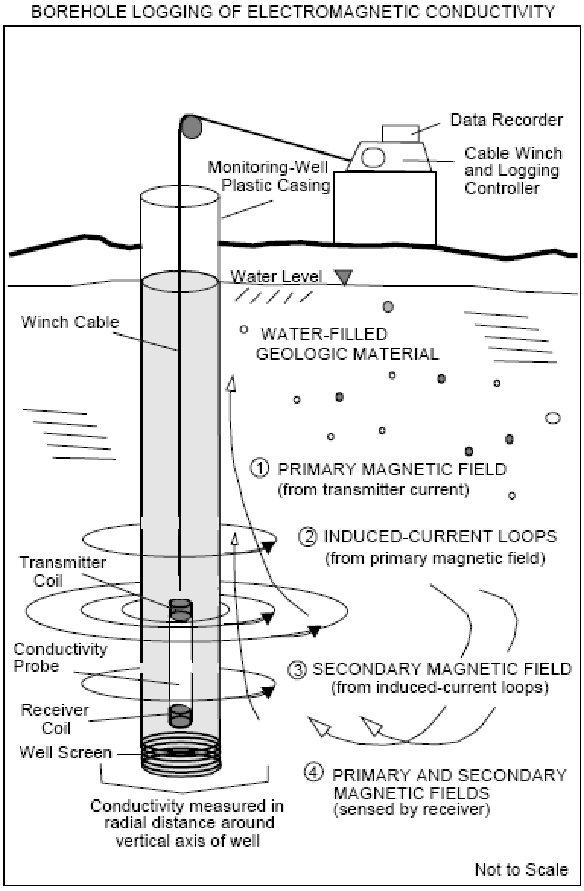

Figure 3.1: General principle of the electromagnetic method (Risch M. & Robinson B, 2001).

The alternating current going through the transmitter coil T_x gives birth to a primary magnetic field H_p $[A/m]$. This field induces small electric currents in the host rocks (current loops). Then, these currents generate a secondary magnetic field H_s. The electromagnetic device simultaneously measures, by the receiving coil R_x, the secondary and primary magnetic fields (McNeill, 1980).

Kaufman & Keller (1983) have shown that the quadrature phase response of a two coil induction logger, with a coil interspacing l, working at the frequency $f = \frac{\omega}{2\pi}$ $[s^{-1}]$ in a homogeneous half-space of conductivity σ $[S/m]$ is given by the general formula

$$\frac{H_s}{H_p} = e^{-p}((1+p)\sin p - p\cos p) \tag{3.1}$$

where $p = \frac{l}{\delta}$ is the induction number and $\delta = \sqrt{\frac{2}{\mu\sigma\omega}}$ is the skin depth, with μ, the magnetic permeability of the air equal to $4\pi 10^{-7}$ H/m[1].

If we work at low values of the induction number such as $p \ll 1$, the secondary magnetic field becomes a simple function of the primary magnetic field

$$\frac{H_s}{H_p} = \frac{\omega\mu\sigma l^2}{2} = p^2 \tag{3.2}$$

In the case of a heterogeneous half-space, the value read by the device is an apparent conductivity σ_a. This value depends on the conductivity distribution around the observation well (if we consider well measurements). If we make the assumption of axisymetry around the well, the expression of σ_a is largely simplified (equation 3.3), because the current in the host rocks is, in this case, composed of horizontal loops centered on the well. In addition, their magnitude is independent of the current in the adjacent loops (McNeill, 1986).

$$\sigma_a = \int_{-\infty}^{+\infty} \int_{0}^{+\infty} \sigma(R,Z) g(R,Z)\, dR\, dZ \tag{3.3}$$

$g(R,Z)$ is a weighting function giving the contribution of each element (R,Z) to the considered measure. It is important to note that R represents the real radial distance divided by the coil interspacing l, and Z the vertical distance to the device divided by l.

3.2 EM39 design

The design of an electromagnetic induction logger is always a compromise between a large lateral investigation zone on one hand, obtained by wide spacing between the transmitter coil T_x and the receiver coil R_x, and a high vertical resolution on the other hand. This latter consideration needs a small coil interspacing.

In the EM39 device, this compromise is achieved by using a spacing of $50cm$. To improve this feature, additional coils are used to focus the measure vertically. Indeed, these coils enable to decrease the sensitivity to the fluid contained in the borehole, to increase the vertical resolution and to diminish the response to the primary field (McNeill, 1986).

However, the additional coils used to improve the vertical resolution lead to modifications in the law proved by Kaufman & Keller (1983) (equation 3.1). A calibration curve (figure 3.2) is used to correct the values read by the device compared to the true values.

On this figure, curve I represents the apparent conductivity value if the hypothesis of a low induction number is respected. Curve II represents the value read by the device and curve III represents the difference of conductivity between the read value and the true value. For a given apparent conductivity σ_a, we have to add the value σ of curve III to obtain a precise measure (McNeill, 1986).

---

[1] as 1 Henry H is equal to 1 $Ohm.s$, δ is in m and p has no dimension.

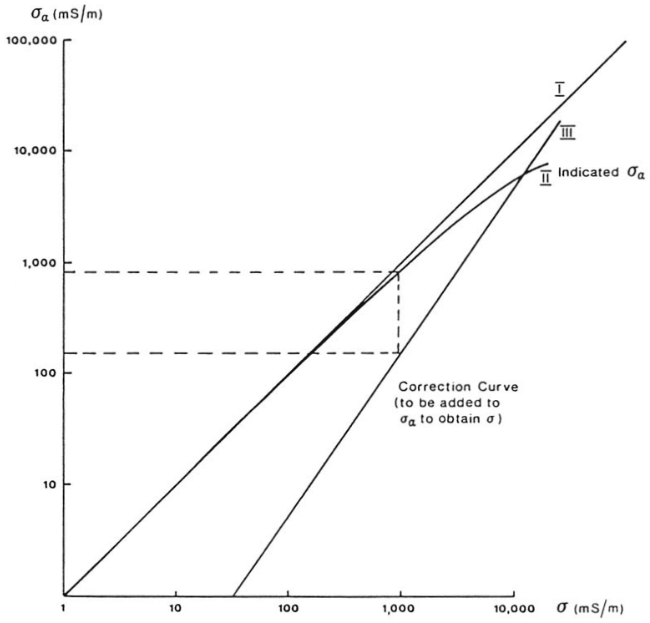

Figure 3.2: Calibration curve of the EM39 device (Mc Neill, 1986).

3.3 Resolution and sensitivity

The radial sensitivity of the device can be obtained by the following expression (equation 3.4; McNeill, 1986), which gives the relative response of an element of thickness dR situated at the distance R of the center of the well. The same definitions are used for R and Z (see equation 3.3).

$$\Phi(R) = \int_{-\infty}^{+\infty} g(R, Z)\, dZ \tag{3.4}$$

Figure 3.3 shows the radial sensitivity of a two coil device (curve 1) compared to the one of the EM39 (curve 2). We note that the EM39 is less sensitive at low distances and has a peak of sensitivity at a value of R equal to 0.56, which signifies a distance of $28cm$. It signifies that the sensitivity is not too high at the borehole itself and thus at the location where the borehole fluid has an influence, which generally displays a widely higher conductivity value than the host rocks (see also Archie's law in chapter 2, petrophysical law) (McNeill, 1986).

By the same way, we can define the vertical sensitivity of the device, by the expression presented in equation 3.5 (McNeill, 1986), which gives the relative response of a horizontal layer of thickness dZ located at a distance Z of the device.

$$T(Z) = \int_{0}^{+\infty} g(R, Z)\, dR \tag{3.5}$$

Figure 3.4 presents this function for a two coil device (dotted curve) compared to the one of the EM39 device. We see that the vertical sensitivity for a device using a focus induction (additional coils) is asymmetric. The width at half maximum is equal to $\Delta Z = 1.3$, which is equivalent to $65cm$. This gives an idea of the vertical resolution of the device (McNeill, 1986).

3.4 Conclusion

This exploration method is well designed to investigate the formation conductivity in wells when the tubing material is non-conductive (for example PVC). Other methods such as an electrical method (for example a log-normal method) can only be used in open holes (with strainers),

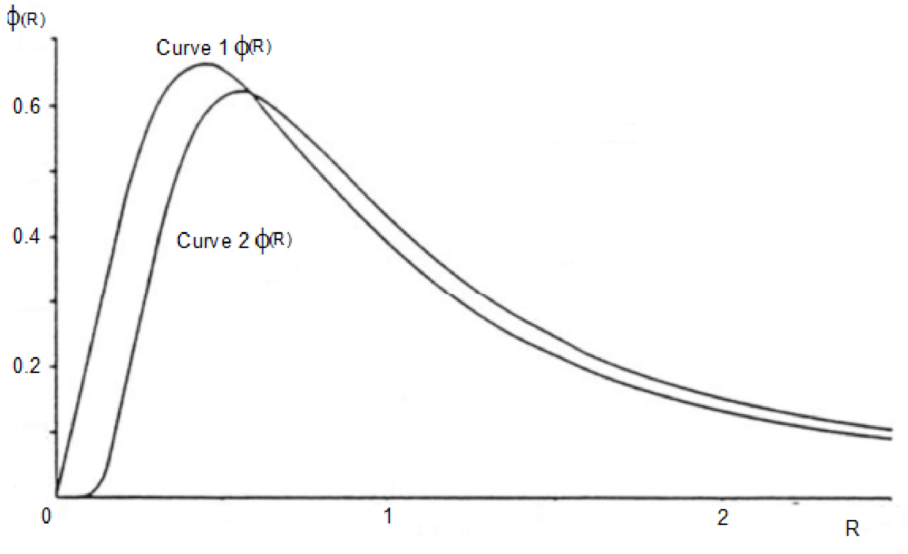

Figure 3.3: Radial sensitivity (McNeill, 1986).

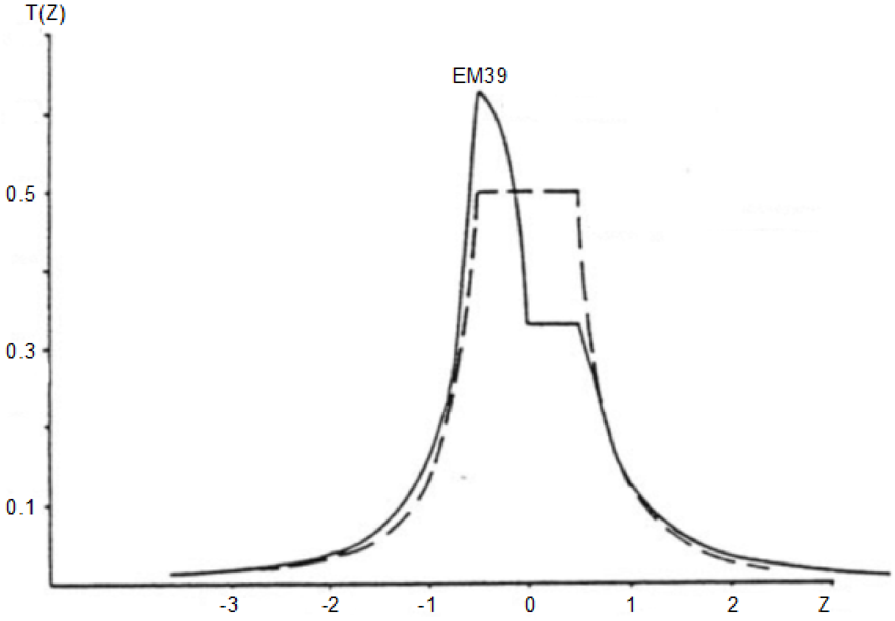

Figure 3.4: Vertical sensitivity (McNeill, 1986).

while the EM39 can be used to measure the conductivity along all the distance from the surface to the bottom of the well.

The EM39 device measures the apparent conductivity of the host rocks and the interstitial water. From figure 3.3 and figure 3.4, we see that the zone of the subsurface explored by each measure is like a torus centered on the well. The conductivity at a low distance (lower than about $15cm$) is not of great importance (position of borehole fluid and perturbed zone), the same can be said about the conductivity of sediments further than $0.8 - 1m$. Vertically, the resolution is about $65cm$. Generally, the measures are taken every $20cm$ (Vandenbohede *et al.*, 2009).

The causes responsible for changes in the apparent conductivity are the same that the ones exposed for the electrical method but the volume support of the method is different, several m^3 for DC, varying with depth and dm^3 to m^3 for the EM39.

Chapter 4

Synthetic case studies

4.1 Introduction

This chapter benchmarks our implementation of the new geostatistical regularization. Since, few studies have explored this possibility for electrical resistivity tomography (Chasseriau & Chouteau (2003) and Johnson *et al.* (2007) explored it for other geophysical methods), we needed to explore the possible effects of this type of inversion and the problems that could be encountered.

In this chapter, we will highlight the important points of the inversion using the covariance matrix. The aim was first to stay within reasonable distances from the field case, reason for which we used data from the Westhoek area to create a model (profile 1, see chapter 7). However, different types of models were also tested to draw more general conclusions. In addition, these synthetic cases enable us to learn the different steps of data processing to apply them later on real data. Information contained in this chapter being quite dense, a detailed conclusion summarizes the results at the end of the chapter.

4.2 Synthetic models

Three different models were created to test the geostatistical regularization. The first model was based on resistance data collected in the Westhoek. The second was derived from similar data, but using another building method (see sections below), and the third was corresponding to another salt water intrusion issue. All models were built on a grid of 153×42 elements (cell dimensions were $1.5m \times 1m$). Then, the same type of grid was used with the program CRTOMO for the inversion process; except for the deepest five lines (a higher thickness was implemented). However, this difference does not have a great significance as the sensitivity is very low at this depth. Cells located outside the profile (before the first electrode and after the last one) also had a higher width, but the influence is very low, too. Topography was neglected to simplify the models. The whole process (variogram modeled with VarioWin (Pannatier, 1996), kriging with S-GEMS (Remy, 2008), etc.) was based on the logarithm of resistivity values, as the inversion (CRTOMO) proceeds with these values.

4.2.1 First model

For the first synthetic case, a random set of points was selected from a previous inversion carried out with RES2DINV (Geotomo software, 2005). This result came from an inversion using reciprocal error as an error estimation with an anisotropy ratio of 2 in the horizontal direction. The anisotropy was evaluated by modeling horizontal and vertical variograms of this set of points and compared them with EM39 conductivity measurements made in boreholes in the Westhoek area (examples are given in appendix B). Since the vertical ranges were quite similar

(7.5m), a synthetic model was created by kriging (ordinary kriging) the selected points with the variogram deduced from the boreholes with the S-GEMS software (Remy, 2008). The variograms derived from the set of points were not used, because during the real inversion process, the aim was to use the EM39 hard data to obtain information on correlation between points. For the horizontal range, the same ratio as in the random set of points (4) was taken (borehole data do not give information about horizontal correlation in this case). Spherical variogram models were used to create the synthetic case study with a vertical range equal to $7.5m$, a horizontal range equal to $30m$. The sill value was taken equal to 0.3, there was no nugget effect.

Gaussian models seemed to fit variograms deduced from boreholes better than spherical ones. However, due to numerical problems, the convergence was not always ensured with these Gaussian variograms[1]. It is the reason why the use of spherical models was preferred for this synthetic case.

This synthetic model is shown on figure 4.1 (top). We see that this model is very smooth. Indeed, it is calculated by ordinary kriging based on points coming from a smoothness constraint inversion and it displays higher length of correlation than expected by the variograms.

As such a problem could appear in reality (the experimental variogram is different from the real one), it was decided to study this synthetic case with the parameters given above. Obviously, some inversions will be also carried out with the effective ranges (66 and $19.5m$ instead of 30 and $7.5m$). This problem was one of the reasons why other models were created, this time with the good characteristics.

If we want to use the covariance matrix regularization, we have to decide if the assumption of stationarity can be made. It is necessary to make this assumption to calculate the covariance function (or the variogram). It is important to say again that we cannot demonstrate the stationarity of a field, it is a decision of the operator. In this synthetic case, and thus more generally for the Westhoek site (see chapter 6 for a complete description of the site), we can suppose that the stationarity is verified. At least, we can assume that the value of $\gamma(h)$ depends only on h and not of the position in the field (hypothesis of intrinsically stationarity). If we consider the site without the intrusion, we are in a quite homogeneous dune area, except for the clay layer, whose position is not perfectly known. The stationarity does not seem to be a strong hypothesis in this case.

Salt water intrusions modify the situation slightly. In a case where the intrusions result from a large scale equilibrium, such as the traditional limit encountered in coastal aquifers, the stationarity is clearly difficult to justify as it is expected to have low resistivity values on one side and higher on the other side of the intrusion. The expectation of the random variable should be different according to the location considered. Here, we are in a case where no equilibrium is reached. Infiltrations of sea water occurred for 6 years during high tides and storm events only. In addition, the inlets are silting up and the infiltration rate diminishes. Once in the dune aquifer, salt water is submitted to diffusion, gradient and other hydrogeological phenomena. In my opinion, it is not exaggerated to accept the assumption of stationarity in this case.

All the results obtained in the next sections for this synthetic case are summed up in table 4.1 and table 4.2 at the end of the chapter.

4.2.2 Second model

Here, the synthetic model was obtained using a Gaussian simulation rather than ordinary kriging in order to avoid the problems described above (the synthetic model respects the variogram parameters) and to test the use of a Gaussian simulation as a prior model. This model is presented on figure 4.3. We can mainly see the same features, but the model is not as smooth.

---

[1] At the time of writing, we still have convergence issues in the inversion process.

It may be a less probable solution in the case of salt water intrusion, but it enables to see other characteristics about regularization tools.

The aim of a simulation is to produce a field with the same variogram characteristics and the same histogram as the data used to build it. Simulations can be conditioned or not. The only difference between them is that a conditioned simulation also respects the observation data points (Marcotte, 2009). In this case, the algorithm used to produce the simulation was the sequential Gaussian simulation algorithm from S-GEMS software (Remy, 2008).

The first step is to transform the conditioning data into a Gaussian distribution. It is always possible to realize that by applying the relation

$$Z_g = \frac{Z - \mu}{\sigma} \tag{4.1}$$

where Z is the value of the variable and Z_g the value of the variable after transformation, μ is the mean and σ is the standard deviation.

After simulation, the inverse transformation is applied to obtain parameter values in the correct range of variation. It is important to note that the simulation will respect the variogram of the transformed distribution. However, it is not sure that the transformation used will enable to fit the variogram of the true distribution.

To produce one realization, a random path is created to visit all the points that have to be calculated. At one point, all the data and the previously calculated points are used to carry out an ordinary kriging. The result gives a kriging result and a variance that are considered to be the expectation and the variance of the random variable at this point. Then, a random value is taken in this distribution and becomes the simulated value at this point (Marcotte, 2009).

As this model is "artificially" built using a simulation based on a variogram, there is no problem to assume the stationarity in this case. It will be used to show the possibility to use a Gaussian simulation as a prior model. Table 4.3 sums up the results for this synthetic model.

4.2.3 Third model

As the first synthetic case was quite particular, in the sense that is was extremely smooth, it was decided to study some features again on another synthetic case. The true model is presented on figure 4.4 (top). The dimensions of the first synthetic case are kept. It also corresponds to a model of salt water intrusion, but the geometry is quite different. The intrusion is located on the right side where the resistivity values are low. The yellow bodies with a resistivity value around $10^{0.8}\,Ohm.m$ correspond to clay, whereas the other parts are characteristic of sand. It is important to note that the range of resistivity value is more limited than in the first synthetic case.

Vertical and horizontal variograms were calculated based on this model. The parameters of the spherical variogram are the following ones: the sill value, taken equal to the variance, is 0.29; the vertical range is equal to $40m$ and the horizontal range is equal to $80m$. It is important to note that it was very difficult to find a good model for these variograms; these parameters are only estimations to represent the structure of the model.

It is probable that the assumption of stationarity is not verified for this synthetic case. This model was built according to a hydrogeological model (stationarity was verified) and then the sea water intrusion was imposed on the right side of the model. One could question the pertinence of assuming stationarity if it is not true. The answer is pragmatic, we simply cannot do anything else if we want to use the covariance matrix regularization. It is the same problem when we use the smoothness constraint inversion when we know that the subsurface is not smooth.

This second synthetic case was carried out with noisy data only (random noise equal to 3%). Table 4.4 sums up the results obtained. Note that the model misfits (see section below) are only calculated in terms of resistivity because some logarithms were equal to zero, which did not enable to calculate the model misfit, since this logarithm is the denominator in equation 4.4. In addition, some resistivity values were very low and led to very high relative error.

4.3 Synthetic data and inversion parameters

Two different sets of data were created for the first true model, the first without noise and the second one with a 5% random noise. A short discussion will show the effect of the noise on the results. However, noise is always present in the data. In consequence, for the second and third models, only noisy data sets were created with respectively 5 and 3% noise.

To assess the advantages and disadvantages of the inversion using the covariance matrix, several inversions were done. First, a classical smoothness constraint inversion was carried out to compare with the geostatistical regularization. For this one, two crucial aspects to determine were the importance of the prior model and the role of variogram parameters.

In the case studied in this master thesis, anisotropy plays an important role. The correlation between two points is greater in the horizontal direction than in the vertical direction. However, it is difficult to assess precisely the value of the anisotropy. It was thus important to know if a variation of the anisotropy led to big differences in the inverted model.

In contrast with the smoothness constraint inversion, the prior model plays an important role. Indeed, in most cases, a homogeneous model is used as a prior model. It signifies that the regularization term in the objective function, since there is no gradient in the prior model, becomes

$$||\mathbf{W_m}(\mathbf{m} - \mathbf{m_0})|| = ||\mathbf{W_m}\mathbf{m} - \mathbf{W_m}\mathbf{m_0}|| = ||\mathbf{W_m}\mathbf{m}|| \tag{4.2}$$

However, a homogeneous model does not signify that covariance matrix is a diagonal matrix. Indeed, a correlation may exist between some parameters. In this case, it is thus important to choose a prior model that represents the true data well and does not influence the results badly.

The parameters deduced from boreholes concern the vertical range and the sill of the variograms. They only constitute an estimation of the real parameters, some uncertainty exists and it was thus interesting to know how it would influence the inverted model.

By studying the various cases, the aim was to highlight the more important points when a geostatistical regularization is used. Since many inversion runs were carried out, we summarized the results in the following sections and in table 4.1 to 4.4.

4.4 Results

The CRTOMO program enables to perform all the inversions until the data misfit reaches the targeted level.

The model misfit estimation (equation 4.3) presented by Amidu & Dunbar (2008) was used to compare the different results together. In this calculation, resistivity values are used, but a model misfit based on the logarithm of resistivity was also used as the inversion process is made on the logarithm (equation 4.4, this one will be only presented in tables to simplify the interpretation). The trends are the same, but differences can sometimes appear. Since the sensitivities are higher near the surface, a specific model misfit presents the results for the first twenty meters.

$$M_{misfit}(\%) = 100 \times \sqrt{\frac{\sum_{i=1}^{N} \left[\frac{\rho_{calc,i} - \rho_{true,i}}{\rho_{true,i}}\right]^2}{N}} \tag{4.3}$$

$$M_{misfit}(\%) = 100 \times \sqrt{\frac{\sum_{i=1}^{N} \left[\frac{\log \rho_{calc,i} - \log \rho_{true,i}}{\log \rho_{true,i}}\right]^2}{N}} \tag{4.4}$$

Sometimes, the inverted model or the inverted model error is also displayed to see where the model was well found or not. This can also give an idea of the resolution of the inversion process. The results are going to be presented mostly for the noisy data. Indeed, in reality, noise is always present and it is preferable to work with this case.

4.4.1 Smoothness constraint inversion

The smoothness constraint regularization is the most used regularization technique in electrical resistivity tomography, and in geophysics in general. This section will present the smoothness constraint solution for the three synthetic models. The anisotropy factor used is chosen equal to the ratio of horizontal and vertical ranges.

Model 1. Figure 4.1 shows the result for the first synthetic case and figure 4.2 displays the percentage change difference with the true model. The model misfit is equal to 40.03% (38.59% for the first 20 layers). The model misfit is less favorable than in the case without noise (table 4.2). This result was expected as the noise increases the difficulty to find a good solution. If we are only interested in the structure of the solution, we see that the smoothness constraint solution is quite good. Indeed, the shape of the intrusion is similar to the "true" one and no artifact due to the noise is present. This result can be obtained because the level of noise is known *a priori*. This enables us to stop the inversion before the creation of artifacts of inversion.

It is important to note that the true model is very smooth. Indeed, conditioning data were taken from smoothness constraint inversion results. In addition, the kriging method leads to a smooth structure. It was thus expected that the smoothness constraint inversion gives quite good results.

On figure 4.2, we see that there is not a clear variation of the error in depth. Some parameters are also close to the true value in depth. However, the most well resolved parameters are found near the surface. The error appears to be greater in the area of the salt water, represented by the low resistivity values between -5 and $-10m$, where resistivity is overestimated. This can be explained by the fact that a small change of a low resistivity value leads to high relative error whereas the same error on a high resistivity value leads to low relative error.

It is not surprising to observe greater differences between the true and the inverted models on the sides of the section, as the data are less constraining in these zones. It is important to say that, even without noise, the model is not perfectly solved, because the problem is ill-posed and underdetermined. With noise, the error tends to be increased; however, the distribution is quite similar, what proved that a great part of the error is due to the inversion process.

Model 2. The results of the smoothness constraint solution for the second true model are presented on figure 4.3. We directly detect the limitations of this type of solution in the case of such a structure. Only the bigger structures located in the first meters are found by the inversion process and are logically smoothed. The model misfit is equal to 323.4% and 230.06% for the first twenty layers. The small structures were expected to miss because the inversion process smoothes the structures. We can thus say that if we expect the true model not to be smooth, this solution only gives an idea of the principal structures.

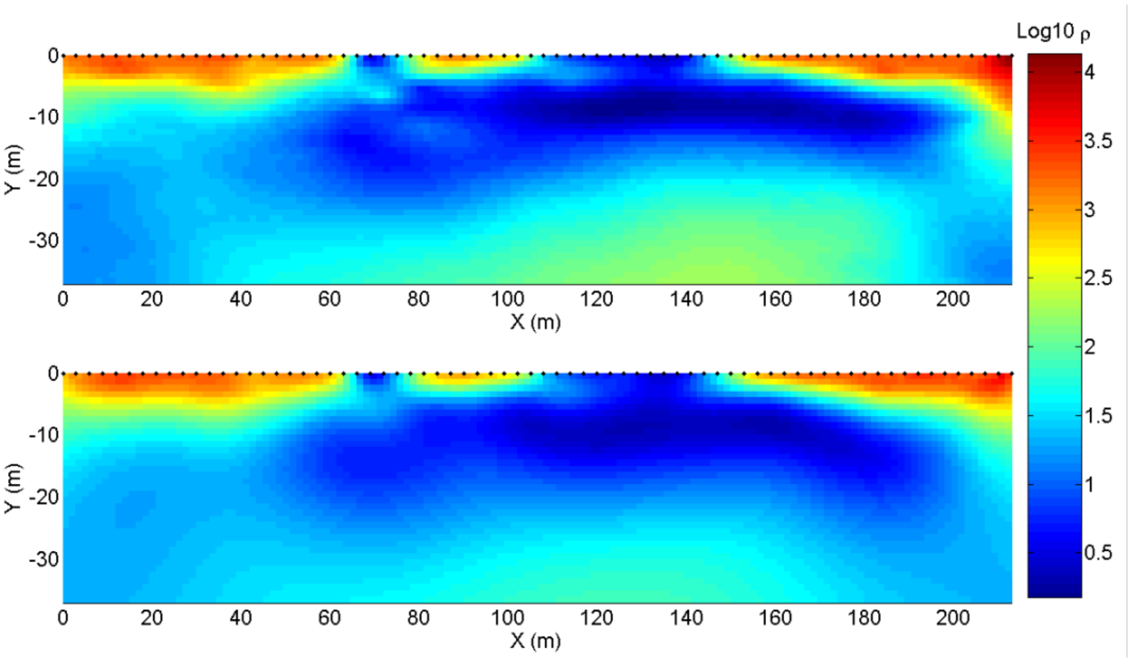

Figure 4.1: First true model (top) and smoothness constraint solution (noisy data set) (bottom) (scale in $\log \rho\,[Ohm.m]$).

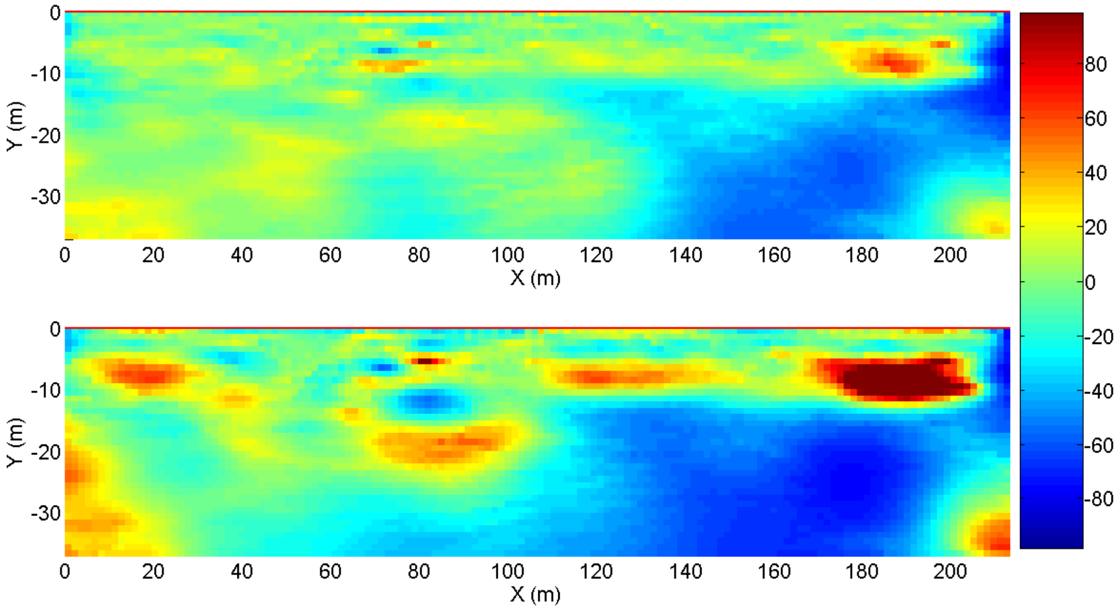

Figure 4.2: Percentage difference in resistivity with the first true model for the smoothness constraint inversion without (top) and with (bottom) noise (in %).

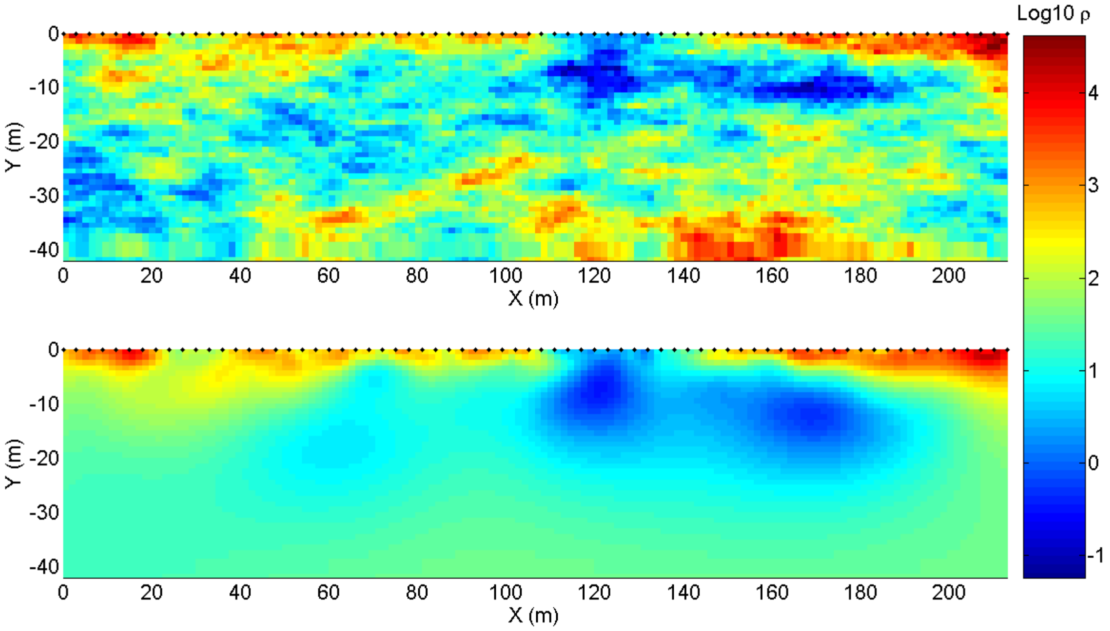

Figure 4.3: Second true model (top) and smoothness constraint solution (bottom) (scale in $\log \rho \, [Ohm.m]$).

In addition, the parameters of the solution are very different from the ones of the true model. Indeed, both vertical and horizontal ranges are more than double (table 4.3). It signifies that, in this case, the smoothness constraint inversion minimizes the gradient too much.

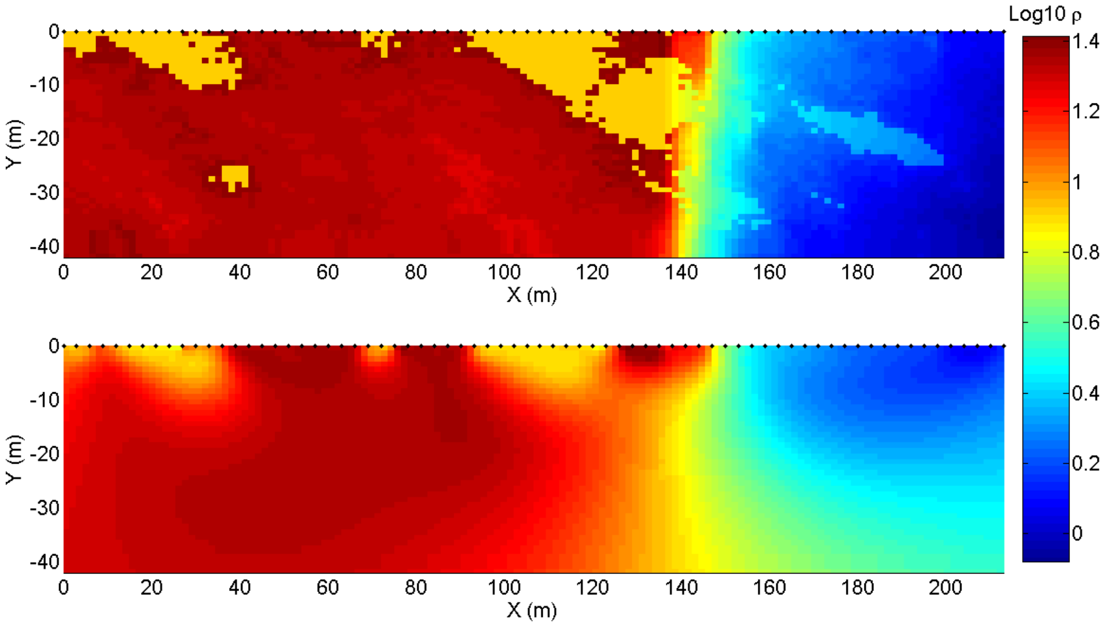

Figure 4.4: Third true model (top) and smoothness constraint solution (bottom) (scale in $\log \rho \, [Ohm.m]$).

Model 3. The third true model is between the two first ones. It displays sharper structure than the first one, but there are not as small as in the second one. The results of the smoothness constraint inversion are presented on figure 4.4.

We see that most of the structures are found by the inversion. Particularly, the position of the intrusion is correct at the surface; however, the accuracy of the detection decreases in depth with the resolution. In the same way, the clay bodies are detected near the surface, but it is not the case deeper.

We directly see with this result that the true model is further from the smoothness constraint model than in the first synthetic case study, because limits between geological bodies are sharper. The model misfit is equal to 64.3% (30.15% for the 20 first layers). We see that there are fewer subtleties in the inversion results due to the smoothness constraint and that inverted values are sometimes quite different from the true one.

4.4.2 The role of the prior model : the smoothness constraint solution as a prior model

As explained before, the prior model plays a great role in a geostatistical regularization. Ideally, the prior model should be very close to the true model. From a statistical point of view, the prior model should contain the mean of the density probability function (if it is assumed that this density probability function is Gaussian) (Tarantola, 2005). In the next sections, different types of prior models will be investigated.

First, an inversion using the smoothness constraint results as a prior model was carried out. This type of prior model can be easily justified in practice. Indeed, a "traditional" inversion without changing any parameters is often done to have a first idea of the results. In addition, we can hope that in some cases, this solution is close to the true model and that the parameters are close to the mean of the density probability function. However, in our second synthetic model, it does not seem useful to try this type of prior model as the smoothness constraint solution is relatively bad.

Model 1. For the first case, the model misfits are quite similar to the ones observed with the smoothness constraint inversion. With noise, an improvement is detected as the model misfit is equal to 38.96% and 27.25% for the first twenty meters. This latter result shows an improvement of about 10%. If we only look at the solution, few differences are detected; it is why figure 4.5 presents the percentage difference with the true model. We see that the anisotropy included in the inversion is also found in the results. In the first layers, the error is correlated in the horizontal direction; the distribution seems less random than for the smoothness constraint, because a structure was imposed by the variograms. Errors are less high in the area of the salt water, we can thus hope that this technique is able to improve the results for the salt water detection. We observe that the same areas have a high error in comparison with figure 4.2. However, the covariance matrix regularization permits to decrease the value of this error, sometimes more than twice. It seems that, in this synthetic case, this type of regularization allows a reduction of the effect of noise on the model misfit. The advantage is that we used hard data derived from borehole measurements to achieve this, while an assumption of smoothness is needed for the first type of inversion.

Model 2. This type of prior model was not tested for this synthetic case.

Model 3. For this synthetic case, the results are illustrated on figure 4.6. They are very close to the one shown on figure 4.4. The model misfit is equal to 63.75% and 30.26% for the first 20 layers. It seems that the inversion process leads in this case to an inverted model very close to the prior model. This is confirmed by the value of the regularization parameter, λ, superior to 12000. A high weight is given to the regularized term and thus to the prior model. As the prior model enables to fit the data to the level wanted, the inversion process leads to a solution equal to the prior model. There are no advantages to use this type of prior model as the true model is far from a smooth model.

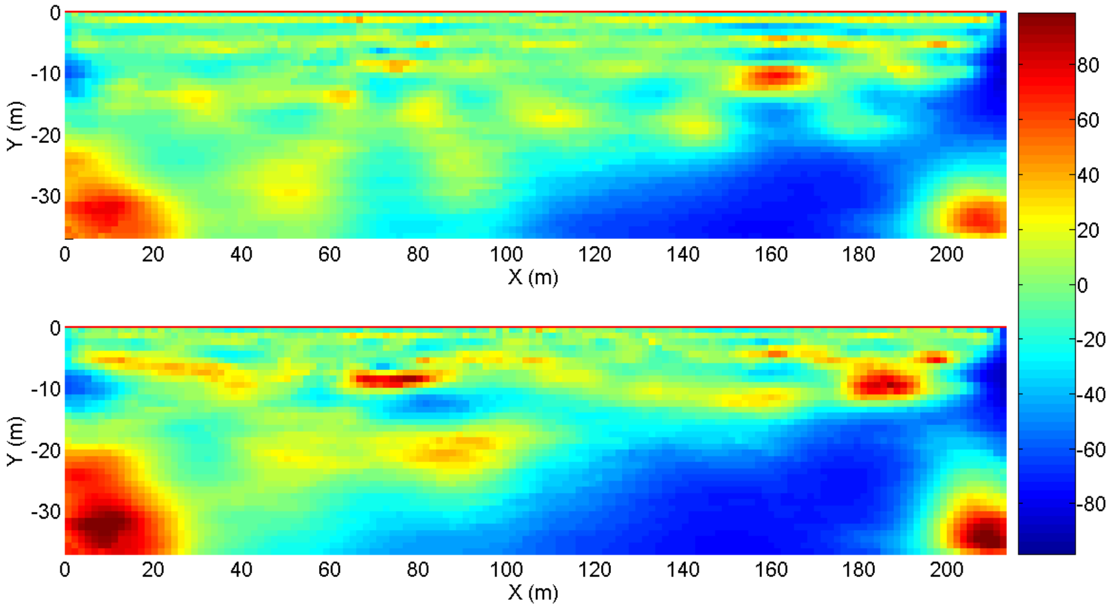

Figure 4.5: Percentage difference in resistivity with the first true model for the inversion with the smoothness constraint solution as a prior model, without (top) and with (bottom) noise (scale in %).

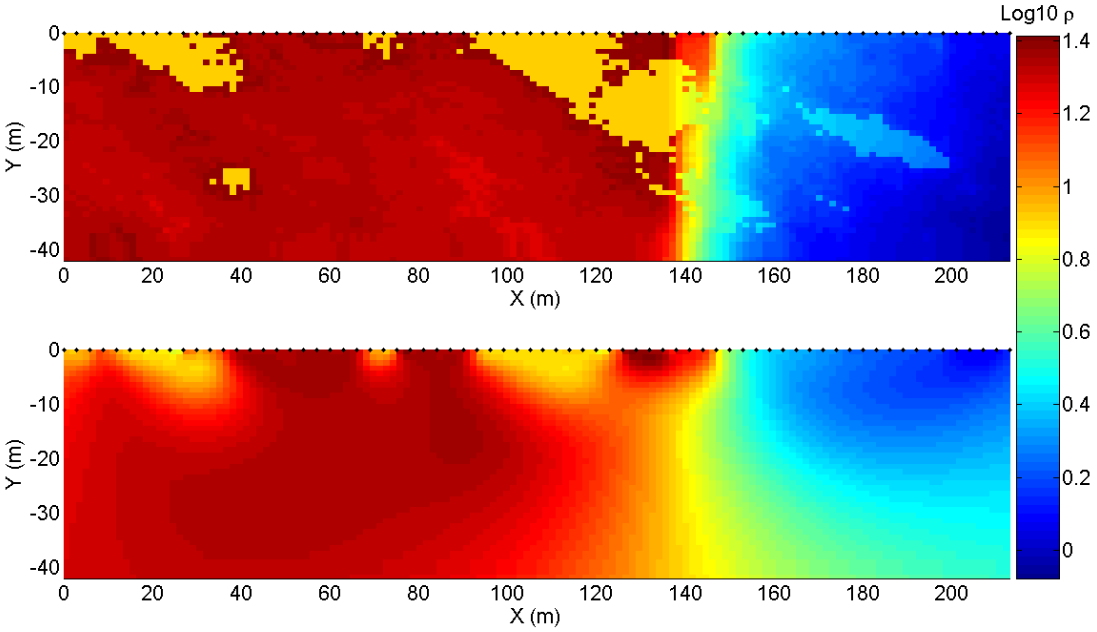

Figure 4.6: Third true model (top) and inversion with the smoothness constraint solution as a prior model (bottom) (scale in $\log \rho \, [Ohm.m]$).

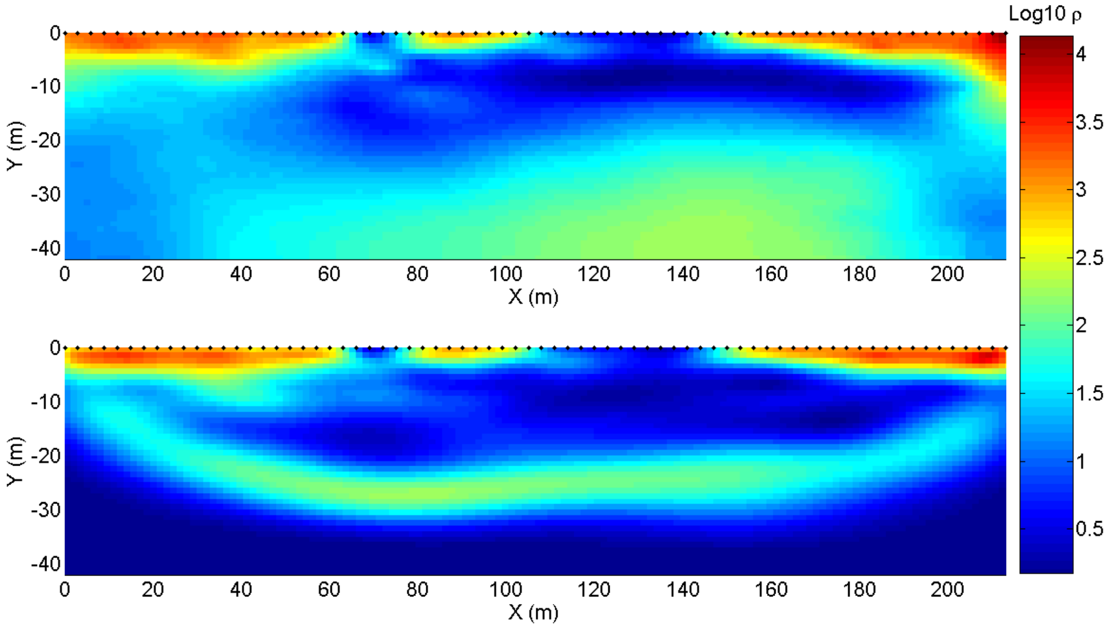

Figure 4.7: First true model (top) and inversion with a prior model equal to zero (bottom) (scale in $\log \rho\,[Ohm.m]$).

4.4.3 The role of the prior model : prior model equal to zero

A very simple solution is to carry out a regularized inversion with a prior model equal to zero. This type of prior model is difficult to justify statistically or physically, but it will allow us to show an important feature of this type of regularization. Therefore, we only need to illustrate our purpose for one model, the first one. The covariance matrix is then directly applied to the model parameters.

Figure 4.7 shows the true model and the result of the inversion. With the noisy set of data, the model misfit is 103.64% (45.79% for the first 20 layers).

We see that the structure in the first 20 meters below the surface is quite well found if we compared it to figure 4.1. It is quite interesting to note the shape of the section; it has a "banana shape". When a prior model equal to zero is used, the inversion result gives a slight idea of the sensitivity. Indeed, if a parameter does not influence the data, the data misfit, i.e. the first term of the objective function, does not change when this parameter changes, the sensitivity is then very low. For this parameter, the second term of the objective function is minimum if the inverted model $\mathbf{m}$ is equal to the prior model $\mathbf{m_0}$.

In this case, the resistivity value decreases rapidly below $30m$ (less on the left and right sides of the section). If this case shows this phenomenon clearly, it is easy to understand that it also appears for other prior models. For example, if another homogeneous prior model is used, the resistivity values are going to tend to the homogeneous value. Results for the other models are not presented as this type of prior does not have a statistical meaning. However, model misfit results are present in the respective tables.

4.4.4 The role of the prior model : homogeneous prior model

If it seems quite logical to obtain better results with a prior model close the true one than a completely different one, it is easier to choose a homogeneous model, because it does not require a first inversion or a detailed analysis of the data. In addition, we have seen that the prior

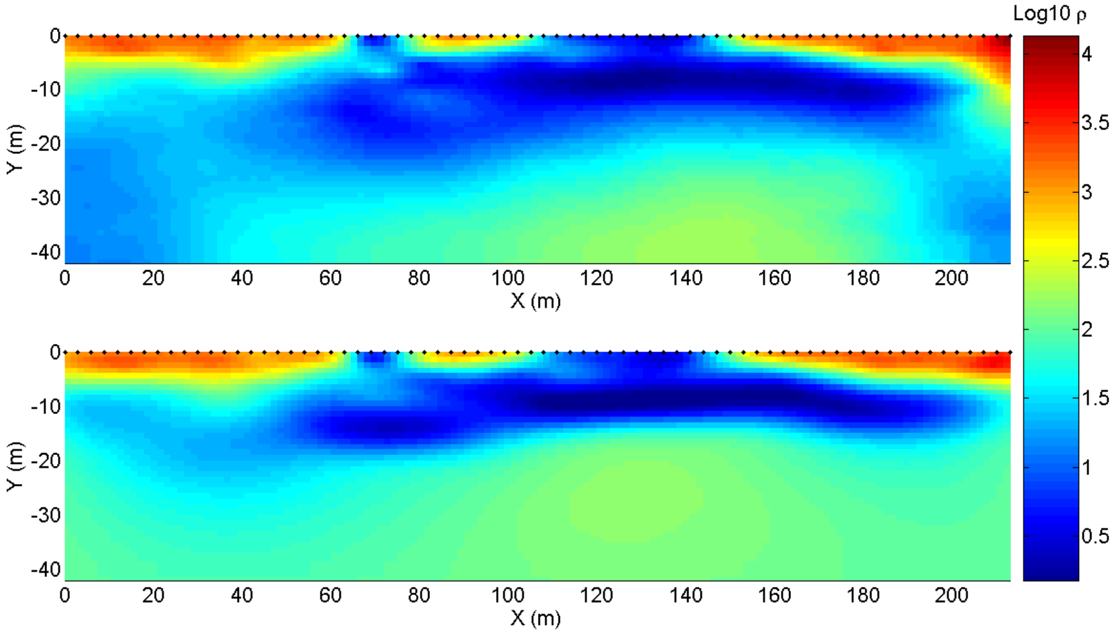

Figure 4.8: First true model (top) and inversion with a homogeneous prior model (bottom) (scale in $\log \rho\,[Ohm.m]$).

model can influence the inversion process badly if it fits the data. In addition, statistically, a homogeneous prior model is also easily justified.

Indeed, we have seen that the prior model should be the mean of the probability density function (Tarantola, 2005). When we assume that the field is stationary, it means that the expectation $E\left(Z(x)\right)$ is independent of x (Gneiting et al., 2000). Thus, a homogeneous model equal to this expectation seems statistically correct. The problem is to determine this value.

In this case, a homogeneous model equal to the average resistivity value of the results of the smoothness constraint inversion ($106\,Ohm.m$ for the first case) or the average resistivity value of the true model ($12.7\,Ohm.m$ for the third case) was chosen. Another possibility is to choose the mean apparent resistivity of the measurements, which could give a good estimate (this value is often taken as a starting model during the inversion process), or a value determined by borehole data (background value). It is important to note that a homogeneous prior model does not verify the variogram parameters at all.

Model 1. Results for the first case are presented on figure 4.8. The model misfits are only equal to 181.88% and 155.22% for the first twenty meters. We see that the difference with the true model is high under the low resistivity value zone. This can be explained by the fact that during the inversion, the algorithm tries to fit the statistics corresponding to the variogram, but in comparison with a homogeneous model. It signifies that the prior model which is not so good in this case compared to the smoothness constraint solution cannot correct the error made on the variogram parameters. Indeed, if we look at the variogram parameters of the solution (table 4.1), they are closer to the ones imposed in this case than in the case of the smoothness constraint solution. It signifies that, when the good parameters are imposed (see section about the range value) and that the correlation length is smaller, a homogeneous prior model could find the structure better than a smoothness constraint solution. Indeed, the true intrusion is expected not to be as smooth as the one of the synthetic case (vertical range about $8m$).

Below $-20m$, the inverted model is very close to the prior model with an almost constant resistivity value around $100\,Ohm.m$. This observation is the same that with a prior model equal to zero ("banana" shape).

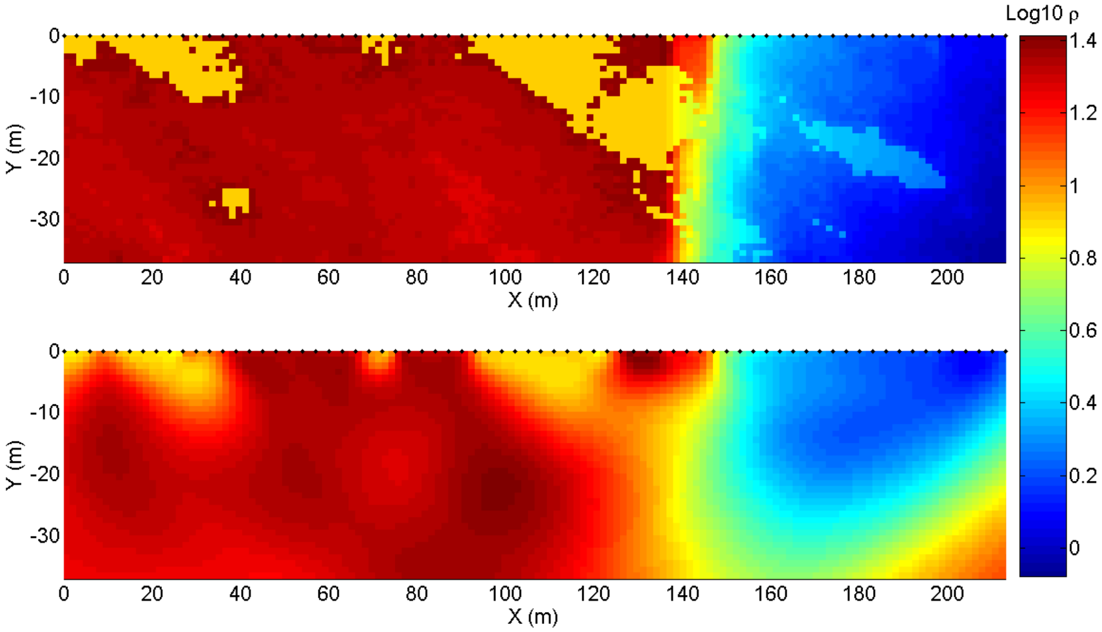

Figure 4.9: Third true model (top) and inversion with a homogeneous prior model (bottom) (scale in $\log \rho\,[Ohm.m]$).

Model 2. A homogeneous prior model was not tested in this case.

Model 3. In the third synthetic case, the model misfits are also less good than for the smoothness constraint solution (171.62% and 48.04% for the first 20 meters). The results are shown on figure 4.9. This difference can be explained by the sensitivity of the parameters. Indeed, we observe the traditional "banana shape", below which the inverted model tends to the prior model. It seems that the true model is such that this shape is asymmetric; the investigation goes deeper to the left part of the section, because the current lines are focused in the low resistivity zone. So, when the model misfit is calculated, the values on the bottom-right corner are quite high, whereas they would be very low with a prior model equal to zero. This explains why this latest prior model gives better results. The model-misfit for the 20 first layers is also slightly penalized.

If we compare this solution with the smoothness constraint one (figure 4.4), the model misfit is worse, but if we look only at the structures, it seems that there is an improvement, especially for the position of the transition between salt and fresh water. This is due to the covariance matrix which controls the structure. Obviously, it is very difficult to quantify any kind of structure misfit.

4.4.5 The role of the prior model : other types of prior model

Model 1. Other types of prior model were also tested, trying to include much information as possible. For example, we tried to include borehole data directly in the prior model. A possibility is to impose these values in addition to a homogeneous prior model. If there is only one well with available data, an obvious solution is to apply the resistivity values laterally at their depth down all the section. It can be a good approximation when the subsurface has a horizontal stratification. When there is more than one borehole, we have the possibility to apply lateral changes in the prior model. The hard data is fixed at its position and an interpolation is carried out between the different boreholes.

Model 3. In this case, since the field did not seem to be stationary due to the salt water intrusion, a homogeneous prior model divided into two zones was applied. The ranges were kept

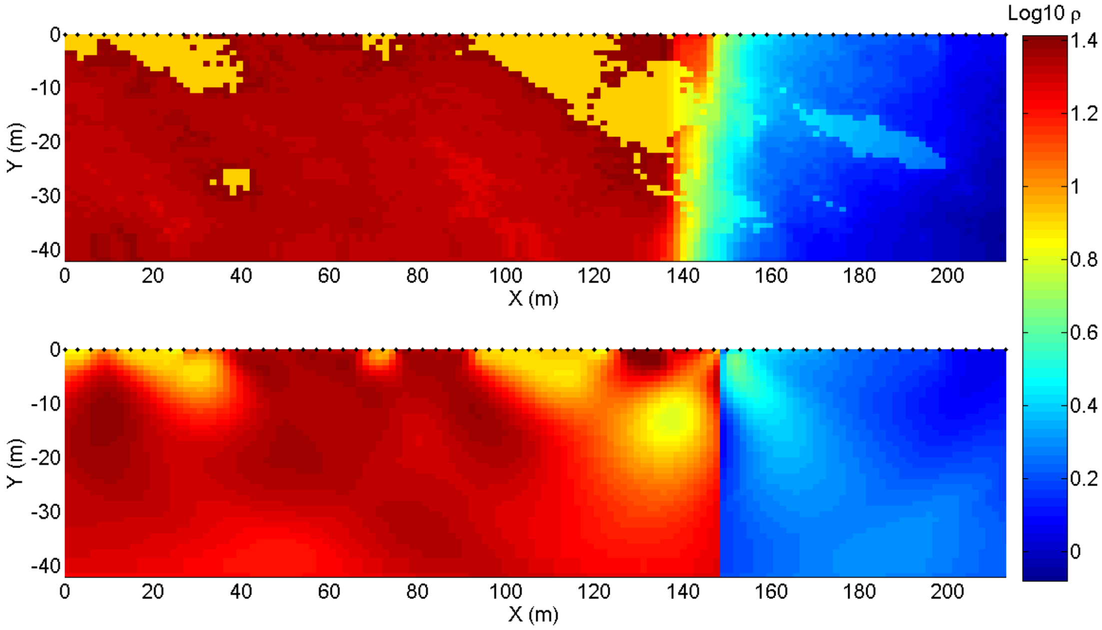

Figure 4.10: Third true model (top) and inversion with a homogeneous prior model equal to $19\,Ohm.m$ on the left and $1.55\,Ohm.m$ on the rigth (bottom) (scale in $\log\rho\,[Ohm.m]$).

equivalent in both zones, as the hydrogeological parameters are the same. The abscissa $150m$ was the limit to impose a mean value of $19\,Ohm.m$ on the left side and a value of $1.55\,Ohm.m$ on the right side. These values correspond to the mean values on these two parts. Results are presented on figure 4.10. The model misfit is equal to 44.37% and decreases to 28.27% for the first twenty layers. That corresponds to a good improvement compared to a simple homogeneous model or the smoothness constraint solution. The mean values of the random variables are thus really different on left and right sides of the section and the problems highlighted in figure 4.9 are resolved.

However, we cannot be satisfied with the results of this inversion. Indeed, we see on figure 4.10 that the limit imposed in the prior model is completely conserved in the inverted model, whereas a smoothness transition is expected and found with completely homogeneous model. This problem was also observed when a borehole data based prior model was used for **model 1**. The conclusion is that it seems dangerous to impose sharp limits on the prior model, because they are conserved in the solution, but that a homogeneous value different from the mean value calculated on all the field is able to improve the misfit.

Another possibility is to use a Gaussian simulation as a prior model. This type of prior model has many advantages: it respects the variogram parameters used to build it, it can be conditioned by data, but avoids sharp limits, as a correlation length is imposed. The main disadvantage is that the value of one parameter is not the mean value of the probability density function but only one realization. We could solve this problem by doing a lot of simulations, but it would cost a lot of calculation time.

Model 2. An example is given by the second synthetic case, where both the true model and another Gaussian simulation were tested as two prior models.

When the true model is used, the solution is very close to the true one, differences appear due to the noise. Obviously, we will never have the true model being prior in reality. Results with another Gaussian simulation are displayed on figure 4.11. Visually, the results look better than the inversion with a homogeneous prior model, because small structures are found in the

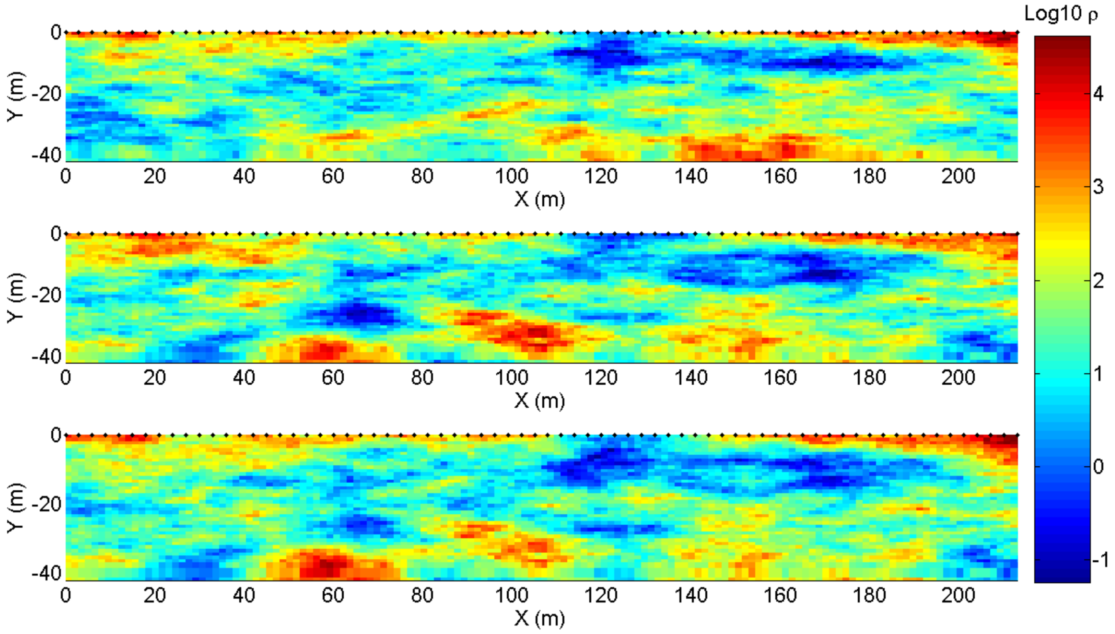

Figure 4.11: Second true model (top), prior model (middle) and inverted model (bottom) (scale in $\log \rho\,[Ohm.m]$).

solution. In addition, the variogram ranges of the inverted model are closer to the true ones than other solutions (except when the true model was used as a prior).

Quantitatively, the model misfits are relatively weak. Only 511.91% for the first twenty layers, even if the solution is influenced by the data. For the whole model the result is catastrophic: 1237.5%. Such values are certainly due to the fact that smaller structures are found in the inverted model, but if they are not exactly located, that can lead to a very high model misfit. We can suppose that this type of model misfit is not a good estimate for this case. Some kind of "structure misfit" should be better. Deeper down, the inverted model is very close to the prior model. Even if the solution looks quite satisfying, it is not possible to interpret the inverted model in this zone, because the prior model is only one possible solution among a lot.

Such kind of prior model can be interesting, but it is important to take into account the fact that the prior model can influence the inversion badly and it is not always easy to see. For example, in this case, we see that the influence is great in depth, but also appears above (shape of the intrusion between 140 and 180m in the first 20 meters). In this case, it is not easy to say clearly where the prior model becomes too important. With such a prior model, it thus seems necessary to carry out several inversions and to take all of them into account to obtain a reliable solution (a mean solution), even if it costs more calculation time. This possibility will be discussed in chapter 8.

4.4.6 Effect of the sill value

The previous sections showed the features linked with the prior model. In the two following sections, the role of the sill value of the variogram and the role of the variogram ranges (and thus of the anisotropy) will be investigated.

Concerning the sill, we can see in the different tables with the results that every time the sill was increased, the inversion led to better results in terms of model misfits. The improvement was such that in many cases a higher value of the sill was directly taken to carry out the inversion (third synthetic case). It was especially the case when the prior model was homogeneous, but it

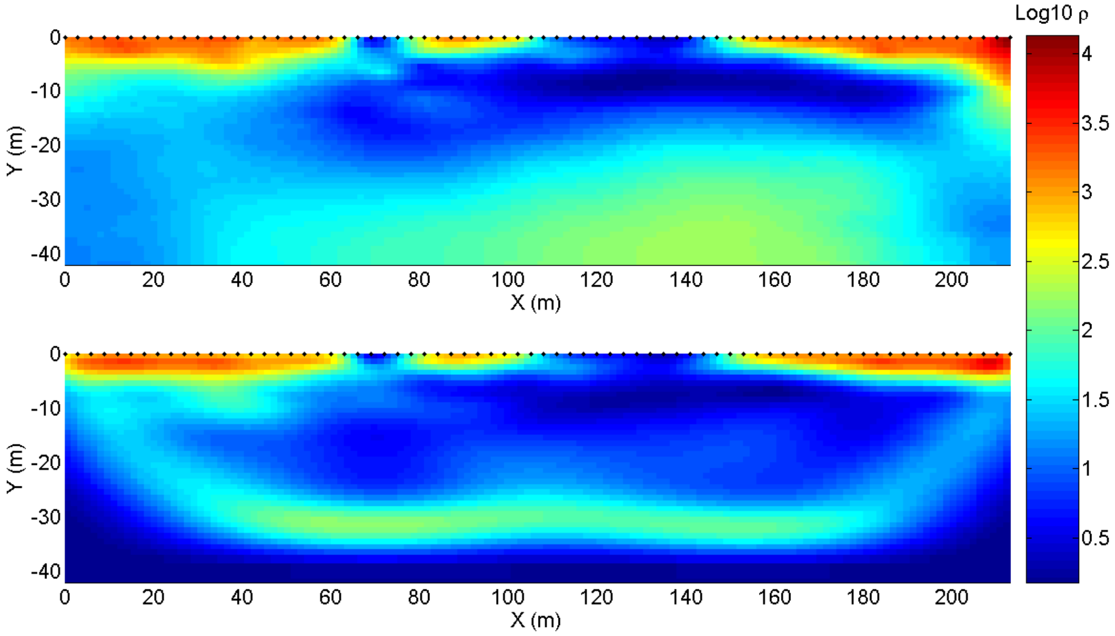

Figure 4.12: First true model (top) and inversion with a prior model equal to zero with an increased sill (bottom) (scale in $\log \rho\,[Ohm.m]$).

was also observed when a smoothness constraint solution was used as a prior. For the different cases, the true value for the initial model was about 0.3 (calculated on the logarithm of resistivity) and an inversion was carried out with the value of 1. As the observations are the same for each model, results are presented only for model 1.

Results for the first synthetic case are presented for a prior model equal to zero on figure 4.12. This inversion was chosen because it is easy to understand what happens when we compared it with figure 4.7. The model misfit is now equal to 62.05% (instead of 103.64%) and 38.87% for the first 20 meters (instead of 45.79%). Similarly, increasing the sill to 1 led to the best model misfit for the first model with the smoothness constraint as a prior. In the third case, an improvement is also observed.

Two reasons can explain this observation. First, the real parameters can take their resistivity value in a larger range than observed in borehole data. During the first inversion used to build the synthetic case, the range of resistivity value was greater than observed in boreholes. The true variance of the model could thus be higher than the estimated one. However, this explanation is not valid for the third true model. The other reason, certainly the main one, is the following.

A result like the one presented on figure 4.12 seems *a priori* a little bit surprising, especially for the third case, as false (or at least not totally true) statistics are used to build the covariance matrix. How is it possible to obtain a similar (even slightly better) solution? To answer this question, one has to investigate the role of the sill value on the inversion process with the covariance matrix as a regularization operator. Let us write the objective function of this regularization again

$$\psi(\mathbf{m}) = (\mathbf{G}(\mathbf{m}) - \mathbf{d})^T \mathbf{W_d}^T \mathbf{W_d} (\mathbf{G}(\mathbf{m}) - \mathbf{d}) + \lambda (\mathbf{m} - \mathbf{m_0})^T \mathbf{C_m}^{-1} (\mathbf{m} - \mathbf{m_0}) \tag{4.5}$$

The covariance matrix $\mathbf{C_m}$ is defined as

$$\mathbf{C_m} = \begin{pmatrix} \sigma^2_{m1} & \sigma^2_{m1,m2} & \cdots & \sigma^2_{m1,mn} \\ \sigma^2_{m2,m1} & \sigma^2_{m2} & \cdots & \sigma^2_{m2,mn} \\ \vdots & \vdots & \ddots & \vdots \\ \sigma^2_{mn,m1} & \sigma^2_{mn,m2} & \cdots & \sigma^2_{mn} \end{pmatrix} \tag{4.6}$$

where $\sigma_{mi,mj}$ are determined by the variogram model. To simplify the problem, let us first imagine that there is not any correlation between the parameters in the model. The covariance matrix becomes a diagonal matrix with the diagonal terms equal to σ^2_{mi}, all being equal to the sill value (it is the case of a perfect nugget effect). The inverse of this matrix is also diagonal with the diagonal terms equal to $\frac{1}{\sigma^2_{mi}}$. The greater the variance is (i.e. the sill value), the smaller these terms are. In the objective function, it signifies that the second term will be smaller (all the rest remaining the same) if the sill value is high or if less weight is given to the prior model. This effect can be counter-balanced by an increase in the regularization parameter.

The second important observation is that if we change the sill value, it does not have any effect on the structure of the solution. Indeed, the sill value is independent of the range in vertical and horizontal directions. So, if the sill value increases, the correlation between two points far away from each other by distance h remains the same. In practice, the sill value is only a weighting term that appears in the covariance definition (see equation of the variogram in table 2.2).

Increasing the sill enables us to obtain a model with a true relation between parameters (correlation), but with a lower importance to the prior model. So, if we have a realistic prior model but with a large error locally, we can hope that a high sill value will diminish its effect on the solution. It is exactly what is observed on figure 4.12. We see that the "banana shape" observed on figure 4.7 is reduced (or found deeper). This is explained by the reduced weight given to the prior model during the inversion process.

If we continue the analysis further, we could decrease the effect of the prior model by reducing the diagonal terms of the inverted covariance matrix gradually. In this way, the effect of the prior model would disappear for the terms corresponding to the diagonal, which gives more freedom to the inverted model. However, the prior model still plays a role for other terms responsible for the statistical structure of the solution (terms off the diagonal). Increasing the sill is a solution; another possibility is to change the diagonal terms of the inverted covariance matrix to zero. However, it seems quite dangerous to modify the diagonal terms only, because it might change the statistics for some parameters only, which could be in contradiction with the assumption of stationarity.

A test was also carried out with a sill value increased up to 10 with the smoothness constraint solution as a prior. Results are quite similar, but slightly worse than for a sill value of 1. So, giving a very high sill value does not lead to the best solution, but it can be due to the fact that the prior model is close to the true model, so a sill value that keeps the solution close to the prior model is not a bad one. We can also suppose that the sill value gives an idea of the orders of magnitude of the resistivity variations. For example, if we assume a mean value of 2 (it corresponds to a resistivity value of $100\,Ohm.m$) and a sill value $\sigma^2 = 1$, we should have (in a Gaussian distribution) 95% of the parameters in the interval $m \pm 2\sigma$, i.e. between 1 and $10000\,Ohm.m$. The inverted model has more freedom to be different from the prior model than with a sill value of 0.3. With a sill value of 10, the interval becomes very large, which is not realistic.

4.4.7 Effect of the ranges

In real cases, we have only, in the best case, vertical information given by boreholes whereas the access to horizontal information is rarely possible. So it is very important to know if the

Type of model (data sets with noise)	Sill	Horizontal range (m)	Vertical range (m)
True model	0.425	66	19.5
Smoothness constraint solution	0.33	70.5	16.5
Smoothness constraint as a prior model	0.325	70	16.5
Smoothness constraint as a prior model, increased sill to 1	0.33	66	16.5
Smoothness constraint as a prior model, increased sill to 10	0.34	67.5	16.5
Homogeneous prior model ($106\,Ohm.m$)	0.37	52.5	10.5
Homogeneous prior model equal to 0	0.63	49.5	12
Smoothness constraint as a prior model, isotropic covariance matrix	0.33	67.5	16.5
Smoothness constraint as a prior model, increased ranges and sill equal to 1	0.34	66	16.5
Homogeneous prior model ($106\,Ohm.m$), increased ranges and sill equal to 1	0.37	70.5	13.5

Table 4.1: Variogram parameters for the first synthetic case.

horizontal range of the variogram has a great influence on the results or not. In addition, it is also important to see the effect of a bad estimate of the range. One can say that it is always possible to use a first inversion (like a smoothness constraint one) to have an idea of the anisotropy by calculating variograms on inverted resistivity values (especially if this solution is used as a prior model), but the parameters of inversion (mainly horizontal and vertical smoothness parameters) will influence the results, so such horizontal range could be inappropriate.

Model 1. Several inversions were carried out to understand the effects of ranges. Firstly, it is important to note again that for the first case, all inversions were done with false ranges. However, if we have a look at the variogram parameters (table 4.1), we see that the ranges of the inverted model are not too far from the ones of the true model. It signifies that the data is strong enough to force the inversion in the right direction (higher range), but the model misfits show that the structure given by the variograms, even underestimated enables to improve the solution.

It also appears that the prior model can have an influence, as we saw that the inversions with the smoothness constraint solution as a prior model (which verify the true statistics quite well) have variogram parameters closer to the real ones than with homogeneous prior models. It explains why a homogeneous prior model leads to worse results in this first case.

If ranges multiplied by two ($60m$ and $15m$) are given for the inversion with the smoothness constraint solution as a prior model, it is quite surprising to see that the model misfit is equal to 33.62% which is the same order of magnitude than the normal case. For the first 20 layers, the misfit is even slightly worse (28.02%).

It signifies that the regularization is mostly influenced by the prior model in this case. The covariance matrix is only there to guide the inversion to a more plausible result, but the data which contains the more important information remains strong enough to impose the model in each case. It signifies that an error on the ranges is not a serious problem in this case. However, it could be very different with a noisier data set for example or a less smooth true model.

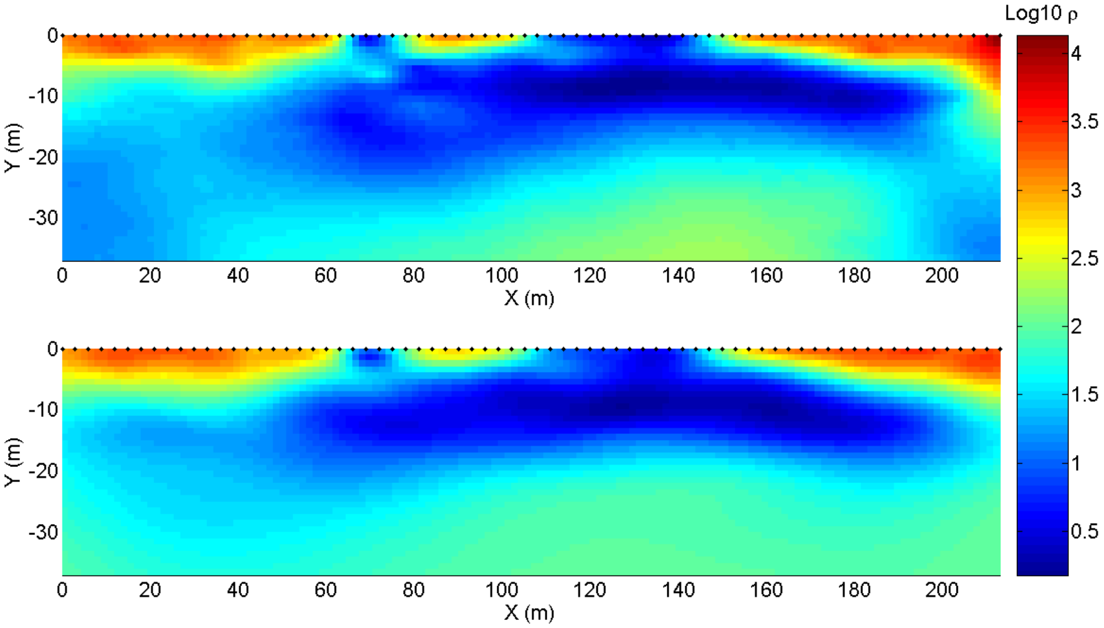

Figure 4.13: First true model (top) and inversion with a homogeneous prior model with increased ranges (bottom) (scale in $\log\rho\,[Ohm.m]$).

The results are totally different with a homogeneous prior model. Indeed, in this case, the prior model did not contain a lot of information. Giving better ranges is thus very important. We see on figure 4.13 that the result is very close to the true model. The model misfits are of the same magnitude as for the smoothness constraint solution for the first twenty layers (44.4%, 100.62% for the whole model). In this case, the covariance matrix plays a more important role than the prior model.

Model 3. However, it seems that vertical and horizontal ranges do not have the same role in the inversion. For the third synthetic case, an inversion was carried out with ranges divided by two. By doing so, the length of correlation is reduced. Obviously, worse results were expected, but we saw in the first synthetic case that it was not always true if the data and/or the prior model contains enough information to lead the inversion. This time, however, degradation in the inverted model is observed, both visually (figure 4.14 to compare with figure 4.9) and quantitatively. The model misfit is now equal to 279.5% for the whole model and 127.9% for the first 20 layers.

We directly observe a change in the right part of the section. The salt water is found, but its depth seems reduced compared to the true one and the one inverted with good ranges (around $20m$ instead of $30m$ with the real ranges). This phenomenon can be easily understood. Indeed, we know that when the data is not sensitive to a change in some parameters, it is the minimization of the second term of the objective function that determines this parameter. This term is influenced by the inverse covariance matrix and by the prior model. We have already had an idea of the role of the prior model by increasing the sill. Here, we see that the real range enables us to retrieve the true model better, because it describes a correlation on a bigger thickness. Knowing the vertical range if we want to improve the solution seems thus very important. However, horizontally, few differences are detected, we can thus hope that the horizontal range (difficult to determine) is of less importance.

We can also see in the left part of the sections that the correlation length is longer in figure 4.9, because the "banana shape" begins to appear in figure 4.14. Having a good estimate of the vertical range is thus very important to improve the solution where sensitivity is low.

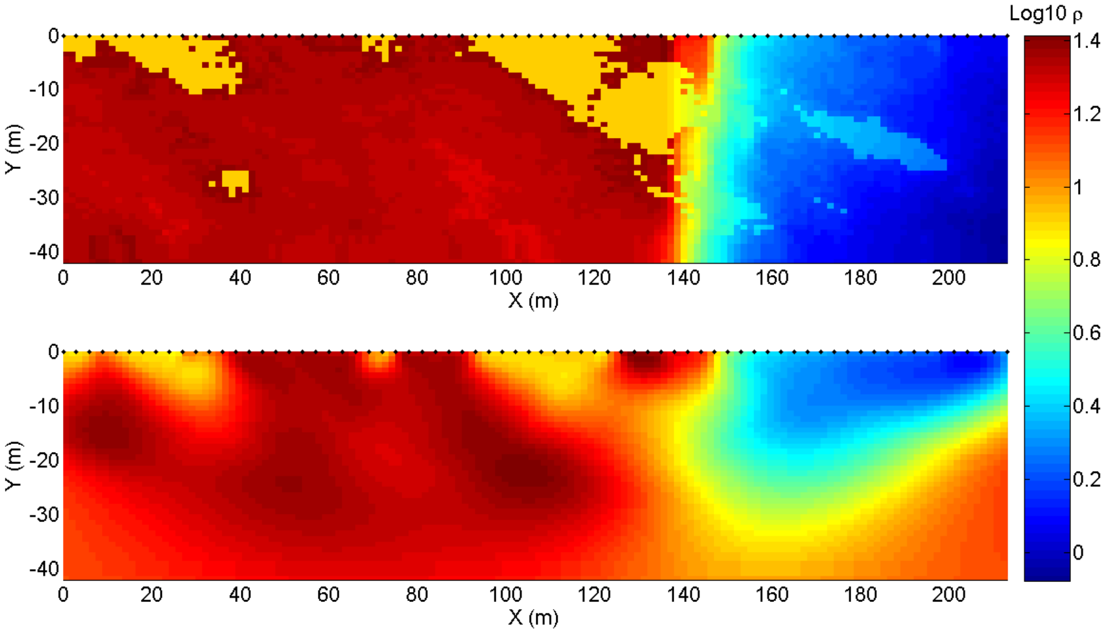

Figure 4.14: Third true model (top) and inversion with a homogeneous prior model with ranges divided by two (bottom) (scale in $\log \rho \, [Ohm.m]$).

Model 1. To analyze the role of the horizontal range without an effect of the vertical range, the data was inverted with an isotropic covariance matrix. This is an extreme case, because we know that a horizontal anisotropy exists, just by analyzing geological data. However, it will enable us to assess the influence of the horizontal range and see if the inversion is sufficiently guided by the data to find the anisotropy.

For the first case, it was first done with the smoothness constraint solution as a prior model. It led to very surprising results, the model misfits being almost equal to the ones of the smoothness constraint solution. The fact that the smoothness constraint inversion gives a good result in this synthetic case can influence the results as it is used as a prior model. Indeed, the regularization parameter λ is higher for this inversion than for the other one. More weight is given to the regularization term, which is equal to zero if the solution is equal to the prior model. It signifies in this case that it was a waste of time to carry out an inversion with an isotropic covariance matrix because the covariance matrix did not bring enough information compared to the prior model.

To see if an isotropic covariance matrix failed to improve the results in many cases, the same inversion was done with a homogeneous prior model. In this case, the results (figure 4.15) with an isotropic covariance matrix are not too far from the results with an anisotropic one (figure 4.8). The model misfit is equal to 193.57% (157.63% for the 20 first meters). It is quite logical that the model misfit is slightly worse, because the anisotropic covariance matrix contains an estimate of the statistics of the true model whereas the isotropic one does not have information on the horizontal range. We just see that structures are slightly less smooth horizontally. However, the difference is not so big and when there is absolutely no information on the anisotropy available, an isotropic matrix can be a first estimate.

We can explain that quite easily: the need of additional information to improve the inversion process is mainly crucial in depth. It signifies that the vertical range, available if boreholes are present, is much more important than the horizontal one. For example, if we detect salt water at $-5m$ depth at abscissa $100m$, it signifies that this is contained in the data. It also signifies that if the intrusion is present at abscissa $120m$, this information should also be among the

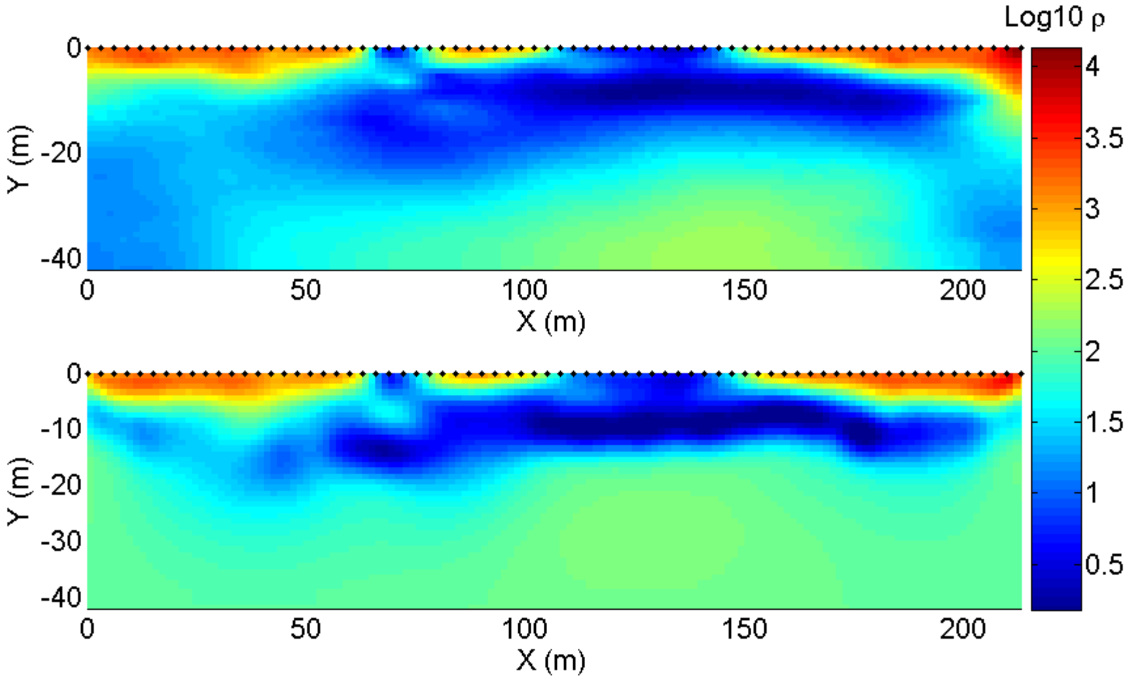

Figure 4.15: First true model (top) and inversion with a homogeneous prior model with equal ranges (bottom) (scale in $\log \rho\,[Ohm.m]$).

data, as the depth level is the same (at the same depth level, sensitivity is often quite constant, see chapter 8). The horizontal range should not be necessary to find a continuous intrusion, the data is sufficient. Obviously, as demonstrated by this example, the right horizontal range will improve the solution slightly. This feature is also shown in table 4.1. Indeed, we see that horizontal ranges, even when there are underestimated by the variogram parameters used during inversion, are quite well retrieved in the inverted model. In this case, an overestimation of the parameter would be worse than an underestimation.

4.5 Conclusion

These synthetic case studies allow to understand better the regularization process using the covariance matrix and to find the best parameters to use during an inversion.

First, the prior model has a great importance during the inversion. For model 1, a smoothness constraint inversion solution seemed to be the best alternative, because the true model was very smooth itself. However, it appears that it was not always the case. For model 2, using this type of prior model would have been without interest, because the smoothness constraint solution was too bad. A Gaussian simulation enabled to better retrieve the true model. For model 3, it yielded very large regularization parameters. In consequence, the solution was very close to the prior model. It also appeared that when a smoothness constraint solution was used as a prior model, this model sometimes played a greater role during the inversion than the covariance matrix. In such a case, a homogeneous prior model (equal to zero or to a mean value) can give good results. As a homogeneous prior model has a statistical meaning, this type of prior model should be preferred. In addition, the results in the first case were not too bad with such a prior model (if good parameters were used). It signifies that it may be preferable to use a model with little prior information than a strong model that will be reflected in the solution. It was for example the case with the prior model with two zones. A Gaussian simulation as a prior model seems to be a possible alternative, with the disadvantage to be only one realization and not the most probable solution (or the need to carry out several simulations), but being able to include borehole data (conditioned simulation).

According to these results, it was decided to try these three prior models for the real case study in the Westhoek area (smoothness constraint solution, homogeneous prior model, Gaussian simulation conditioned with borehole data). It will not be possible to calculate a model misfit, but we saw that it was not always the best estimate. In addition, borehole data are available to check the accuracy of the inversion.

Then, it appeared that the sill value plays also a great role, not on the statistical point of view, but on the weight given to the prior model. In every case, it seemed better to use a higher sill value to give more freedom to the inverted model. According to these observations, it was decided to use a value of 1 for the real data set (it seemed that this value was close to the true variance on the site).

Finally, the importance of the ranges is not so clear after our synthetic benchmarking. For model 1, underestimated ranges led to good solutions because the data contained enough information. In addition, when the smoothness constraint solution was used as a prior model, the prior model influenced the inversion a lot. However, for model 3, we see that true ranges enabled to improve the solution in the zone of low sensitivity, which is one of the aims of this type of regularization (where the data brings a lot of information, it is not necessary to regularize hugely). Thus, it seems that it is very important to have a good estimate of the vertical range. Indeed, it enables to improve the solution, especially in depth. It was clearly the case when a homogeneous prior model was used for model 1. Having a good estimate of the horizontal range is also very useful to carry out a good inversion, but in most cases, an underestimation of this parameter is not a big problem. Indeed, near the surface, data contains enough information to produce continuous structure. The estimate of the horizontal range could be a bigger problem when vertical structures are expected (to find them in depth).

In most cases, the regularization parameter remained limited (the bigger this parameter, the bigger the weight on the regularization term), and the solution did not verify the imposed variogram completely. Sometimes, its value was abnormally high and the solution was equal to the prior model. It could be useful to control this parameter more accurately to avoid such a case or to allow to verify the statistical constraint exactly.

Inversion	Noise	Model misfit (%)		Model misfit 20 first layers (%)		λ
		ρ	$\log\rho$	ρ	$\log\rho$	
Smoothness constraint	N	25.74	10.23	22.54	10.8	43.57
	Y	40.03	18.52	38.59	20.93	14.97
Smoothness constraint as a prior model	N	31.83	12.56	22.84	11.62	0.43
	Y	38.96	15.26	27.25	13.59	315.8
Homogeneous prior model	N	170.11	20.67	72.46	16.32	8.56
	Y	181.88	30.95	155.22	30.33	10.42
Borehole based prior model	N	56.38	18.23	57.57	20.64	14.13
	Y	85.35	27.82	84.79	33.71	7.485
Prior model equal to 0	N	233.32	54.62	63.88	31.42	4.24
	Y	103.64	44.38	45.79	26.27	3.57
Smoothness constraint as a prior model, isotropic covariance matrix	N	25.75	10.21	22.48	10.74	4960
	Y	39.88	18.43	38.33	20.8	1952
Homogeneous prior model, isotropic covariance	Y	193.57	33.96	157.63	34.45	4.29
Smoothness constraint as a prior model, increased sill to 1	N	28.83	10.22	20.17	8.67	158
	Y	34.41	13.75	26.85	13.44	549.5
Smoothness constraint as a prior model, increased sill to 10	Y	35.23	15.27	32	16.34	633.4
Prior model equal to 0, increased sill to 1	Y	62.05	30.31	38.87	20.82	18.1
Smoothness constraint as a prior model, increased ranges to 15 and 60 and increased sill to 1	Y	33.62	13.66	28.02	14.45	524.1
Smoothness constraint as a prior model, increased ranges to 15 and 60	Y	35.74	13.68	27.82	13.63	235.6
Homogeneous prior, increased ranges to 15 and 60	Y	100.62	21.37	44.4	19.93	24.36

Table 4.2: Model misfits and regularization parameter for the first synthetic case.

Inversion	Model misfit (%)		Model misfit 20 first layers (%)		λ	Vertical range (m)	Horizontal range (m)
	ρ	$\log\rho$	ρ	$\log\rho$			
Smoothness constraint	323.4	1988.1	230.06	2128.9	6.15	24	94.5
Prior model equal to 0	177.96	1496	144.86	1507.6	1.93	19.5	79.5
True model as a prior model	110.01	580.95	30.03	172.16	28670	10.5	39
Other Gaussian simulation as a prior model	1237.5	2126	511.91	1516.9	1.67	12	33

Table 4.3: Model misfits, regularization parameter and variogram ranges for the second synthetic case.

Inversion	Model misfit (%)	Model misfit 20 first layers(%)	λ
Smoothness constraint	64.3	30.15	11.9
Prior model equal to 0	27.3	23.05	21.26
Smoothness constraint inversion as a prior model	63.75	30.26	11970
Homogeneous prior model ($\rho = 12.7\,Ohm.m$)	171.62	48.04	41.37
Homogeneous prior model ($\rho = 12.7\,Ohm.m$) and half ranges	279.50	127.9	75.7
Prior model equal to 0 and sill equal to 0.3	32.25	25.63	6.14
Homogeneous prior model with two values	44.37	28.27	18.94

Table 4.4: Model misfits and regularization parameter for the third synthetic case.

Chapter 5

Geology of the Belgian coast

5.1 Geology of Paleozoic and Mesozoic

The Paleozoic basement of the studied area belongs to the massif of Brabant (Jacobs *et al.*, 2002). It is formed by sedimentary rocks from the lower Cambrian to the upper Silurian. During the Caledonian orogeny, the massif of Brabant was folded. Outcrops can only be found in valleys cutting the overlying rocks (the Dender, the Senne, the Dyle, the Thyle, the Orne, the Orneau, the Gette, the Mehaigne) (Boulvain, 2010). In the coastal area, this basement is situated at great depth. In the studied zone, it appears around $-250mTAW^1$ (Legrand, 1968).

During the lower and middle Mesozoic, no deposits took place in the present western coastal area. During the Cretaceous, the area was again evaded by the sea. The studied area belonged to the carbonate buildup during the upper Cretaceous. It led to chalk deposits (Jacobs *et al.*, 2002 ; Boulvain, 2010). They are in discordance with the Paleozoic basement. The basis of the Mesozoic deposits lies at a depth between $-200mTAW$ to the south and $-430mTAW$ to the north (important north dip). The thickness of these layers ranges from 30 to $120m$. It is about $80m$ near the French-Belgian border (Jacobs *et al.*, 2002).

5.2 Geology of the Tertiary

During the Cenozoic, several periods of transgression and regression followed one another (Boulvain, 2010). A great part of Flanders is covered by tertiary sediments. The basis of the Tertiary deposits lies at a depth of $-170mTAW$ in the area of De Panne. The first deposits of the Paleocene belong to the group of Landen. Continental sediments of the formation of Tienen (member of Knokke) covered marine sands (member of Grandlise of formation of Hannut) (Jacobs *et al.*, 2002). The formation of Tienen constitutes the base of the Ypresian. It corresponds to a sharp variation in the ^{13}C content of the sediments linked with the "Thermal maximum at the base of the Eocene" (Boulvain, 2010).

At the beginning of the Eocene, the sea invaded the submerged area. In the same time, the massif of Brabant is in subsidence (Boulvain, 2010). The Eocene deposits are constituted, from the base to the top, by the group of Ieper, the group of Zenne and the formation of Maldegem. The succession is presented in table 5.1. In the studied area, only the group of Ieper, and particularly the formation of Kortrijk, is found. This clay formation (marine deposit) is subdivided into several members and has a thickness of more than $100m$ (Jacobs *et al.*, 2002). At the base is the member of Mont-Héribu (not found in the study area). It is characteristic of the transgression with silty clay with silt and sand intercalations (Boulvain, 2010). Then, the member of Saint-Maur is composed of homogeneous fine-silty grey clay, $20m$ thick. The

---

[1] The elevation is given in $mTAW$, the Belgian reference system, $2.3m$ below the mean sea level. In the next section, elevation will always be given in $mTAW$, even if TAW will be sometimes omitted.

Chronostratigraphy	**Group**	**Formation**	**Lithology**
Upper-Middle Eocene		Maldegem	Alternation of sand and clay
Middle Eocene	Zenne	Aalter	Sand Sandy clay
Lower Eocene	Ieper	Ghent	Sand Clay
		Tielt	Sand and silt
		Kortrijk	Clay
		Tienen	Sandy and clayey continental sediments
Upper Paleocene	Landen	Hannut	Marine sand

Table 5.1: Lithostratigraphy of the Tertiary (modified after Jacobs *et al.* (2002)).

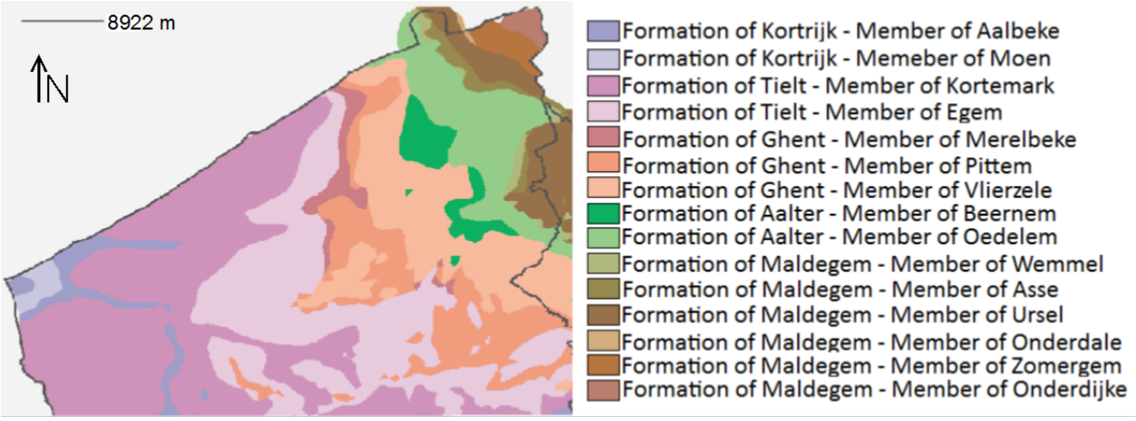

Figure 5.1: Geological map of the coastal area (modified after Jacobs *et al.*, 1998 ; DOV, 2010).

member of Moen covers the member of Saint-Maur with grey clay to clayey silt. At the top of the formation, the member of Aalbeke is found. It is a dark grey and stiff clay, $10m$ thick. Deposits of the Oligocene and the Neogene are not present in the western part of the coastal area. Sediments of these periods are found elsewhere in the country (North-East and central part) (Jacobs *et al.*, 2002).

Figure 5.1 shows the geological map of Flanders in the coastal area. The study site is located at the French-Belgian corner, along the coast (western part of the figure). We see that the formation of Kortrijk appears in the western part of the coast. Then, the formation of Tielt and Ghent are found. On the Eastern part, the formations of Aalter and Maldegem cover the previous ones. All the formations are subhorizontal with a dip angle oriented towards the northeast (Jacobs *et al.*, 1998).

5.3 Geology and hydrogeology of the Quaternary

Quaternary evolution enables to explain the nature of the sedimentary deposits in the coastal plain. Recent Quaternary evolution and human interventions (land reclamation) explains the current complex fresh-salt water distribution. The thickness of the quaternary deposits varies, in the coastal area, between 25 and $40m$ (Jacobs *et al.*, 2002 ; Jacobs *et al.*, 1998).

The map presented on figure 5.2 shows the different units of quaternary deposits in the Belgian coast with an explanation of the different profiles.

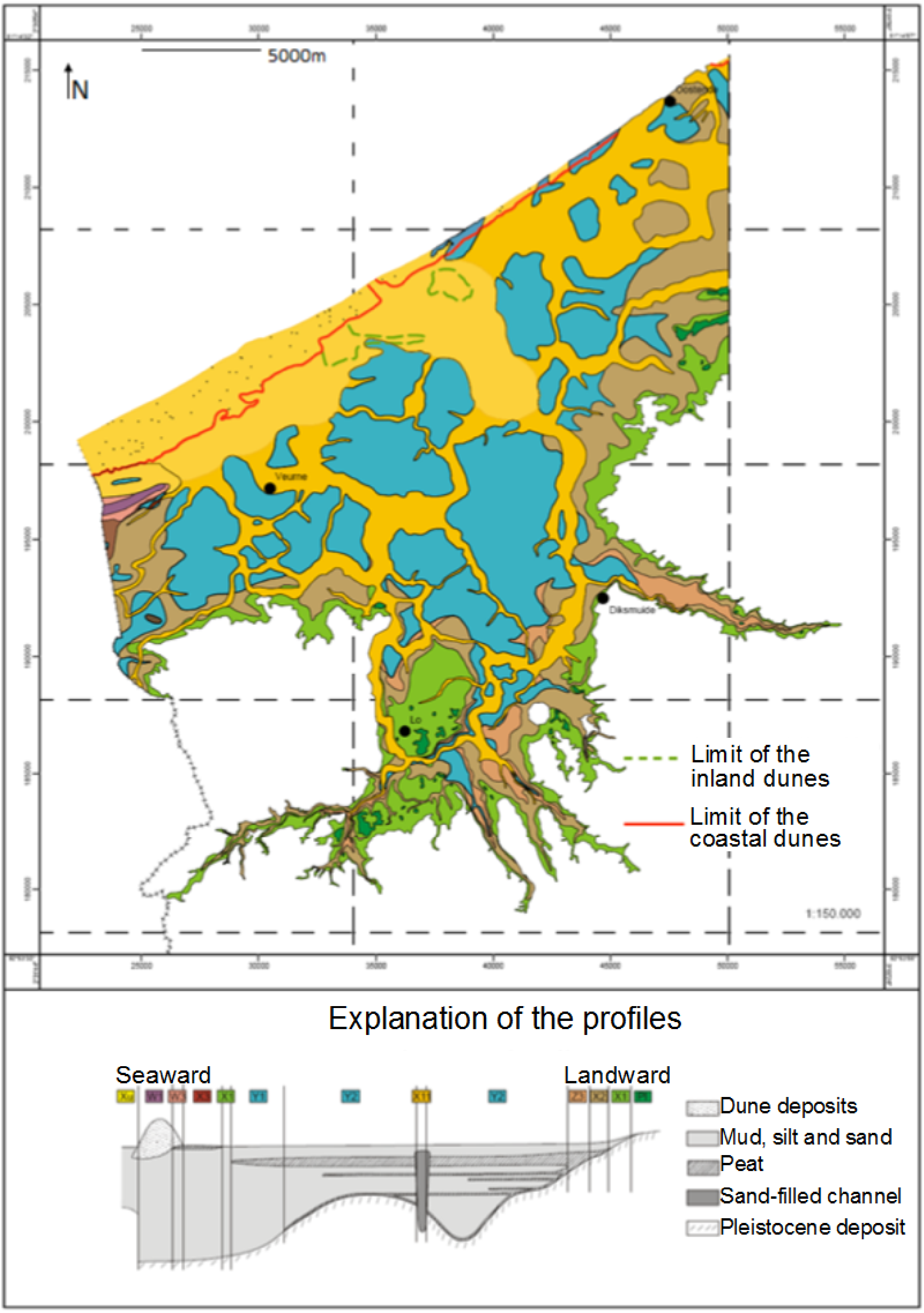

Figure 5.2: Map of the Quaternary deposits of the Belgian coast (modified after Baeteman, 2005).

5.3.1 Pleistocene

During the Upper Pleistocene (Eemian/Wechselian), the sea level was very low, due to the last glaciation. The deposits of the recent Pleistocene (Wechselian) in Belgium correspond to this period. It signifies that the sea level was very low. They mainly consist of aeolian deposits. It is why the coarse particles (sand) were deposited in Low-Belgium, loess particles until Middle- or even, for the finest ones, High-Belgium. Along the south part of the western coastal area, there are no Wechselian deposits. It could be due to intensive erosion, when a great amount of Pleistocene deposits were reworked (Lebbe, 1978). Indeed,during the Holocene, 10000 years ago, the sea level increased by more than $100m$. The sea entered the Belgian coastal plain of the Pleistocene again.

In the area of De Panne, Eemian deposits of a thickness of about $1m$ are found. They are marine, estuary and fluviatile sands (Lebbe, 1978). At some places along the coastal plain wadden deposits can also be found under the Wechselian deposits (Maréchal, 1992).

5.3.2 Holocene

Previously, it was assumed that the Holocene deposits in the coastal plain were the results of two transgressions: the Calais and the Dunkirk transgressions. This description was mainly based on shallow boreholes ($1.25m$) realized within the framework of the soil mapping survey (Baeteman, 1999).

Sand with clay lenses at the top and old dunes were supposed to be deposited during the Calais transgression. Then, a one to two meters thick peat layer is present. It might have resulted from deposition behind the dune belt during a decrease in the sea level or a stable period of sea level. After that, the Dunkirk transgression would have had three phases beginning around the 2^{nd}, 4^{th} and 10^{th} centuries AD, leading to clay and sand deposits (Maréchal, 1992). However, these considerations do not seem to take into account all the sedimentary characteristics of the deposit and radiocarbon dating data published after 1980 (Baeteman, 1999).

This theory evolved in the last decades and new explanations permit to better described the sedimentary deposits in the Belgian coastal area.

As presented above, the subsoil of the Holocene consists of deposits of Pleistocene sediments (mainly of Weichselian age) or in Eocene deposits when the Pleistocene is eroded. It presents a depression nearly perpendicular to the coastal line, certainly formed by a river during Weichselian age. This palaeovalley does not result from erosion during the Holocene (Baeteman, 1985 ; Baeteman, 1999).

A lateral evolution characterizes the deposits in the coastal plain of Belgium. Towards the sea, marginal-marine and brackish clastic sediments are found. In some places, a basal peat layer underlies them. Further from the sea, in the transition zone, clastic sediments alternate with peat layers. Towards the hinterland, a basal peat layer is covered by clastic brackish sediments (Baeteman, 1991). This sequence is illustrated on figure 5.3. The sedimentary succession can be explained by the sea-level history during the Holocene, presented on figure 5.4, according to Baeteman (1999). The evolution of the position of the coastal environment is showed on figure 5.5.

The basal peat layer developed from about 10000 BP[2] seaward to 8100 BP landward. The sea invaded the area through the palaeovalley (see figure 5.5) (Baeteman, 1999). It indicates a shift of the coastal environment due to a rapid rising sea level (Baeteman, 1991), so the central part of the area was a tidal flat whereas in the landward part there were channels. This rising sea-level rate reached an average of 7m per thousand years (Baeteman, 1999). The presence of

---

[2] BP : Before Present, the reference year is 1950. 50 BP corresponds to 1900.

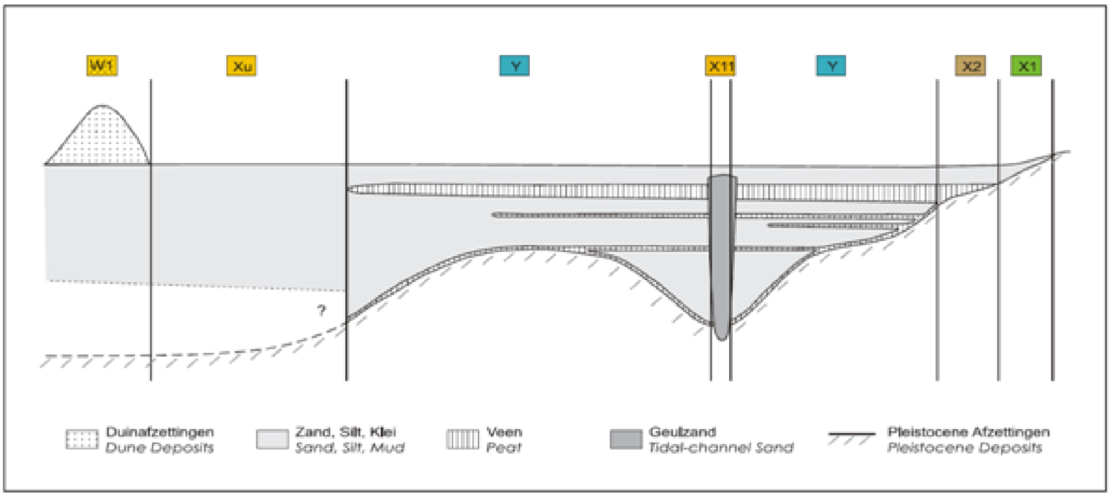

Figure 5.3: Schematic cross-section in the Holocene sediments (Baeteman, 2005).

the peat layer gives evidence that the depression in the Pleistocene had existed before the sea level rise (Baeteman, 1985). The basal peat layer is absent (figure 5.3) in some zones, where the Pleistocene deposits have a too high elevation or where the peat layer or even the Pleistocene have been eroded (along the sea). After 8100 BP until 7000 BP, tidal flats started to develop (Baeteman, 1991).

Around 7500-7000 BP, the rise sea level curve (figure 5.4) shows a slower average rate of 2.5m per thousand years, the shift of the tidal environments was less important and the sedimentation was such that the basin was filled up (Baeteman, 1999). The conditions were such that peat growth initiated again, this phenomenon was generalized around 6400 BP when peat is observed over nearly the entire plain in alternation with tidal flat sediments (figure 5.5). However, this alternation is not homogenous on the entire plain. Indeed, intertidal flats, supratidal flats and peat growth environments existed simultaneously next to each other. This explains the intercalated peat layers described above in the transition zone (Baeteman, 1991 ; Baeteman, 1985 ; Baeteman, 1999). In consequence, according to Baeteman (1999), this alternation does not reflect sea-level fluctuation and the intercalated peat layers cannot be regarded as a single peat bed stratigraphic unit as proposed by previous authors (for example Maréchal, 1992).

After 5500-5000 BP, the average rate reduced again to a level of 0.7m per thousand years. Apparently, sediments supply was still available and overran the sea-level rise. Thus, the shoreline prograded seaward. During this period, the thickest intercalated peat layer developed. The peat accumulation stopped globally around 3000 BP but continued until about 1500 BP in some places in the landward part of the plain (Baeteman, 1991 ; Baeteman, 1999). Around 4700 BP, a first dune belt began to develop: the old dunes of Adinkerke-Ghyvelde. The dunes reduced the influence of the sea on the plain. After that, tidal flat deposits formed the next fill of the plain, which is one or two meters thick (Baeteman, 1999).

After this period, a new landward migration in successive steps of the tidal systems began. There is no evidence to explain this new movement of the coastal line. The most likely hypothesis is the lack of sediments to compensate for the rate of sea level rise. Erosion certainly took part in the supply of sediments during this period (Baeteman, 1999).

After that, the final fill of the western coastal plain was a mudflat deposit. The area changed into a salt marsh. The current dune belt also started to develop from about the seventh century AD. From about 900 AD, man reclaimed the area (Baeteman, 1999). The flooding, called phase

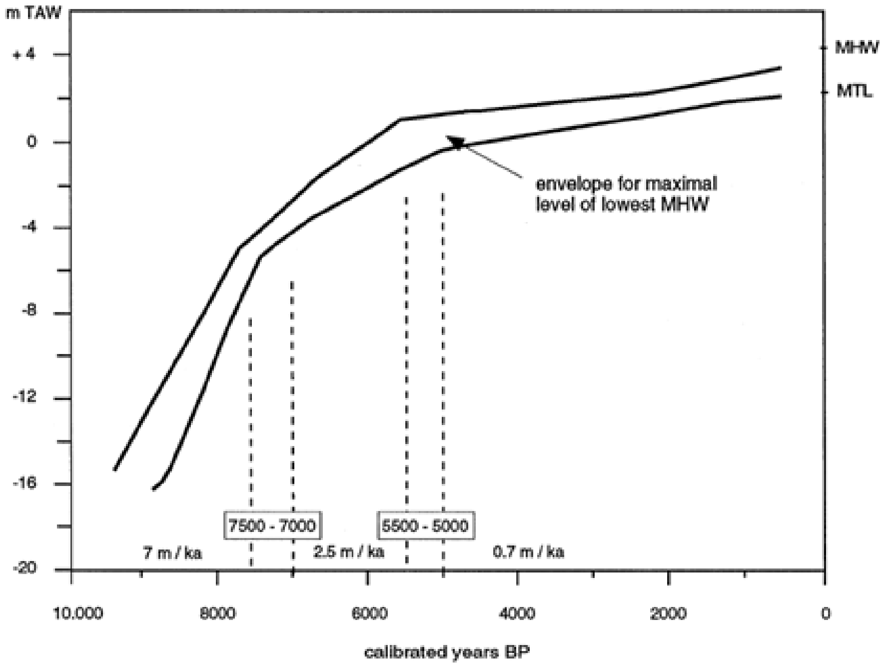

Figure 5.4: Relative sea level curve during the Holocene in the western Belgian coast plain (Baeteman, 1999 after Denys & Baeteman, 1995).

III of the Dunkirk transgression[3], occurring around 1000 AD, started from two breaking zones: the Zwin and the IJzer's mouth (Maréchal, 1992). As they occurred after land reclamation, these floods could have been induced by man (Baeteman, 1999).

5.3.3 Hydrogeological evolution

During the first part of the Holocene, the ground-water reservoir was almost completely filled with salt water, but locally, a fresh water lens could have developed under the peat (Vandenbohede & Lebbe, 2002).

As seen in the previous section, during the Quaternary, there was an evolution in the sea level. A first coastal barrier started to develop around 4700 BP: the Old dunes belt (Van Meir & Lebbe, 1998 ; Maréchal, 1992). This barrier was attacked for the next centuries. Even if the dates are not well known, it seems that around 2700-2800 BP, a dune belt was lying at both sides of the current French-Belgian border. It is possible to find relics of the Old dunes belt under the young dunes to the west of De Panne (Van Meir & Lebbe, 1998).

If we assume, like Van Meir & Lebbe (1998), that, at that moment, the coastal aquifer was completely filled with salt water and that a recharge[4] of fresh water was taking place, consequently, the dune belt aquifer was progressively filled with fresh water. This fresh water pushed the salt water downwards and sidewards. This freshening of the aquifer was almost completely achieved after 1000 years. However, salt water could be found on both sides of the dune belt, under the shore due to the semi-diurnal tides and underneath the tidal flat on the other side.

In the next centuries, the area was submerged during different periods. It has already been explained that some authors thought that it was due to the different phases of the Dunkirk flooding, but the new theory favor a progressive sea level rise with a decreasing rate. It was

---

[3] The name of Dunkirk transgression is still widely used, even if the new theory is now more widely accepted.

[4] Van Meir & Lebbe (1998) assumed an annual recharge rate of 280mm.

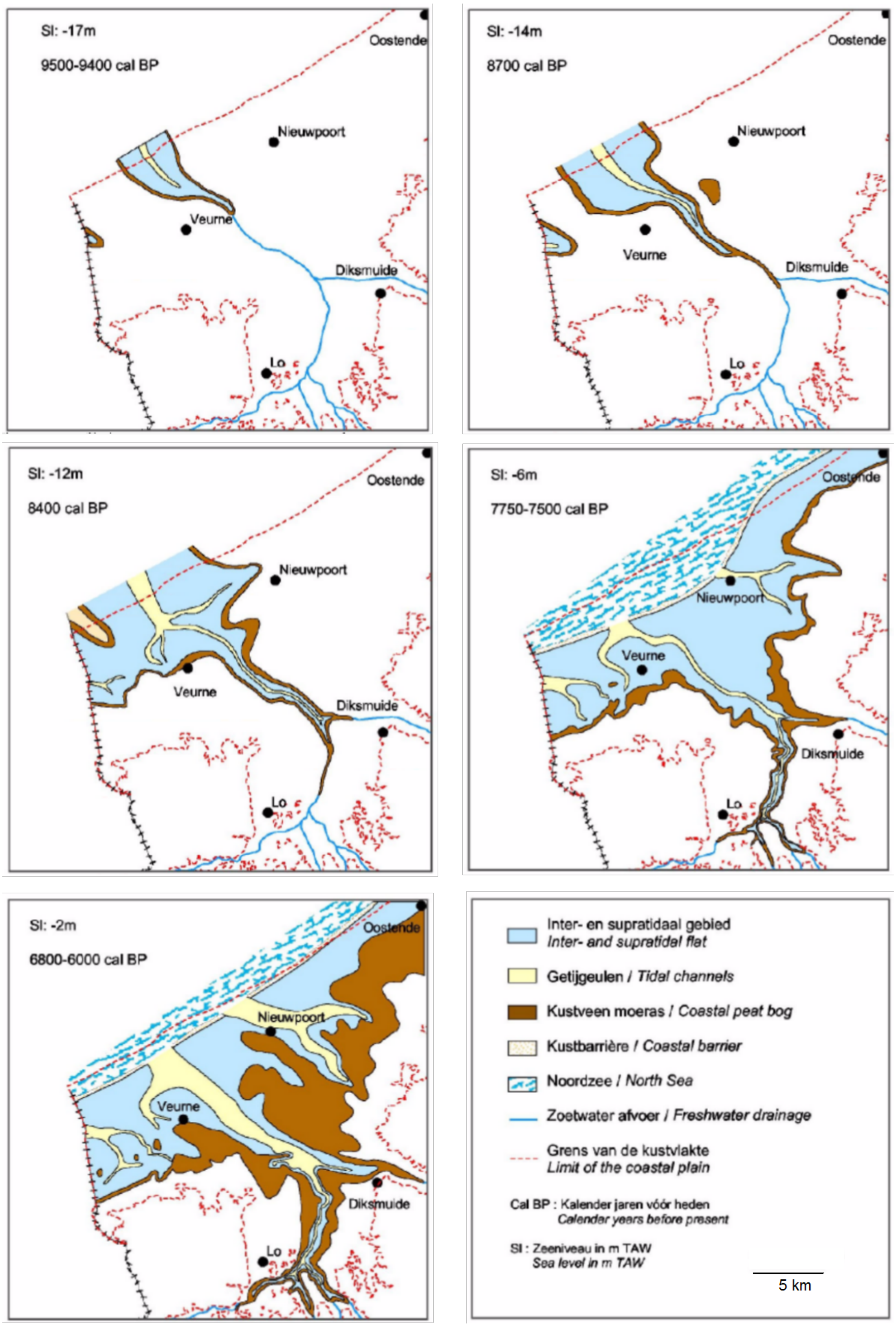

Figure 5.5: Palaeogeographical maps of the landward extension of tidal flat environment (Baeteman, 2005).

also during these periods that the current dune belt developed (Vandenbohede *et al.*, 2008a; Maréchal, 1992; Baeteman, 1999).

From the hydrogeological point of view, it seems that a dynamic equilibrium between fresh and salt water existed in the area. Thus, the situation remained stable until around 700 AD (Van Meir & Lebbe, 1998). After that, the present dune area developed and extended leading to an evolution in the hydrogeological situation. Because of the recharge of fresh water, salt water was pushed deeper into the tidal flat in the upper part of the aquifer. However, in the lower part, salt water situated landward flowed towards the sea. So, even with a freshening, salt water occurred again in the lower part of the dune aquifer. This phenomenon was due to the position of the water divide moving landward due to the extension of the dune area. During the following decades, the recharge of freshwater tended to dilute the salt water. Around 1200 AD, the dune aquifer was filled again with fresh water. Salt water lenses could have appeared in some low permeable layers (Van Meir & Lebbe, 1998).

In contrast, in the polder area, where the mean elevation is situated below the high water mark, drainage systems are necessary to evacuate the water; this action limits the recharge rate. It signifies that only the upper part of the aquifer is filled with fresh water, whereas salt water is found deeper (Vandenbohede *et al.*, 2008a).

Chapter 6

Presentation of the study site - the Flemish Nature Reserve Westhoek

6.1 Situation and general presentation

The site of the Flemish nature reserve Westhoek is situated in De Panne, along the French-Belgian border along the coast. The zone investigated in this master thesis is located more accurately among the dune area, where two artificial sea inlets were achieved crossing the fore dunes. Figure 6.1 offers a general overview of the Westhoek.

Figure 6.1: Site location, the two artificial sea inlets are indicated with black arrows (modified after Vandenbohede *et al.*, 2008a).

The two artificial sea inlets were built to promote biodiversity and, in particular, to develop naturals habitats (Vandenbohede *et al.*, 2008a ; Verwaest *et al.*, 2005). Such sea inlets remain a rare phenomenon along the southern North Sea, but they display specialized bird species and also a particular salt tolerant flora (Vandenbohede *et al.*, 2008a).

Initially, the inlets made in the dune belt in January 2004 were designed in such a way that seawater could only enter inside the dune area, among the two infiltration ponds, during the period of high tide (initial level of the breach was $5.5mTAW$ while the high sea level varies between 3.5 and $5.6mTAW$) (Vandenbohede *et al.*, 2008a). However, at the moment, the two sea inlets are silting up with sand. The biggest one (the western one) is completely filled whereas the second one is almost closed, but sea water could maybe enter the pond during very high tides or storm events. It signifies that the dynamics of sea water arrivals stopped (at least for the western pond). Nevertheless, salt water has already infiltrated and continues to evolve in the dune aquifer.

As it was presented in chapter 5, salt water fills the sediments under the sea but also deeper under the polders. So, this water cannot be used for human consumption. The fresh water aquifer situated within the dune area is thus particularly important. On figure 6.1, we note the presence of water catchment facilities, situated approximately $1.4km$ away from the two sea inlets. In order to evaluate the risk of contamination, a study was carried out to evaluate and monitor the evolution of the sea salt water which was going to infiltrate in the dune area (Vandenbohede *et al.*, 2008a).

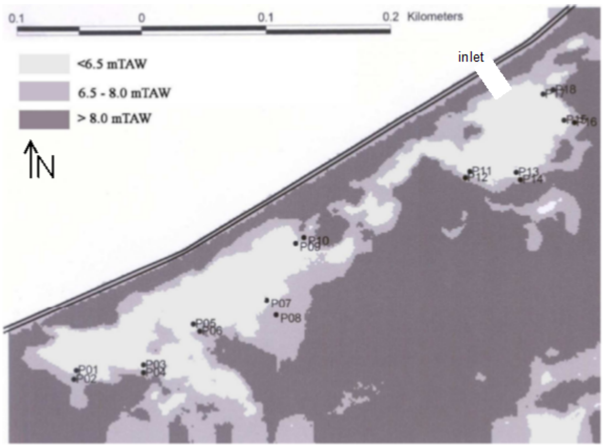

Figure 6.2: Location of boreholes and topography of the investigated zone (Vandenbohede *et al.*, 2008a).

The geophysical studies carried out within the context of this master thesis are in line with the continuity of measurements already done to monitor the two artificial sea inlets area in the Westhoek nature reserve. Figure 6.2 presents the location and configuration of 18 observation boreholes drilled around the infiltration ponds. Three other boreholes were drilled further from the sea, but they are not visible on figure 6.2.

6.2 Geology and hydrogeology of the site

According to Baeteman (1985, 2005), the site of the Westhoek has a general lithologic profile with only clastic sediments, no peat layer is occurring in the dune area, it appears further landward (see figure 5.3). As explained before, this absence could be due to erosion during the last part of the Holocene.

Lithology of the dune area is well developed in the PhD thesis of Lebbe (1978) and the master thesis of Luyten (2003). My aim in this context was not to develop the lithology in all the dune area as the investigation zone was limited at the sea board of the dunes. After a general overview, more details will be given about infiltration ponds. They are well known thanks to borehole descriptions.

At the basis of the quaternary deposits, we find the formation of Kortrijk (Eocene), which is about $100m$ thick. The depth of investigation of ERT will not be sufficient to see the Paleozoic and Mesozoic rocks. From a hydrogeological point of view, this formation can be considered as impermeable (in the models) (Vandenbohede *et al.*, 2008a).

As can be seen on the geological map of the Quaternary (figure 5.1), quaternary deposits of the Westhoek nature reserve are constituted of recent dunes. They are about $30m$ thick

(Vandenbohede *et al.*, 2008a ; Jacobs *et al.*, 1998 ; Baeteman, 1985). As the topography of the dunes can be important, it is impossible to give a more precise value. The lower part of the deposits is formed by medium to coarse medium sands with shells and shell debris of Eemian age. The upper part of the deposits is constituted of fine to fine-medium sands of the Holocene (Lebbe, 1999; Van Meir & Lebbe, 1998; Lebbe, 1978). Two semi-permeable layers (figure 6.3) with clay content are also found among the dune deposits, the first one in the area of the infiltration ponds, the second one near the water catchment (Vandenbohede *et al.*, 2008a).

Luyten (2003) divided the whole dune area in three different parts for her hydrogeological model: the upper part from the water level to $+0.5mTAW$, the middle part from $+0.5$ to $-17mTAW$ and the bottom part down to the top of the Tertiary. This work and the lithological study of Lebbe (1978) permit a better description of the deposits than above. The upper part consists in aeolian pale yellow medium sands from the young dunes; some layers with peat content are possible, but not well developed. This sand is less humic than the one of the old dunes located below. This is a yellow-grey to brown-grey medium to fine sand. Under this layer, grey to grey-blue medium to fine sand with organic rests and shell debris is found.

The middle part of the quaternary deposits is constituted by medium to fine grey to dark grey sands. Between about -7 and $-12mTAW$, a layer with more fine materials (clay content) is found. Hereafter, this layer will be sometimes mentioned as clay layer, clayey layer or semi-permeable layer. In the bottom part of the study area, the deposits are medium to coarse marine sands with a large content of shell, shell debris and flint pebbles that constitute the coarse part of the layers (Luyten, 2003 ; Lebbe, 1978).

We can compare these lithological descriptions with the borehole logs around the inlets (Laboratoria Van Vooren, 2005). During the field campaign, only the smallest pond was investigated (see chapter 7); it is why the results are presented for boreholes P11 to P18. The upper part of the deposits is everywhere composed of fine sands with a lot of shell debris, but this content decreases in depth. For the geophysical campaign, the more interesting parameters are the position and the thickness of the layer with clay content. Table 6.1 summarizes these parameters for each borehole. This layer seems to be less deep than expected. In addition, its thickness is quite large. However, there may be some errors on the depth due to the drilling method. Indeed they used a bentonite mud to make the holes. In addition, the cuttings took some time to rise up to the surface. Accuracy is thus limited.

Under this layer, fine to medium sands with shell debris are found. Sometimes, low clay content is possible in the upper part. The clay of the formation of Kortrijk lies at a depth between -25.5 and $-26.8mTAW$ (Laboratoria Van Vooren, 2005)).

The hydrogeological situation resulting from the historical development during the Holocene is illustrated in figure 6.3. The dunes have a higher elevation than the sea and the polders and water is artificially drained from the polders. The groundwater level is thus higher in the dunes. As a consequence, part of the freshwater of the dunes flows towards the polders, whereas the other one flows towards the sea.

On figure 6.3, we note also a seawater lens that occurs under the shore. This lens is due to the recharge of salt water during high tide, especially on the back shore. It is the result of the interaction between the tides and the sloping shore and is in a dynamical equilibrium (Vandenbohede *et al.*, 2006a ; Lebbe, 1999 ; Van Meir & Lebbe, 1998).

Since 1967, freshwater has been extracted from the dune aquifer to produce drinking water. The pumping leads to a drawdown around the extraction wells. With the current extraction rate, influence of the water extraction on the study area around the inlets is, however, minimal. Two hydrogeological water divides exist among the dunes: the first one is located more or least in the center of the dunes, the second one is situated to the south of the water extraction zone.

Borehole	Depth (m under the surface)	Elevation ($mTAW$)	Thickness (m)	Clay content	Note
P11	-13	-6.6	7	High	Low clay content from -3.6 to $-6.6mTAW$
P12	-10	-2.8	9	Medium	
P13	-9.5	-3.3	11	High	
P14	-9.5	-2.5	9.5	High	
P15	-10	-3.6	9	High	
P16	-10	-7.9	6	High	Medium clay content from -2.9 to $-7.9mTAW$
P17	-9.5	-3.1	5.5	Medium	
P18	-11	-4	8	High	Low clay content from -1 to $-4mTAW$

Table 6.1: Description of boreholes - top of the clay layer (after Laboratoria Van Vooren, 2005).

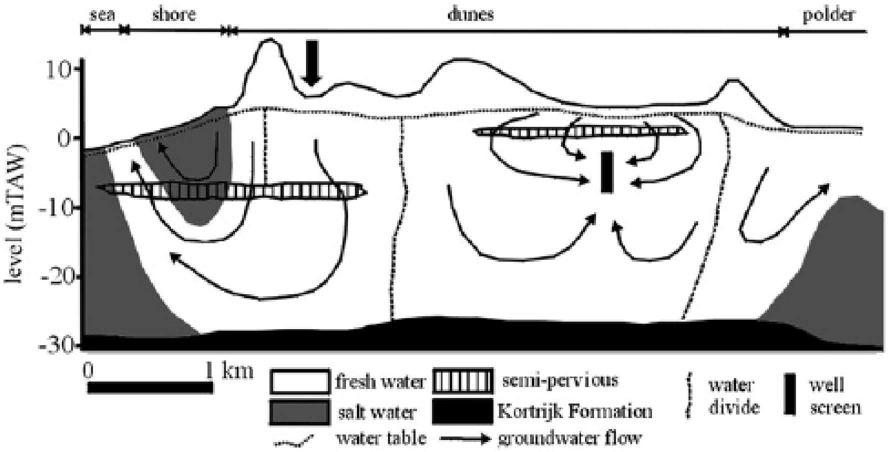

Figure 6.3: Scheme of groundwater flow, fresh/salt water distribution and position of water divides before infiltration. The black arrow indicates the position of the inlets (Vandenbohede et al., 2008a).

Without the extraction, only one water divide would be there. It would delimit the zones where the freshwater flows towards the sea or the polders (Vandenbohede *et al.*, 2008a).

The less permeable layers that are lying within the quaternary deposits led to secondary hydrogeological water divides (Vandenbohede *et al.*, 2008a). Figure 6.3 presents the situation before the building of the two artificial sea inlets. They brought changes in the water quality (salt water instead of freshwater), but could also cause variations in the water level distribution. It was very important to monitor this infiltration.

6.3 Evolution

The evolution of the sea water infiltration was monitored mainly by electrical conductivity measurements carried out by an EM39 device, fresh water head observations (taking into account the

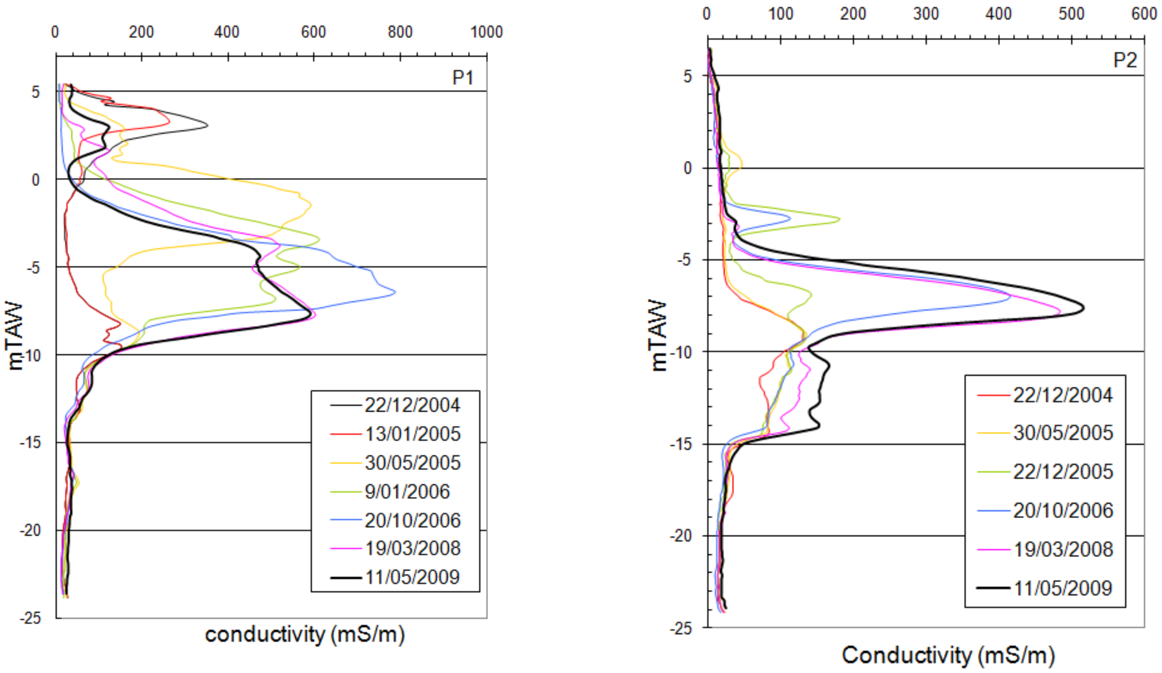

Figure 6.4: EM39 conductivity data in P1 and P2 (modified after Vandenbohede *et al.*, 2009).

density of water following salt content, deduced from water conductivity data) and temperature measurements carried out by divers. The last two of them were mainly used to evaluate how the infiltration was happening. It appears that salt water infiltrated the two artificial inlets during high spring tide or during storm events (Vandenbohede *et al.*, 2008a).

Several phases of EM39 measurements were performed since the creation of the two inlets. The first one was implemented from 2005 to 2006 (Vandenbohede *et al.*, 2008a); a second one in 2008 and a third one in 2009. Figure 6.2 shows the position of the different boreholes where the EM39 measurements were taken (Vandenbohede *et al.*, 2009). Figures 6.4 to 6.7 present part of this data, to show how the infiltration process evolved (all the data is presented in appendix A).

In P1 (figure 6.4), we can observe two peaks on 13.01.2005. The deepest one (between -8 and $-10mTAW$) is due to the lithology. Indeed, the conductivity of the dune aquifer is between 10 and $30mS/m$. Between -8 and $-10mTAW$, conductivity increases up to $160 - 180mS/m$ because of the presence of a clayey sand to sandy clay layer. It corresponds to the layer described in the previous section. This layer will have a very big importance during all the process of infiltration, because it acts as a semi-permeable layer. This layer is also seen in P2 between -12 and $-15mTAW$. The shallow peak ($230mS/m$) is due to salt water that infiltrates the dune area since there is a decrease at this depth on 30.05.2005 (Vandenbohede *et al.*, 2008a).

The role of the semi-permeable layer is illustrated in the next measurements. On 30.05.2005, we first see that salt water has moved deeper into the aquifer up to around $-4mTAW$. Later, on 20.10.2006, the movement in depth of the salt water is stopped by the semi-permeable layer because of its low hydraulic conductivity. It signifies that the lateral component flow becomes important; part of this flow is directed inside the dune area. This movement can be observed in P2, which is situated further from the pond than P1. We observe an increase in conductivity around $-8mTAW$ on 20.10.2006, whereas nothing was detected before. The salt water had to come from a lateral flow. In P1, the conductivity in the upper part of the aquifer decreased because less sea water was entering the dune (silting up of the inlet). The contrast with the salt water increased up to $800mS/m$ (Vandenbohede *et al.*, 2008a ; Vandenbohede *et al.*, 2009).

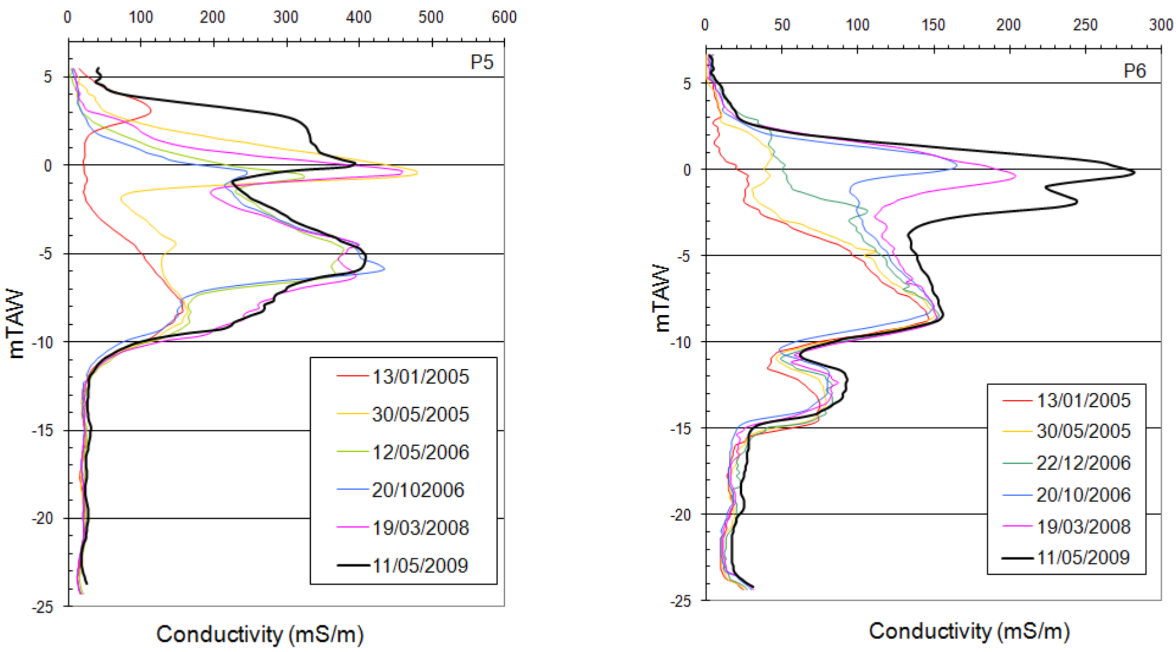

Figure 6.5: EM39 conductivity data in P5 and P6 (modified after Vandenbohede *et al.*, 2009).

However, the semi-permeable layer is not homogeneous. In some parts, the hydraulic conductivity is not so low. As a consequence, the vertical flow of salt water was not stopped and salt water could go deeper into the aquifer (Vandenbohede *et al.*, 2009). As we will see later, our results (chapter 8) tend to confirm this hypothesis.

Measurements taken in 2008 and 2009 showed that new salt water infiltrated in the ponds (figure 6.5). In several wells (P1, P5), an increase in conductivity is also observed within the semi-permeable layer. It signifies that fresh water in the pores is replaced by salt water. In some cases, salt water is even observed under the semi-permeable layer (P7, P8 figure 6.6) (Vandenbohede *et al.*, 2009).

Parallel to the vertical flow of infiltrated water, an increase in conductivity is also observed in wells situated further from the ponds (P2, P6, P8, P16), as already said for P2. It signifies that the lateral flow is also of importance everywhere in the ponds (Vandenbohede *et al.*, 2009).

The above evolution is mainly visible in the western inlet. In the eastern inlet, it seems that the semi-permeable layer continued to form a barrier of sufficient hydraulic resistance to hinder the vertical movement of sea water. Indeed, no increase in conductivity was observed under the semi-permeable layer (figure 6.7). In consequence, a lateral flow towards the dune can also be observed (Vandenbohede *et al.*, 2009).

In conclusion, we can say that even if salt water does not infiltrate the ponds anymore (at least in the western pond), it is important to see the evolution of saltwater in the dunes. The behavior of the semi-permeable layer is of great importance as it influences both vertical and lateral flows.

Borehole data gives us a good idea of the position in depth of the plume of salt water. However, this information is only available on the perimeter of the pond. One of our objectives is therefore to see where the limit between fresh and salt water is under the ponds themselves. Another valuable information, not available from previous studies, is the continuity of the infiltration between different boreholes. A third and very important unknown factor in this situation is how far the lateral flow entered the dune area. Indeed, we know from boreholes that this flow exists, but it is not known where the plume ends. It only appeared that no salt water was present

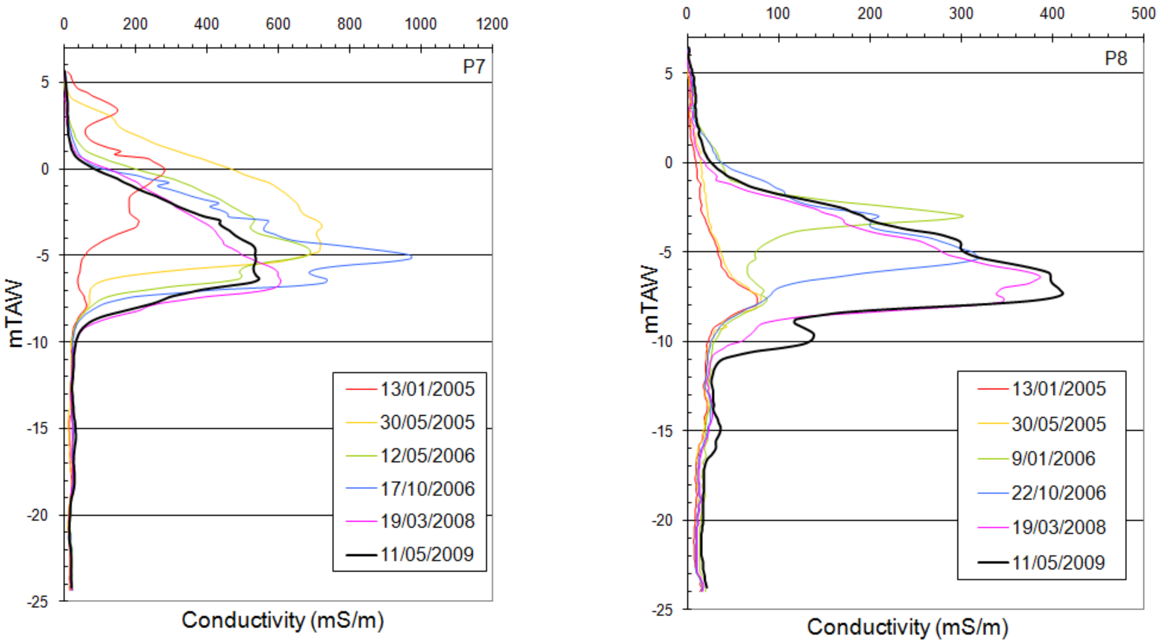

Figure 6.6: EM39 conductivity data in P7 and P8 (modified after Vandenbohede *et al.*, 2009).

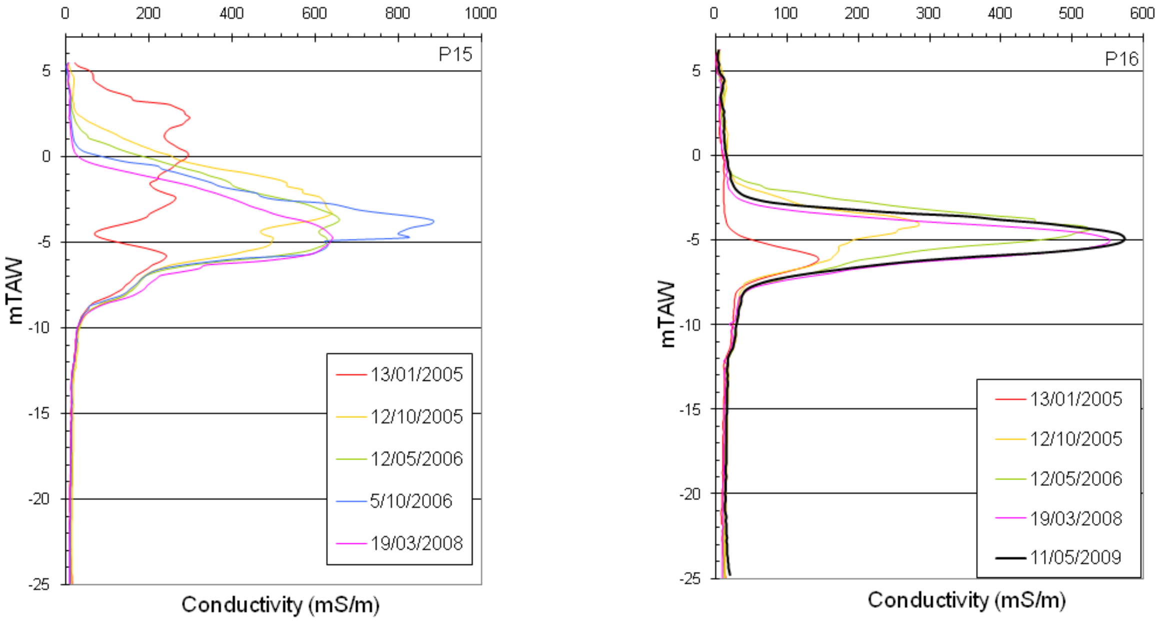

Figure 6.7: EM39 conductivity data in P15 and P16 (modified after Vandenbohede *et al.*, 2009).

in the wells P19, P20 and P22 situated along the "Konijnpad", further from the inlets (not visible on the figures). What happens between is only hypothetic. To answer those questions, ERT sections will be presented in chapter 8.

Chapter 7

Survey design

7.1 Modeling

Before the field campaign, a synthetic benchmark was carried out using available data presented in chapter 6. The aim of this modeling study was not to determine the inversion parameters (see chapter 4) but to decide what the best array was to investigate the specific site of the Westhoek.

7.1.1 Choice of the model

The model used is a simplification of the situation based on both drilling data (lithology) and EM39 data. It is shown on figure 7.1. We will summarize the important results below. Unfortunately, there was no EM39 background data available to have an idea of the resistivity distribution outside salt water. However, we can hope that the first measurements made in 2004 were not (too much) polluted by any intrusion. The model took into account the depth of the layer with clay content, which is around $10m$ under the surface. The thickness of this layer was chosen at $3m$. The borehole data let us think that it is an underestimation, but on the EM39 data, a change in resistivity was observed, but only on a limited thickness. The resistivity of this layer was taken at $10\,Ohm.m$ ($100\,mS/m$). This layer is surrounded by saturated sands with a resistivity of $100\,Ohm.m$. The unsaturated zone was not modeled because it was not clearly visible on the EM39 logs. However, it appeared later that the resistivity of dry sands was much bigger, leading to a very high contrast in resistivity values. The salt water intrusion was modeled by a $2m$ thick layer with a lateral extension of about 65 (electrode spacing of $2m$) or $100m$ (spacing of $3m$). The resistivity was taken equal to $2\,Ohm.m$ ($500\,mS/m$). At a depth of $33m$, the formation of Kortrijk is modeled with a resistivity of $50\,Ohm.m$.

7.1.2 Results

Knowing the characteristics of the different arrays (Dahlin & Zhou, 2004 ; Loke, 2004 ; see chapter 2), two different arrays were tested with $2m$ and $3m$ electrode spacing: dipole-dipole and Wenner-Schlumberger. The data sets were created with RES2DMOD (Loke, 2002) and a level of noise of 5% was applied. It soon appeared that a spacing of $2m$ was not able to resolve this problem accurately because the depth of investigation was only about $20m$. As it was also interesting to investigate deeper in the dunes (the salt water could have crossed the less permeable barrier), it was preferable to increase the electrode spacing up to $3m$. Figure 7.2 shows the results of inversion (smoothness constraint) and the corresponding sensitivities. We see that the sensitivity is about 0.5 in the salt water but decreases rapidly in depth. We could use $2m$ electrode spacing if the depth was well estimated (for example in a second field campaign). For the Wenner-Schlumberger array, the depth of investigation was lower; it was thus excluded to use this array with such a spacing.

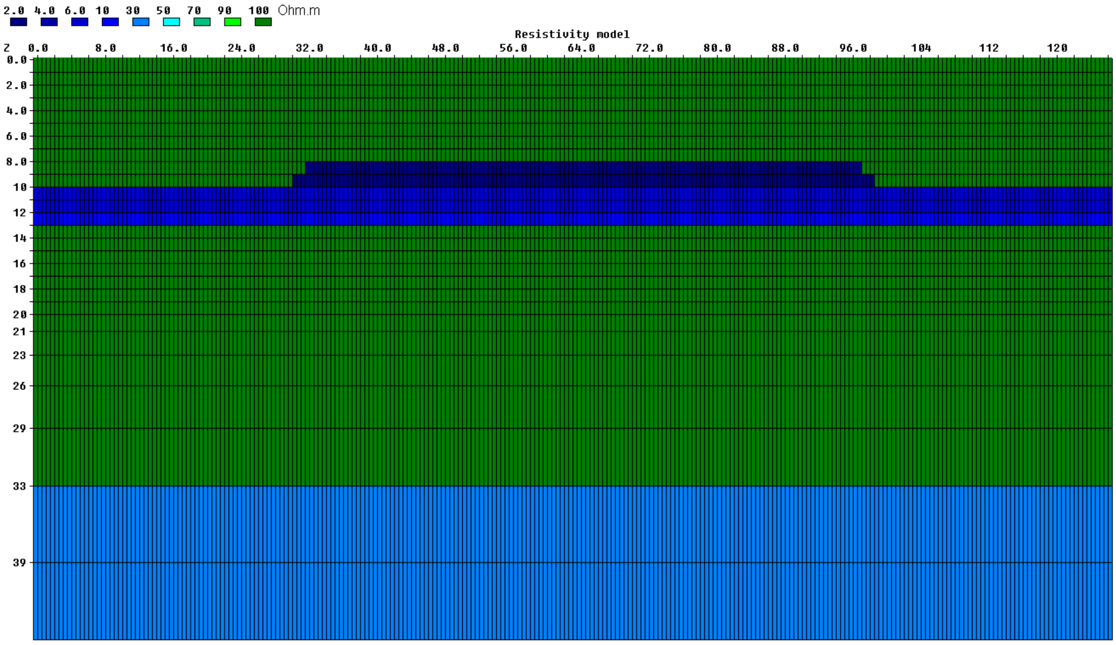

Figure 7.1: Model of the field based on borehole data.

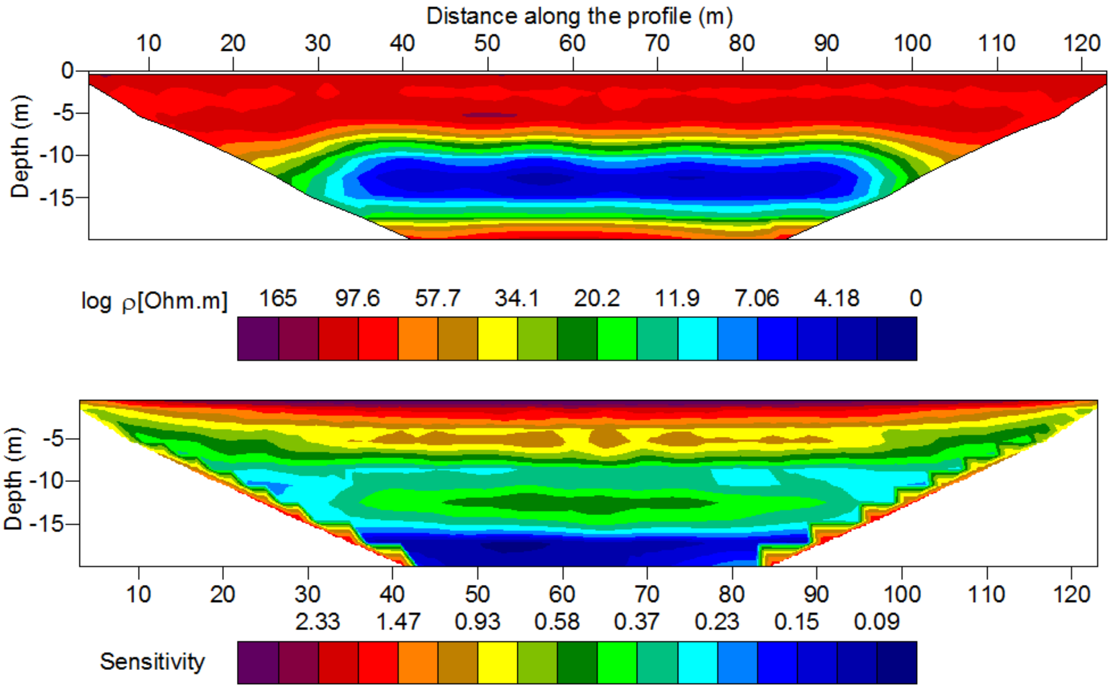

Figure 7.2: Inverted model for a dipole-dipole array, $2m$ electrode spacing (top) and corresponding sensitivity (bottom).

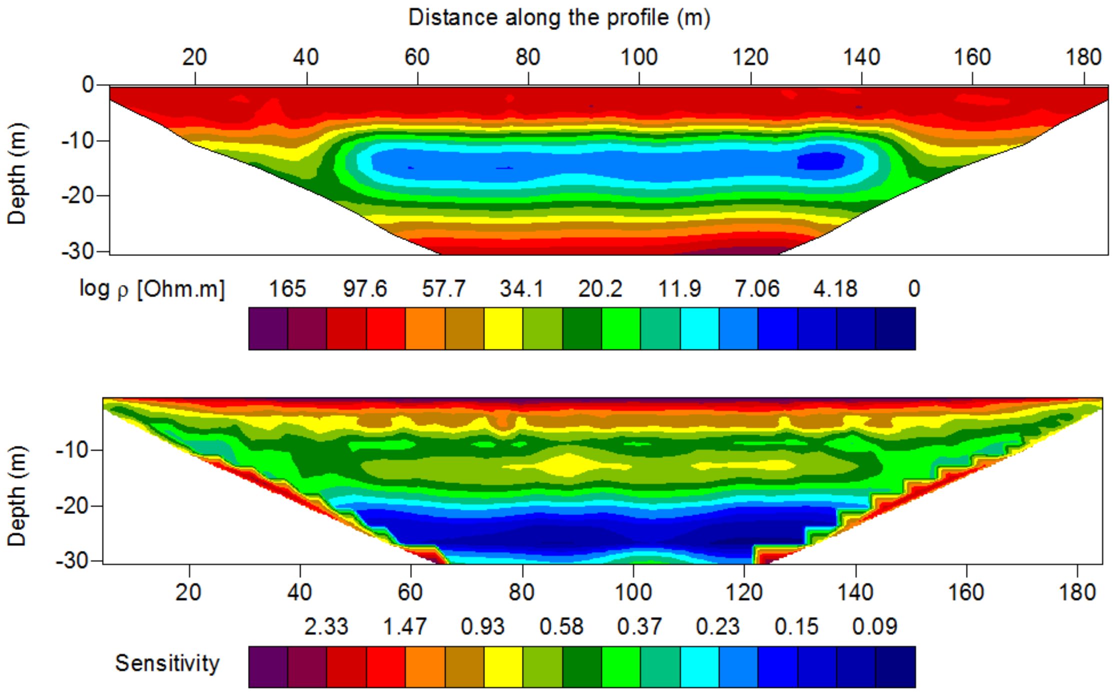

Figure 7.3: Inverted model for a dipole-dipole array, $3m$ electrode spacing (top) and corresponding sensitivity (bottom).

The first results showed that the minimum reliable electrode spacing should be greater than $2m$. It is why the modeling was continued with a spacing of $3m$. Figure 7.3 presents the results for the dipole-dipole array. Figure 7.4 displays the inverted model for the Wenner-Schlumberger array. The problem of the depth of investigation is well resolved, and the sensitivity at the position of the salt water is now around 0.8 for the dipole-dipole and 0.5 for the Wenner-Schlumberger.

First we see that both configurations are able to find the resistivity of the sands in the first layers. If we compare both configurations, we see that the dipole-dipole detects the true depth of the salt water (beginning of the decrease in resistivity) at $8m$ while the Wenner-Schlumberger tends to put it somewhere deeper. Then, it appears that it is impossible to detect the limit between the layer with clay content and the salt water because the contrast is too small. The minimum resistivity value (superior to the real one) seems to correspond to the transition clayey sand/clean sand. It is situated at $13m$ for the dipole-dipole and $15m$ for the Wenner-Schlumberger. During the interpretation, we will have to be careful when positioning the clayey layer.

In depth, with the dipole-dipole configuration, the resistivity of the saturated sands is well recovered after inversion, while it is not the case for the Wenner-Schlumberger array (smaller resistivity values around $50\,Ohm.m$). To detect the clay of the formation of Kortrijk, larger electrode spacing should be used, but it would be at the expense of resolution in the most interesting part of the dunes.

With $2m$ electrode spacing, the resolution is more favorable and we find minimum resistivity value close to the one of the model ($2\,Ohm.m$). With $3m$, there is a loss of resolution, and the minimum resistivity value is higher (around $7\,Ohm.m$). The results are worse for the Wenner-Schlumberger.

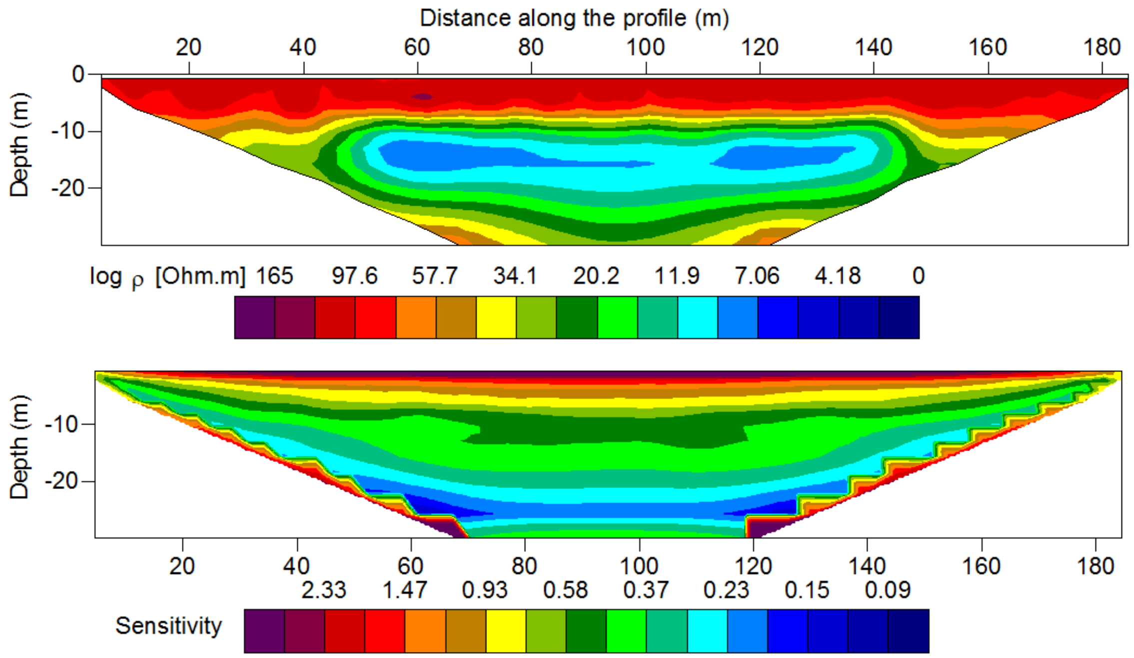

Figure 7.4: Inverted model for a Wenner-Schlumberger array, $3m$ electrode spacing (top) and corresponding sensitivity (bottom).

7.1.3 Conclusion

Although the modeling is quite limited, it appears that the dipole-dipole configuration has a larger depth of investigation. As it was expected, the resolution of the dipole-dipole array is better. It enables to find the position of the salt water intrusion more accurately, but also to find resistivity values closer to the real values than the Wenner-Schlumberger array.

The change in resistivity being due to different causes, e.g. water salinity but also lithologic change (clay content), the interpretation is not easy. Indeed, the limit between the clayey layer and the sands with salt water is not observable by a resistivity contrast.

According to these results, it was chosen to use a dipole-dipole array with $3m$ electrode spacing on the field. In addition to a better resolution, this array enables to take advantage of a multi-channel resistivity measurement device such as the Syscal Pro. As such a device was available for the field campaign (University of Bonn, Germany), the use of a dipole-dipole array enabled to take both normal and reciprocal measurements, and thus to have an idea of the error level required for the inversion (chapter 8).

7.2 ERT campaign

7.2.1 Introduction

The field campaign was carried out in the beginning of March, from 5^{th} to 10^{th}. During this campaign, it was decided to focus on the smallest infiltration pond for several reasons:

- the distances are less important in the eastern pond, it allows to use smaller distances between electrodes to cover the area and thus to obtain a better resolution;
- logistics is easier because the distance to transport the equipment is reduced;
- the geological conditions are such that the layer with higher clay content seems less permeable under the eastern inlet than the western one. This is shown by the EM39 measurements where we see that the infiltrated water flowed deeper in the western pond. So,

the lateral flow is more worrying in the smaller pond because the barrier is acting more strongly;

- the eastern pond is in a worse hydrogeological situation. Indeed, there is no idea about the position of the intrusion in the direction of the water catchment. As it seems that this intrusion goes further in this pond, it seems safer to investigate firstly this pond;
- the western inlet is completely silted up by sands. It means that there is no new infiltration in this pond. In contrast, the second inlet is still open and the sea could invade the pond during very high tide or maybe storm events.

The modeling showed that a spacing of $3m$ between electrodes should be sufficient to reach the target depth of investigation (about $30m$, approximate position of the Kortrijk formation). It was decided to keep this distance for all profiles to simplify the interpretation. Indeed, in this way, all the profiles have the same resolution and it is possible to compare them.

The first day of the field campaign was dedicated to a test (see below, profile 1). It was decided to carry out normal and reciprocal resistivity measurements. In this way, it was possible to analyze the error and to see if it was possible to use the dipole-dipole array to obtain good inversion results (even if the signal to noise ratio is reduced). This process will be described in chapter 8.

In addition, induced polarization measurements were taken in the time-domain. The residual voltage was measured after the current was switched off. Their aim was to distinguish the layer with clay content of the clean sand. Indeed, clay minerals are responsible for the membrane polarization effect (Telford *et al.*, 1990). A layer with high clay content should display a higher value of chargeability $[mV/V]$ than any other ones.

Unfortunately, it rapidly appeared that induced polarization measurements were polluted by very high repeatability errors. In addition, the inversion process led to high RMS error and erratic distribution of the chargeability. It was thus decided to give up this type of measurements for the rest of the field campaign. We attribute this problem to the very high resistance contact that can occur in dry sand, and therefore the difficulty to pass and measure low currents in the ground; and to the relatively high salinity of the subsurface which lower considerably polarization phenomena.

It also appeared that the resistivity was quite high in the dune where the sand on the surface is dry, compared to the pond area. As it will be shown in the "data error analysis" section (chapter 8), it seemed that some measurements corresponding to low resistance values were very sensitive to noise and displayed high repeatability errors. However, the treatment of profile 1's data clearly showed that it was possible to obtain good inversion results if an estimation of the errors using reciprocal measurements was done. It is why other profiles were also taken using a dipole-dipole array and both normal and reciprocal measurements.

In an attempt to clarify the text, the different profiles will be described in terms of technical survey design (positioning, electrode spacing and numbers, etc.) in the next sections (7.2.2 to 7.2.7). Since, the latter may be not of interest to all readers, one will find the discussion of the results in chapter 8. The approximate position of the different profiles is given in figure 7.6. On the field, the exact position of each electrode was taken with a differential GPS. The general objective was to cover the pond in two directions (parallel and perpendicular to the coast line) to detect the sea water infiltration and to see its lateral migration. For profiles parallel to the coast, the zero was placed in the south-west direction. For perpendicular profiles, the zero was lying landward, in a south-east direction. To illustrate the following sections, figure 7.5 offers a general view of the pond. It should enable the reader to better understand the discussion about 3D effects, effect of dry sand, etc. This picture was taken from the east towards the west, a pictogram indicates the position on figure 7.6.

Figure 7.5: View of the pond from the east towards the west.

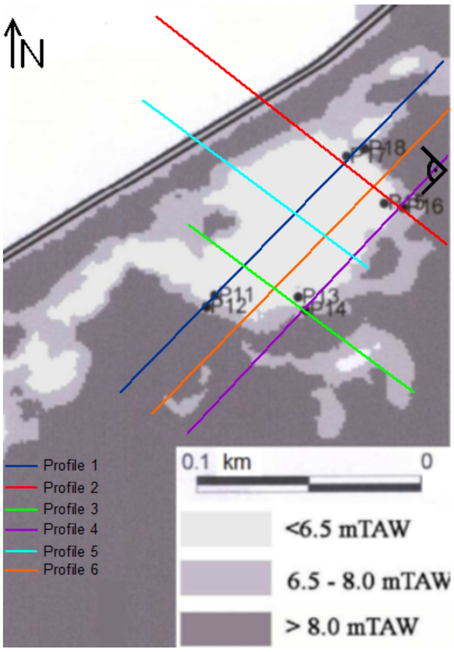

Figure 7.6: Location of the profiles.

As the density of measurements is quite high, one could suggest making a 3D inversion. However, the distance between profiles is too high ($20m$ on average) to improve the 2D results. Ideally, the distance between profiles should be the same as the electrode spacing ($3m$). The time spent on the field to obtain so many measures would have been too long whereas a 3D inversion without them would have led to simple interpolation between profiles since no true 3D information is present in the data.

7.2.2 Profile 1

Profile 1, composed of 72 electrodes, was almost parallel to the coast and went through the well P11, P12 and P18. The well P17 was not found anymore because it got stuck in the sand. P11 is located between electrodes 22 and 23, $64m$ away from the beginning of the profile. P12 is located near electrode 20 at abscissa $57m$ and P18 is located between electrodes 56 and 57, $167m$ away from the beginning of the profile.

The beginning and the end of the profile (beyond the wells) are situated in the dune area, whereas the rest of the profile is located in the pond. However, the small dune in the pond (end of profile 3) is larger than in figure 7.6. In consequence, electrodes 26 to 37 were at the bottom of this dune (the bottom corresponds to the intersection between profiles 1 and 3).

As far as the effects of 3D are concerned, we can hope that there are not too important for the topography. Indeed, the topography is almost the same at both sides (except for the dune mentioned above), we can expect the resistivity distribution to be quite homogeneous. In addition, the profile is more or less in the middle of the pond and the distribution of sea water should be quite symmetric on both sides of the profile.

7.2.3 Profile 2

Profile 2 is perpendicular to the coast. It is the longest profile since it was carried out with 96 electrodes. However, for the last roll-along[1], only normal data was taken. It is why the interpretation is done on a shorter profile (72 electrodes), because an error estimation was needed to obtain results comparable to other profiles. Profile 2 went through P16, located at electrode 20 ($57m$ away from the beginning of the profile). The limit between the pond and the beach (i.e. the dyke) is comprised between electrodes 50 and 52 around abscissa $150m$.

The end of the profile is on the beach. It enables us to detect the sea water lens under the beach and a possible connection between this lens and salt water coming back from the pond. Unfortunately, the profile was not long enough to reach the position of the fresh water flow.

After P16, few 3D effects are expected, because the profile was far enough from the dune to the north-east. In the beginning of the profile, among the dune area, some 3D effects are possible due to the topography. Indeed, it was also changing laterally in this zone.

7.2.4 Profile 3

Profile 3 was also perpendicular to the coast and was composed of 48 electrodes. It was centered on P14 (25^{th} electrode, $72m$ away from the beginning of the profile).

As far as the possible 3D effect is concerned, we can expect the distribution of resistivity to be quite homogeneous on both sides of the profile. However, the topography effect might have an impact in the dunes, just like in profile 2.

7.2.5 Profile 4

Profile 4 was a profile of 72 electrodes, parallel to the coastline. However, a small deviation is observed at the beginning of the profile. It was due to the topography. Indeed, at this part of the profile, it was difficult to distinguish the rest of the profile to carry out a straight one. Initially, this profile had to go through P14 and P16 to have two wells. However, due to the vegetation made up of barbed bushes, it was necessary to deviate the profile slightly. In consequence, it only went through P14, located at electrode 28, which corresponds to abscissa $81m$. P16 was only located at a distance of about $6m$ away from the profile, landward.

For this profile, all the electrodes were outside the pond. Thus, we expected to find higher resistivity values in the middle of the profile than with other parallel profiles.

---

[1] One cable corresponds to 24 electrodes, two cables were available. To carry out a profile of 72 electrodes, it was necessary to move the first cable.

Unfortunately, 3D effects may be quite important in this case. Indeed, from electrode 28 to electrode 57, the electrodes were lying close to the base of the dunes on one side, and near the infiltration pond on the other side. In addition, the lateral flow of sea water is expected to be limited; it signifies that the resistivity distribution might be quite different on both sides.

This profile seems to be the less favorable for a quantitative interpretation, but it will bring important qualitative information about the intrusion.

7.2.6 Profile 5

Profile 5 was perpendicular to the coast, at (approximately) mid-distance between profiles 2 and 3. It was composed of 48 electrodes. Initially, it had to be exactly parallel to profile 3. However, due to the bushes again, it was not possible to place the profile in the dune area. It is why this profile was moved forward in the direction of the beach. There are no wells located on this profile.

The profile crossed the dyke between electrodes 31 and 33, which corresponds to abscissa 90 to 96m. The end of the profile is thus located on the beach.

Few 3D effects are expected as this profile is almost centered on the infiltration pond; the distribution of resistivity should be quite symmetric. Some problems could appear near the dyke, because the dunes were only present on the south-western side of the profile. However, the base of the dune was not so close, and the length was limited (tenth of meters). Some problems could also appear where the profile is located under the bridge, at the entrance of the pond (the same is possible for profile 2).

7.2.7 Profile 6

Profile 6 was a profile of 72 electrodes, parallel to the coastline, located at mid-distance between profiles 1 and 4. There were no wells on this profile.

There should not be important 3D effects on this profile. It is located almost in the middle part of the pond. In the dunes, the topography could have an effect, but the profile was perpendicular to the main direction of the dunes, even if there were some changes in the topography.

For this profile, it was also possible to take the data with a Wenner-Schlumberger array. Reciprocal measurements for this array were taken only for the roll-along part. It will enable us to observe the difference between the two arrays.

7.3 EM39 measurements

On 20^{th} April, a second field campaign was organized to take conductivity measurements with the EM39 device in the five accessible wells of the smallest pond. These measurements were not taken previously because the logging device was being under repair.

Even if six weeks separated both types of measure (ERT and EM39), we can assume that the salt water intrusion did not change. Indeed, we will see (chapter 8) that conductivity distribution did not vary a lot within one year, one month thus seems negligible. In addition, weather conditions were the same during the two campaigns: sunny and very little rain on the previous days (no fresh water infiltration).

Conductivity measurements were taken every 20cm along all the height of the well (about 30m). We can assume, according to the description of the geology, that the conductivity distribution is axi-symmetrical around the well.

Chapter 8

Field results and interpretation

8.1 Data error analysis

8.1.1 Introduction

Data quality plays an important role in inverse problems. All desired information of the field subsurface parameters is included in this data. However, the data is always polluted by some noise. Noise can arise from different factors (Slater *et al.*, 2000):

- errors due to the background noise (sporadic);
- errors due to the measurement device (random);
- errors due to a bad contact between an electrode and the soil (systematic).

The estimation of the error made on the measurement data (noise) is very important as it can lead to a misinterpretation during the inversion process (LaBrecque *et al.*, 1996). Indeed, an overestimation of the level of noise can lead to the final image being smoothed. In contrast, when the error is underestimated, the inversion algorithm will try to achieve this level by creating rough and irregular structures that are artifacts of inversion. There are two common ways to assess data errors (Robert *et al.*, 2009): repeatability errors and reciprocal errors.

Repeatability error (or stacking error) measures the standard deviation of several successive measurements. A common feature of an electrical resistivity device is to take the same data point several times until a fixed standard deviation or a maximum number of stacks is obtained. However, the repeatability error, if it is a quality indicator, generally gives an idea of precision and not accuracy (Robert *et al.*, 2009). Indeed, in some cases, the mean value which is calculated is a good estimator of the true value.

Reciprocal measurements are taken by switching current and potential electrodes. Normally, as explained in chapter 2, this process should not change the value of resistance (Parasnis, 1988). In contrast with repeatability measurements, during reciprocal measurements, some factors are changed such as injected current, electrode polarization or measured voltage. It reduces the amount of systematic errors but does not eliminate all of them (LaBrecque *et al.*, 1996). It signifies that reciprocal error is a better estimate of noise level (Slater *et al.*, 2000).

Slater *et al.* (2000) propose a general procedure to assess the level of noise in a data set. The reciprocal errors is defined as

$$e_{N/R} = R_N - R_R \tag{8.1}$$

where R_N and R_R are the normal and the reciprocal resistance. They propose a model in which the reciprocal error varies with the resistance

$$|e_{N/R}| = a + bR \tag{8.2}$$

where a represents the minimum error and b defines the increase of the error with the resistance. These parameters are determined by the envelope that contains all the points after removal of outliers.

There are other possible procedures to assess the level of noise. Koestel *et al.* (2008) defines another method to find the parameters. They sort the resistances into logarithmic equally sized bins and calculate the standard deviation of the reciprocal errors in each bin. Then, they defined also a and b to fit

$$\varepsilon = a + bR \tag{8.3}$$

where ε is the standard deviation of the reciprocal error.

8.1.2 Wenner-Schlumberger data set

To evaluate the level of noise of the Wenner-Schlumberger array, reciprocal data points were taken out of a sample of 416 points at all depths of investigation. Due to the greater time demand, data points were not taken for other profiles, in contrast with the dipole-dipole array.

First, obvious outliers were removed. As the Wenner-Schlumberger is a quite robust array, all points with a repeatability error greater than 10% were eliminated. The remaining repeatability error has a mean value inferior to 1%. Points with a relative reciprocal error superior to 50% were also removed. 375 points were remaining. The mean reciprocal error is equal to $-0.0097\,Ohm$ and the standard deviation is $0.1112\,Ohm$. The histogram is presented on figure 8.1 and the envelope following Slater *et al.* (2000) is shown on figure 8.2.

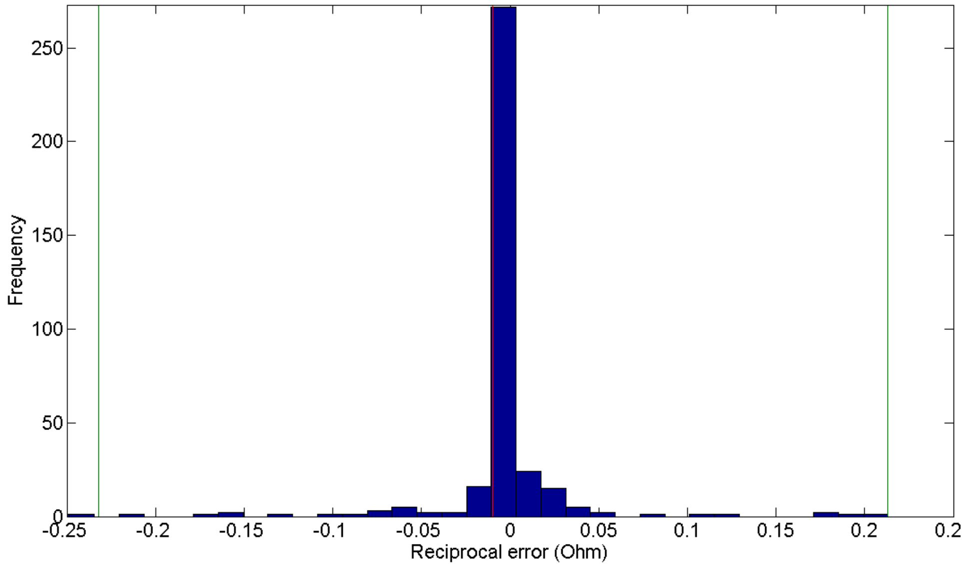

Figure 8.1: Reciprocal error distribution for the Wenner-Schlumberger array, in red the mean value, in green the 2σ interval.

We see on figure 8.2 that the definition used is highly dependent on the distribution of the points and the presence of some points with higher reciprocal error. Indeed, we find a minimum error of $0.24\,Ohm$, whereas the least-square solution only gives $0.0053\,Ohm$. The true minimum error certainly ranges between these two values, around $0.05\,Ohm$. The relative change is less than 1% in both cases. Note that we can also find an envelope curve with completely different parameters: minimum error of $0.05\,Ohm$, but a relative change of 5%. It is thus very difficult in this case to find the good values to fit the chosen law.

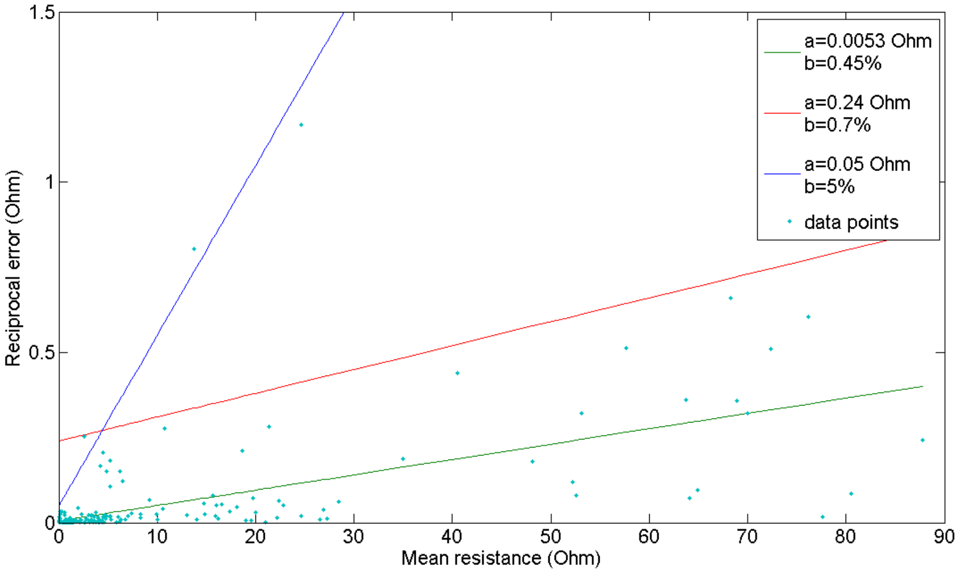

Figure 8.2: Envelope of the reciprocal error for the Wenner-Schlumberger array.

8.1.3 Dipole-dipole data sets

Since the field campaign was implemented with a dipole-dipole array and always with reciprocal measurements, a lot of points were available to study the distribution of the reciprocal error. Since the dipole-dipole is sensitive to noise, a lot of data had a quite high repeatability error. However, the first inversions showed that it was possible to obtain images of good quality by using the reciprocal measurements.

To analyze the reciprocal error, all the data with a standard deviation superior to 50% were removed. This value can appear to be high, but a lot of points displayed a small resistance due to the presence of salt water. Even a small absolute error can lead in these cases to a high stacking error. Then, the points with a reciprocal error superior to 100% were removed. After that, 4417 points were remaining.

The mean reciprocal error is $-0.0033\,Ohm$ and the standard deviation is equal to $0.1205\,Ohm$. Several points are quite outside the distribution (up to $2.5\,Ohm$ of reciprocal error), but they correspond to high resistance measurements (relative error less than 10%). The histogram is shown on figure 8.3. The majority of the measurements have an absolute error close to zero. But this is not very representative as a lot of data display very low resistance value.

Figure 8.4 gives the variation of the reciprocal error with the resistance and the parameters for the envelope and the least-square solution. The envelope curve is manually fitted; thus, the points that seemed to show a very big error were left out the envelop. The minimal error is closed to the one found for the Wenner-Schlumberger array : $0.23\,Ohm$. The relative change is about 5%. Again, we can think that the envelope given by this method overestimate the true distribution of the reciprocal errors. The set contains more than 4000 points and only few of them show large reciprocal errors. If we neglect some points, we can fit an envelope with a minimal error of $0.05\,Ohm$ and a relative error of 5%.

What is interesting in the data error analysis is the distribution of the relative error with the resistance measured. We see on figure 8.5 that above the resistance of $1\,Ohm$, all the relative reciprocal errors are less than 10%. In contrast, below this value, the distribution shows error ranging from 0.001 to 100%. It signifies that small resistance values are more likely to present large variation. All these resistances are related to salt water intrusions.

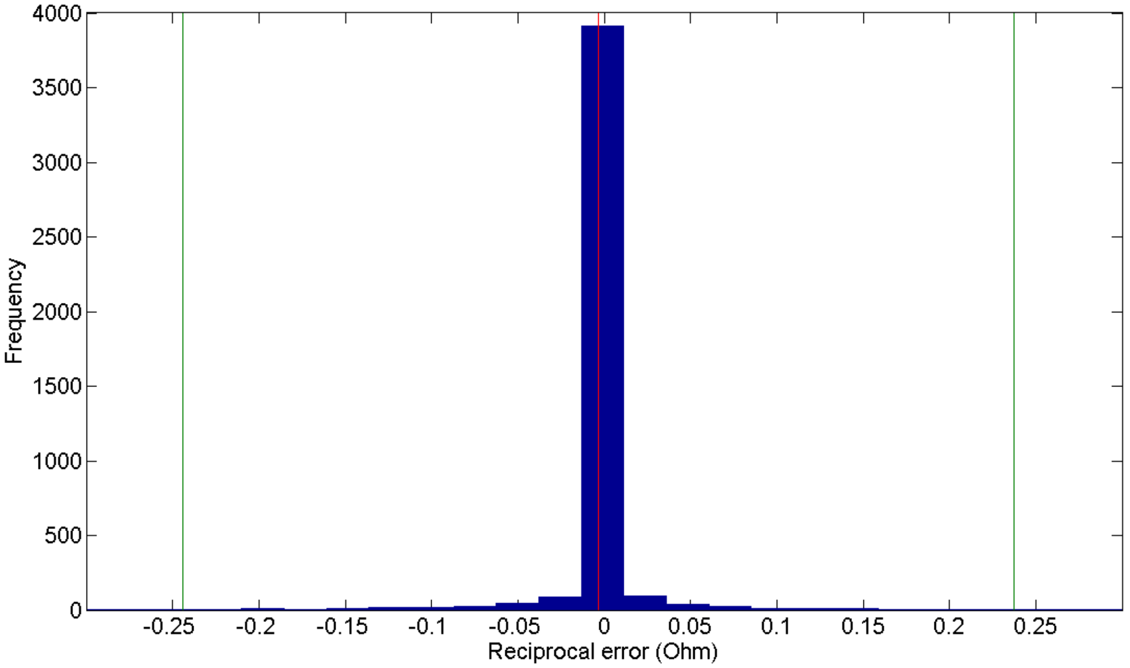

Figure 8.3: Reciprocal error distribution for the dipole-dipole array, in red the mean value, in green the 2σ interval.

The analysis of the repeatability error shows the same trend. Low resistance measurements are more likely to have a large standard deviation (in %).

8.1.4 Conclusion

Even if the Wenner-Schlumberger array displays smaller repeatibility errors, the reciprocal error shows a quite similar distribution compared to the dipole-dipole array. In both cases, we could fit a envelope with a minimum error of $0.05\,Ohm$ and a relative error of 5%. First inversions also showed that the Wenner-Schlumberger data set did not allow to obtain better results. It justifies *a posteriori* the choice of the dipole-dipole array.

The first idea after such an analysis could be to eliminate all the points which exceed a certain value of reciprocal or repeatability errors. The difficulty with such a set of data would be to find the cut-off value to sort the data.

As explained before, the repeatability error gives an idea of precision and not accuracy whereas it is difficult to give a cut-off value for the reciprocal error (which should be based on the absolute or relative error).

Instead of using this method, which can be easily implemented for data set with low error (it is sufficient to delete the obvious outliers), it was preferred to use the opportunity given by the reciprocal error assessment. Indeed, as explained in chapter 2, it is possible to use it to weight the data. In this way, the importance of the data with a high error will be lower than the other. Each data will be fitted to its supposed noise/error level. It enables to keep the information given by the points with low resistance (linked with salt water) but with a high reciprocal error. The detailed method will be exposed in the following section.

8.2 Data selection

During the first phases of interpretation, the aim was to determine a common method to sort the data. We saw in the previous section that some data points display a high repeatability error,

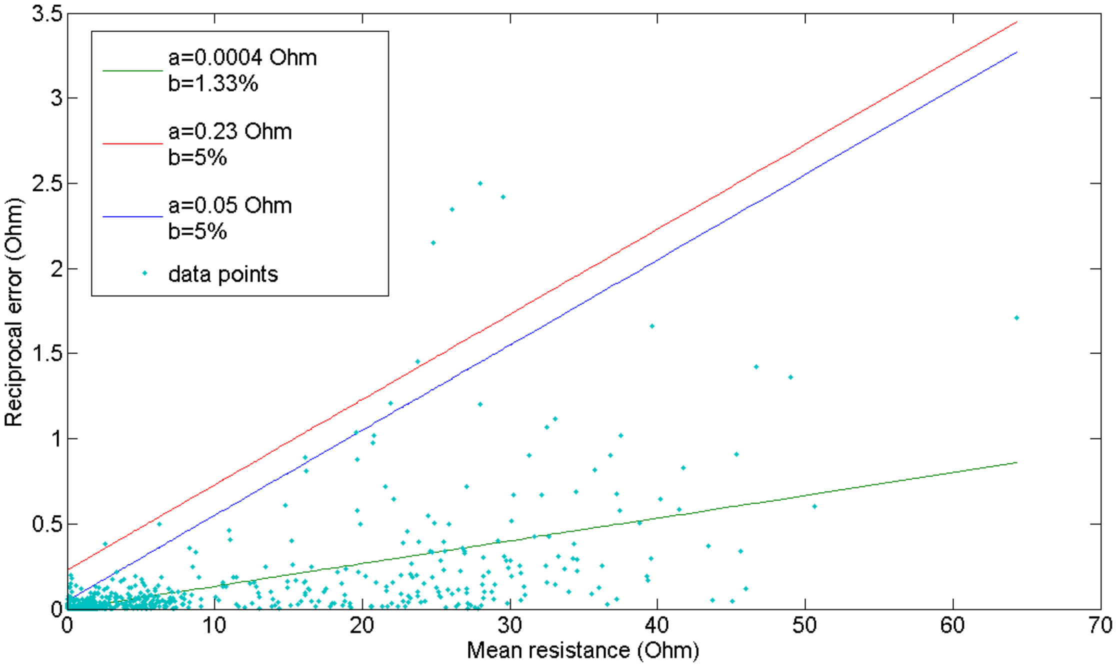

Figure 8.4: Envelope of the reciprocal error for the dipole-dipole array.

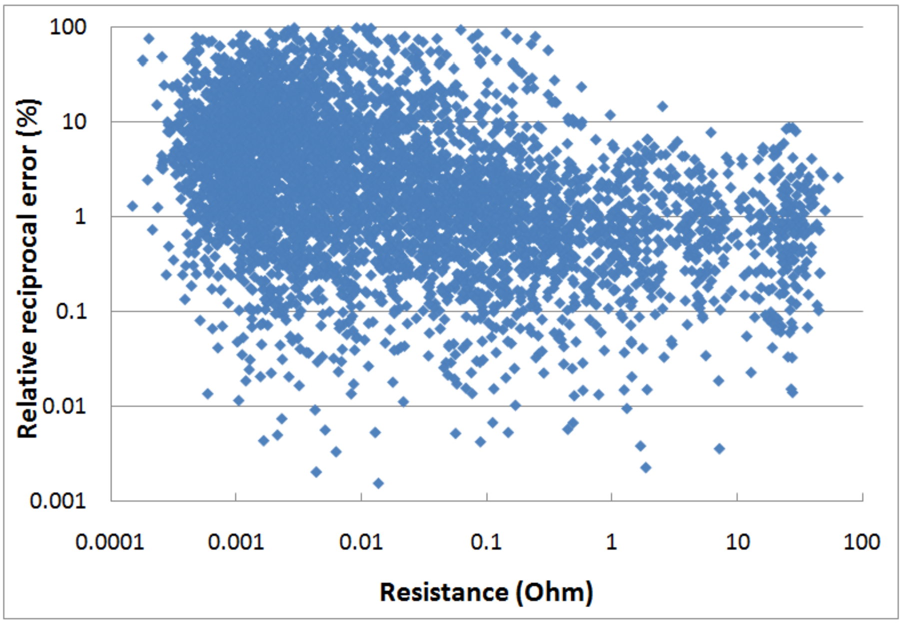

Figure 8.5: Relative reciprocal error according to the mean resistance.

but that this feature was certainly due to the very low resistance of the subsurface in the area concerning by the sea water intrusion. An average value, even with a high standard deviation, may have been a good estimate of the real value and could bring important information during the inversion process.

In addition, the reciprocal measurements enable us to assess the quality of the data by giving a hint of the error and a second estimation of the resistance corresponding to a quadripole. It was thus preferable to combine both types of error to sort the data and remove outliers. The normal (reciprocal) measurement also happened to be of better quality than the reciprocal (normal) one. This was illustrated by a lower standard deviation or by the fact that one of the two data was clearly wrong (negative resistance for example). Considering these facts, a procedure to sort the data was implemented, considering different cases.

1. A limit of repeatability error of 5% was chosen as cut-off value; about 60% of the measurements were below this value. If only these measures had been kept, a lot of information would have been missing and the results would not have been reliable.
2. When both normal and reciprocal measurements were below this cut-off value, an average resistance was taken and the reciprocal error was used as an error estimation.
3. When one or both measurements display a repeatability error greater than 5%, an evaluation of the difference of quality was done. If the greater error was less than two times the smaller one, an average value was taken as a resistance value. If it was not the case, the resistance value of the measurement with the smaller repeatability error was kept. In both cases, the reciprocal error was used as an evaluation of the error.
4. If one of the measurements was wrong, the other one was used as a resistance value and the error estimation was supposed to verify the relation determined in the section above (minimum error of $0.05\,Ohm$, relative error of 5%).

An "average standard deviation" was calculated by means of the same method as the resistance value. It is not a standard deviation from a statistical point of view, but a parameter used to determine if the resistance value selected by means of the method comes from valid data or not. A value of 50% was chosen for this parameter to eliminate bad data points considered as outliers.

At this stage of the process, we can state that the selection process is very arbitrary and keeps a lot of data that could be wrong. This was done because it is very difficult to know if a mean value is a good estimate of the true value. A possibility to achieve this is to analyze the pseudo-section.

The pseudo-section simply displays the apparent resistivity value calculated at a position depending on the quadripole. It seems quite logical that quadripoles close to each other have not too different apparent resistivity. If it is not the case, one of the measurement points is certainly invalid.

In the RES2DINV software, this possibility is carried out by the option "exterminate bad datum points". The points are represented following the depth level (one value of a and n corresponds to a level) and the position of the electrodes. An example is given on figure 8.6. We see that obvious outliers are quite easy to eliminate. However, it is more difficult to decide if small variations are due to the resistivity distribution or to bad data. This option was used to remove outliers from all the data sets.

After that, an inversion was carried out with RES2DINV software for each section (with individual error estimation). A robust norm for the data was used to decrease the influence due to possible remaining outliers. After inversion, this software gives the possibility to see the distribution of the data misfit. Thus, we can see if a data point is well fitted after inversion,

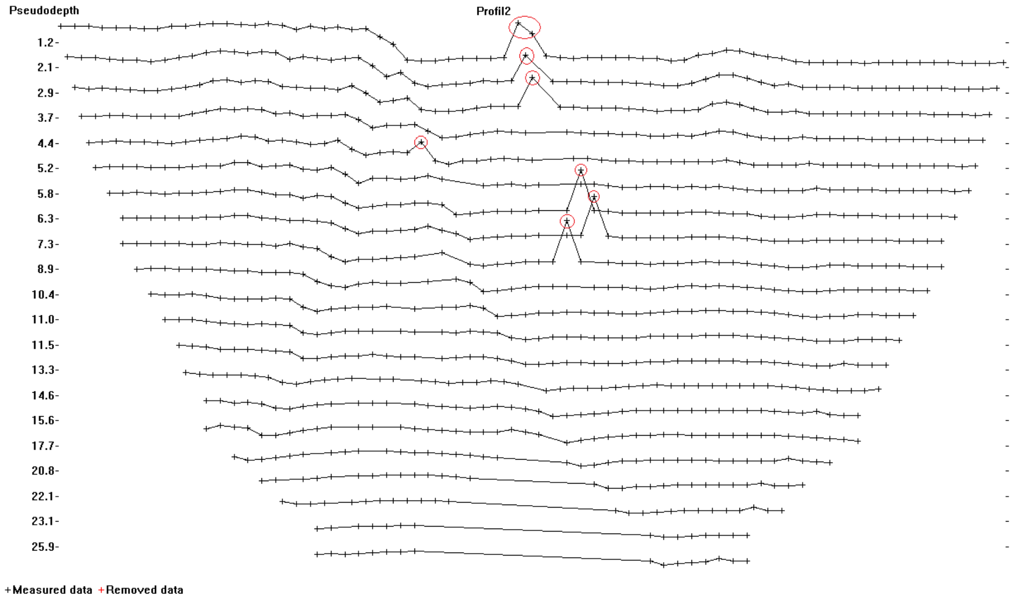

Figure 8.6: "Removed bad datum points" option. Red circles show bad data.

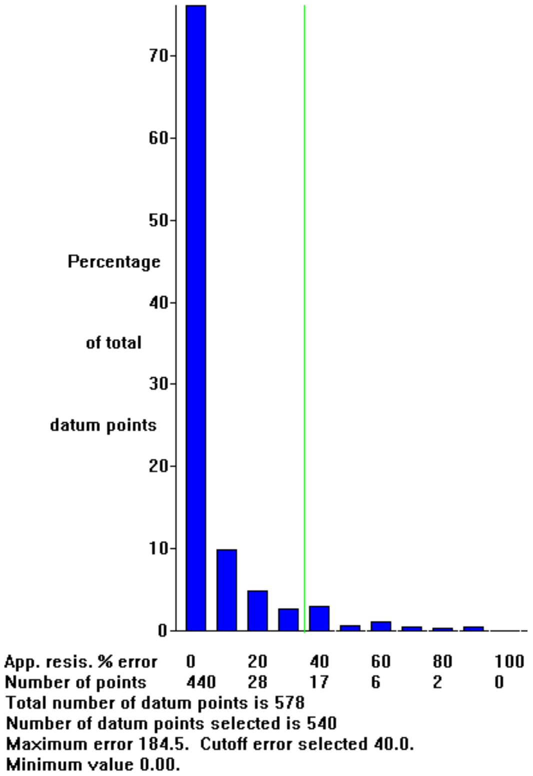

Total number of datum points is 578
Number of datum points selected is 540
Maximum error 184.5. Cutoff error selected 40.0.
Minimum value 0.00.

Figure 8.7: Error distribution.

and we can eliminate data which displays too big errors. This is illustrated on figure 8.7, which gives an example for Profile 3. It is possible to choose a limit of the percentage error to remove some data. After an analysis of every set of data, a limit of 40% was chosen.

Profiles 2 and 5 displayed a quite different distribution of the error and a lot of points had a much bigger error. This can be explained by the fact that part of these profiles were located on the beach with sea water (and thus very low resistivity values) just below the surface. The general resistivity distribution of these profiles was not the same; it could be also true for the error after inversion.

As we will see in the next sections, this data selection enabled us to obtain reliable results even if the repeatability errors were quite high. In such a case, it was thus very important to carry out a quality analysis and to remove bad data points.

8.3 EM39 measurements and water level

In this section, new conductivity measurements made on the wells with the EM39 device are presented. They are compared to the ones made one year before to evaluate the evolution of the intrusion. The first measurements that were taken in the area are also given (these measurements were carried out when the inlets were already open and salt water intrusion might have happened).

8.3.1 Conductivity logs

We see on figure 8.8 the same distribution of conductivity in P11 and P12. In 2005, two zones display higher conductivity values. The first one, around $2.5mTAW$, does not appear anymore later in P12. It is certainly composed of salt water that has flown deeper down the aquifer later. In P11, it remains a small increase in conductivity, certainly due to higher clay content. The second one is located around $-7mTAW$, i.e. the position of the main clay layer. It is why, in 2009, high conductivity values are observed above, because this layer acts as a barrier against vertical flow. In 2010, the conductivity values have decreased by about 30%. We can assume that the decrease is due to the dilution of salt water with fresh water, diffusion and dispersion. It is probable that no new intrusion took place between the two last measurements. Indeed, the inlet is almost filled with sand and very high tides are necessary to cause sea water intrusion. If it was the case, the wells are quite far away from the center of the pond and the intrusion may not be detected in these two wells.

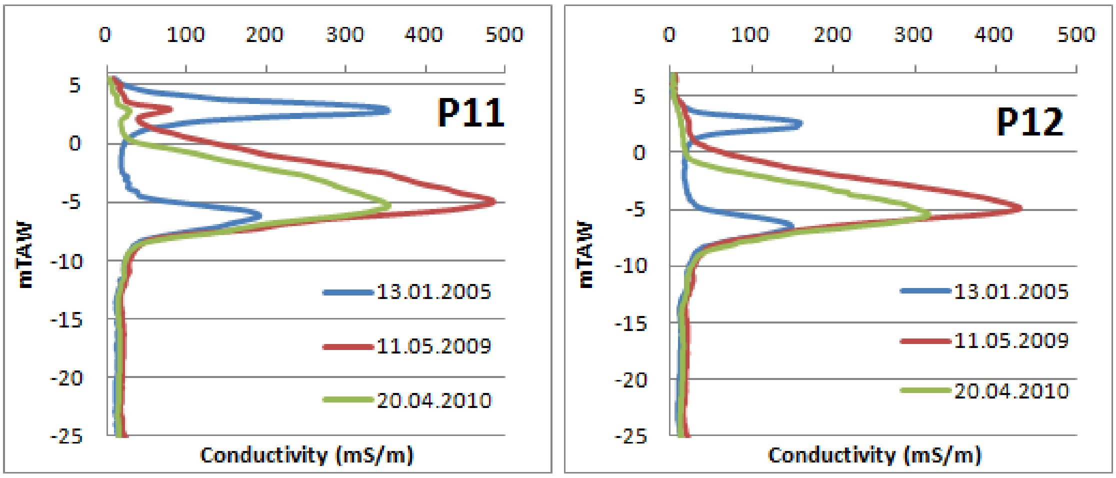

Figure 8.8: Conductivity measurements in P11 and P12.

Conductivity values are systematically higher in P11 than in P12. An explanation is that P12 is further away from the center of the pond, and thus, from the intrusion zone. Salt water that arrives in P12 is more diluted than in P11.

According to figure 8.9, it seems that the sea water intrusion did not reach P14 and P16 in 2005. We only detect higher conductivity values due to the clay layer. For P14, the observed depths are quite different compared to the one given in the drilling data (table 6.1). No salt water is present in the upper part of the aquifer. This observation is quite logical as these wells are located outside the pond and as the horizontal flow is mainly due to the clay. Since the intrusion did not occur at this level, no salt water was observed in these wells. For the same reason, the thickness of the intrusion is thinner than in P11 and P12 in 2009 and 2010.

In P16, the conductivity values are slightly higher than in P14 which could indicate that the intrusion is not the same in the western and eastern part of the pond. A possible explanation is that P16 is closer to the inlet than P14. Again, conductivity values are smaller in the last measurements.

The conductivity distribution in P18 is shown on figure 8.10. In this case, the observations are quite consistent with the lithological description of boreholes. Indeed, the clay layer should be located at around $-4mTAW$ with medium clay content from $-1mTAW$ to $-4mTAW$. That might explain the conductivity values of 2005. In the upper part, salt water is already observed. In 2009, almost all the aquifer above the clay is filled with salt water. The part with medium clay content does not act as a barrier against vertical flow, increased conductivity values are thus found in this zone, too. In 2009, the conductivity values in P18, the closest well to the inlet, are the highest among these five wells. The (high) decrease observed in 2010 confirms that intrusion is probably not occuring anymore.

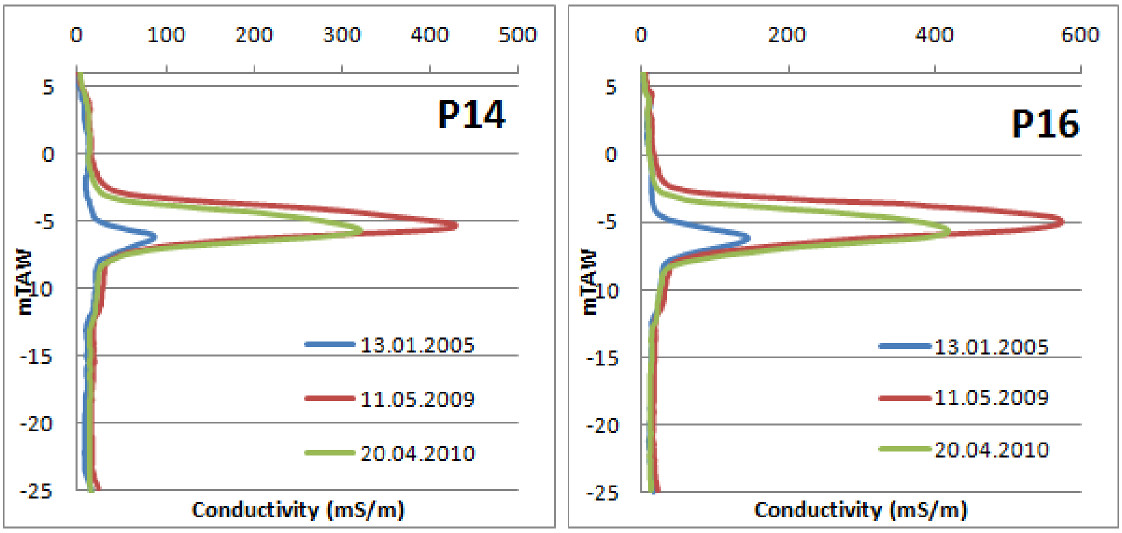

Figure 8.9: Conductivity measurements in P14 and P16.

8.3.2 Water level

Water levels were measured in the wells (F2 corresponds to the deep well and F1 to the shallow well) at the same time EM39 measurements were done, but no correction was made to take salinity into account. However, as explained by Vandenbohede *et al.* (2008a), the water level in these wells is highly dependent on the tides and it is thus difficult to interpret one single measurement. In addition, during the geophysical inversion process, a layer is about $1m$ thick, so we cannot expect a better precision to detect the water level after inversion.

For the detection of the saturated zone, it thus seems sufficient to keep the approximate (Vandenbohede *et al.*, 2006b) elevation to compare it with the inversion results (table 8.1).

8.3.3 Variograms

For each well, variograms were calculated (with VarioWin), based on EM39 conductivity measurements. In addition, a variogram was calculated by putting all the data together. This

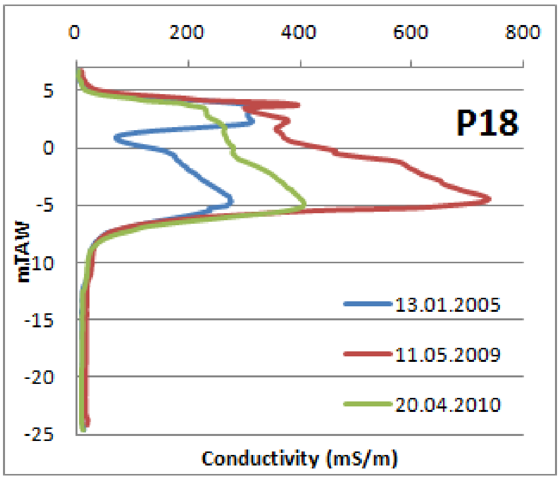

Figure 8.10: Conductivity measurements in P18.

Well	Approximate elevation (mTAW) in F1
P11	4-4.5
P12	
P14	4.5-5 (P13 and P14)
P16	6-6.5 (P15)
P18	4-4.5 (P17)

Table 8.1: Water level.

was done because it seemed more logical to use a general variogram to invert the data when none or several wells were located on the profile. This remark can also be true for profiles with one borehole. Indeed, the variogram of this well is characteristic of punctual statistics and not statistics of the entire field. The results are presented on figure 8.11 and appendix B. Table 8.2 sums up the parameters of the variogram models fitted manually. We can see that all variograms are Gaussian, displaying a high correlation at low distance. P14 and P16 have a smaller range whereas P18 shows more correlation. This feature could already be observed on EM39 measurements, where P18 has a smoother variation than other wells.

Well	Model	Sill	Range
All	Gaussian	0.37	8.41
P11	Gaussian	0.37	8.2
P12	Gaussian	0.37	8.4
P14	Gaussian	0.22	5.94
P16	Gaussian	0.32	6.71
P18	Gaussian	0.63	12.17

Table 8.2: Variogram parameters.

8.4 ERT profiles

8.4.1 Inversion procedure

Six sets of data have been collected and inverted to try to characterize the sea water intrusion in the eastern inlet of the Westhoek nature reserve. As one of the objectives was to show the

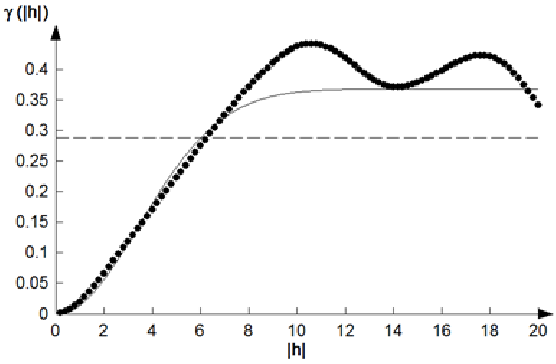

Figure 8.11: Variogram for all the boreholes together.

benefit to use prior information to improve the inversion results, the following scheme was used for each profile.

First, a smoothness constraint inversion was carried out, using the sorted data and the error estimate as explained above. An anisotropy ratio of 4 was chosen after several tries. This ratio was kept for each profile and each type of inversion (it signifies that horizontal ranges are 4 times higher than vertical ranges when the covariance matrix is used to regularize the inversion process). A robust norm was used to inverse all the data sets until the same error level ($\varepsilon^{mean} = 1$). Then, several inversions were done (same parameters) with the covariance matrix as a regularization tool (the assumption of stationarity was discussed in chapter 4), using different prior models as we did for the synthetic benchmarking in chapter 4: the smoothness constraint solution, a homogeneous model equal to $100\,Ohm.m$, and a Gaussian simulation conditioned on borehole data (except for profiles 5 and 6, on which no borehole was located).

For the homogeneous prior model, the value of $100\,Ohm.m$ was chosen for several reasons. Firstly, it was decided to keep a constant value for all the profiles because they are part of the same system. Then, it appears from the synthetic case studies that the prior model plays an important role in depth, where sensitivity is low. According to this fact, it seemed to be a better solution to take a value independent of the surface phenomena (high resistivity value in the dry sands of the dune and low resistivity value of the salt water intrusion). In addition, previous inversions showed that the depth of investigation was almost equal to the thickness of the Quaternary deposits. There were few chances to detect the clay of the Kortrijk formation and to influence the interpretation in this zone badly. Finally, if we observe all the EM39 measurements made since 2004 in depth, they were generally comprised between 7 and $15\,mS/m$ (note that the values were changing from time to time at the same place). It is why it was decided to adopt $10\,mS/m$, which corresponds to $100\,Ohm.m$.

Since it seemed very long and quite redundant for the reader to present all the results obtained for the six profiles, the complete results and discussions of the important points are only presented for profile 1. The observations are the same for the other profiles. For them, only the best results obtained, according to my interpretation, will be shown with, if pertinent, a comparison of the different results with borehole measurements.

Unfortunately, as already said in chapter 4, during the calculation, numerical problems occurred when Gaussian variogram models were used. At the moment, the reason is still not found[1]. It is why other models had to be used for the inversion. A possibility to avoid the problem might be to modify the definition of the Gaussian model

---

[1] We also discussed this point with our colleagues in Bonn who are working on the same code but we still could not find the bug.

Profile	Exponent	Exponent Total
Profile 1	1.5	1.5
Profile 2	1.6	1.5
Profile 3	1.7	1.55
Profile 4	1.65	1.55
Profile 5	1.5	1.5
Profile 6	1.55	1.55

Table 8.3: Gaussian model exponent.

$$\gamma(h) = C\left[1 - e^{-3\left(\frac{h}{a}\right)^2}\right] \tag{8.4}$$

by using an exponent smaller than 2[2]. However, the data set seems to play a role as different exponents had to be used for different profiles, as shown in table 8.3 (Exponent Total corresponds to the case where the general variogram was used to build the covariance matrix). Obviously, it signifies that the covariance matrix is not exactly the one deduced from borehole data, but it was the less worse solution to carry out the inversions.

8.4.2 Conversion into salinity

After inversion, resistivity values may be converted to salinity through Archie's law (equation 2.11). However, we must note that it was not possible to determine the formation factor from borehole measurements directly, because strainers were only located in the bottom or the upper part of the well. The water in the well was therefore not in chemical equilibrium with the water of the aquifer. Since the site is located in a natural reserve, it was forbidden to do a new mechanical drilling. Using manual drilling equipment seemed too difficult because dune sands are too permeable and the pressure would have been too low to keep the hole open. In addition, even with such measurements, it would have been necessary to use homogeneous value laterally for the entire zone. We chose to use a homogeneous value of 3 for the formation factor in agreement with Lebbe (1978)[3].

In addition, it is important to say again that several phenomena are responsible for a decrease in resistivity. In this case, the two main reasons are the salt content and the clay content. Unfortunately, since IP measurements did not yield good results, it was impossible to discriminate the two. Since clay acts as a barrier for the salt water, the two low resistivity bodies will be close to each other. In addition, from EM39 measurements, we can say that salt water fills parts of the pores of the clayey layer. It seems quite sure that the formation factor is different in the less permeable layer; a mistake is thus made when we consider a homogeneous F. To reduce the presence of artifact in the salinity map, it was decided to use a cut-off value of resistivity to calculate a salinity value. From EM39 measurements, a conductivity value below $20\,mS/m$ can be considered as sand filled with fresh water. Therefore, $50\,Ohm.m$ was chosen as the cut-off value. Several relations have been described to link the salinity and conductivity of salt water (see chapter 2). The relation used in this master thesis is the one from previous studies (Van Meir & Lebbe, 2003)

$$TDS = 10F\sigma_b \tag{8.5}$$

where TDS is the total dissolved solid content $[mg/l]$, F is the formation factor and σ_b is the bulk conductivity of the soil $[mS/m]$. No temperature correction was taken into account since

---

[2] Note that the resulting variogram models are only slightly different from a true Gaussian model and is still within error bound of the experimental variogram.

[3] Variations about 10% are possible.

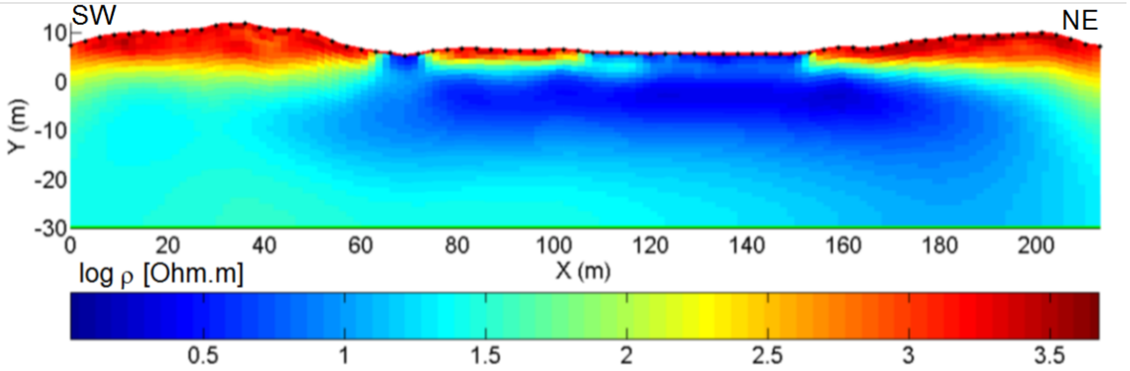

Figure 8.12: Smoothness constraint solution for profile 1 (scale in $\log \rho\,[Ohm.m]$).

the groundwater temperature is around $9 - 11°C$ (Vandenbohede *et al.*, 2008a)

According to the remarks above[4], it is possible to produce a TDS content map in the pond. We again insist that these values are just orders of magnitude to highlight the large scale trends in salt water distribution.

8.4.3 Profile 1

Inversion process. Below, only the features due to the inversion process will be discussed. Geological and hydrogeological interpretations are going to be explained later in section **interpretation**.

Figure 8.12 shows the results of inversion with the traditional smoothness constraint solution. When we first look this figure, we can think that this solution seems quite satisfying. Expected features are observed and the salt water intrusion is detected. However, we also see that the resistivity remains quite low below $-10m$ whereas we know by EM39 measurements that the intrusion is stopped by a clayey layer. If we look at figure 8.17, we see that the vertical distribution of ERT conductivity is very different from the one observed in P11 with EM39 measurements. The maximum conductivity value is underestimated and the transitions are too smooth as a value of about 20 to $30\,Ohm.m$ is found by inversion in depth and only $10\,Ohm.m$ for the intrusion. Clearly, the contrast is partly erased by the smoothness regularization.

The same features could be observed in other wells and other profiles (figure 8.23 and figure 8.27). Only P18 displayed something different (figure 8.18) because the EM39 measurements are smoother in this well, and the smoothness constraint solution performs well in the upper part of the aquifer. Below $-8mTAW$, the other solutions become more satisfying. It is the only borehole where inverted values overestimate EM39 measurements.

Then, the data set was inverted with the covariance matrix as a regularization operator. The variogram parameters determined from all well data merged together was used since the profile ran through 3 wells. Figure 8.13 gives the results for the inversion with the smoothness constraint solution used as a prior model. The observations made in the synthetic cases can also be applied to this real case. Indeed, this solution is very close to the smoothness constraint one. The explanation is the same: the constraint on the prior model is too strong and the solution cannot move away from it. On figure 8.17, we see that the corresponding curves overlays the one of the smoothness constraint solution. For other profiles, this solution sometimes led to a slight improvement. However, this improvement does not justify the time necessary to obtain it, because the solution remains quite different from EM39 measurements.

---

[4] In addition, resistivity values obtained after inversion contain some deviations from the true values.

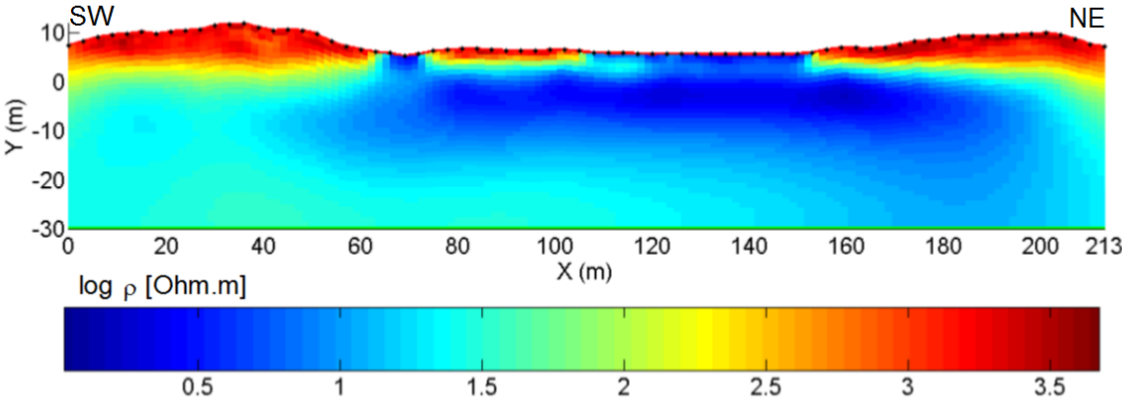

Figure 8.13: Inversion with the smoothness constraint solution as a prior model for profile 1 (scale in $\log \rho \, [Ohm.m]$).

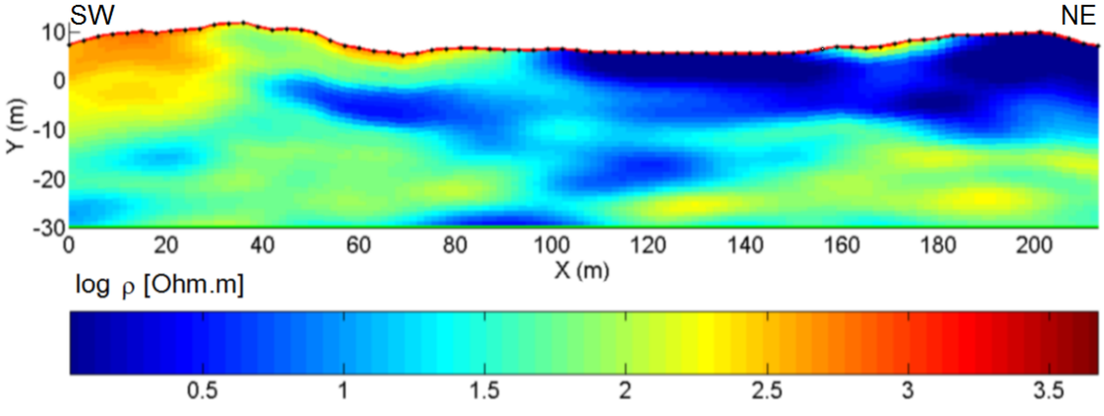

Figure 8.14: Gaussian simulation used as a prior model (scale in $\log \rho \, [Ohm.m]$).

The smoothness constraint solution is clearly not efficient as a prior model, because it does not allow to take full advantage of the geostatistical regularization. As stated earlier, two additional prior models were tested. First, a Gaussian simulation, conditioned by EM39 measurements was used as a prior model and second a homogeneous prior model was tested. Figure 8.14 represents the resistivity distribution of the Gaussian simulation used as a prior model. At abscissa of the boreholes (57m, 64m and 167m), it respects the values imposed. Around the wells, the values are correlated due to the variogram parameters used to build this simulation. Elsewhere, the resistivity values are only one possibility inside a probability density function.

After inversion, we obtained the section of figure 8.15. Combined with figure 8.17, it gives both advantages and disadvantages of this type of prior model directly. Indeed, around the wells, the conductivity distribution is well respected. However, the imposed values are not conserved, even if the prior model is also used as a starting model. This is due to the fact that nothing in the inversion process says that these parameters have to remain equal to the prior. They just guide the inversion to a more likely solution around the well. It signifies that the improvement is real around the well, but limited in the middle of the pond, where no borehole is available.

Disadvantages are mainly visible at depth. The role of the prior model when the sensitivity is low (see chapter 4 and section 8.5) was explained for the synthetic cases. The same is true here, below $-10m$, the inverted model is very close to the prior model. The problem is that a Gaussian simulation cannot be considered as a good solution. Indeed, if another simulation (but with the same parameters) had been used, the inverted solution would have completely changed in depth. To avoid this problem, a possibility is to carry out an ensemble of inversions with

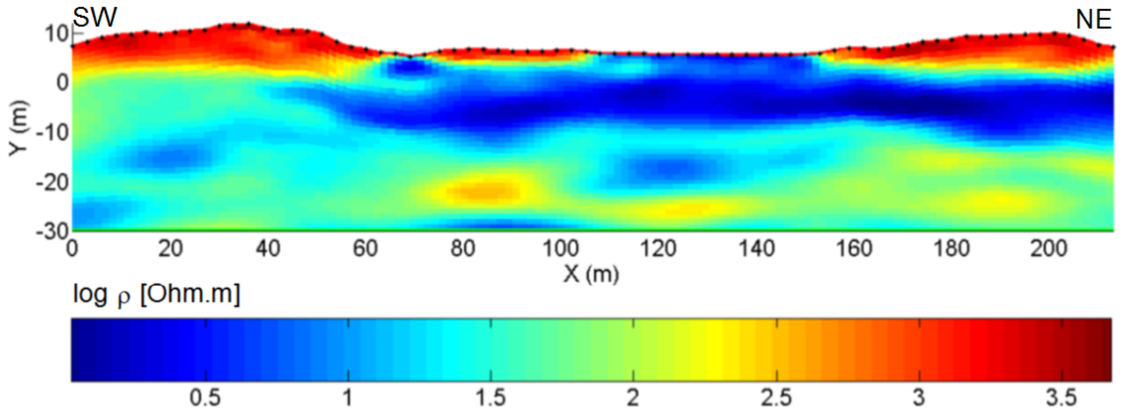

Figure 8.15: Inversion with a Gaussian simulation as a prior model (scale in $\log \rho \, [Ohm.m]$).

different simulations as a prior model. This was done for profile 3 (which has fewer parameters to be calculated, see section 8.4.7) with 50 simulations.

However, it costs a lot of time to obtain. For example, the grid used to invert data of profile 3 was composed of 3710 elements. The calculation time for 50 simulations was equal to 40 hours with a calculation station operating in 64bits with four processors. In addition, we have to take into account the time to prepare all the inversion files (one file for each different prior) and to collect the results. As explained, this process was tested for a short profile. Profiles 1, 2 and 4 have 5355 elements. The calculation time would be increased for these profiles. We understand that such a calculation time becomes much too important for engineering deterministic applications. However, this approach could be of interest to provide several scenario of contamination for example (stochastic approach). In addition, it is necessary to have a borehole on the profile to carry out such an inversion. It is why it was decided to interpret the results coming from inversions with a homogeneous prior model (figure 8.16). Figure 8.17 (and equivalent for other wells) shows that this solution is always better than the smoothness constraint solution, whereas it is slightly worse around boreholes than the solution with a Gaussian simulation as a prior model. Elsewhere, both solutions seem quite equivalent, except in depth, where a lot of simulations are necessary to obtain a solution similar to the one with a homogeneous prior model.

One could argue that EM39 measurements are being out of the inversion process (although they are used indirectly in variograms). At the moment, the possibility to impose resistivity values in CRTOMO is not implemented yet. It could be a very interesting perspective to develop this characteristic, as in RES2DINV. It would allow us to use the covariance matrix regularization and borehole data simultaneously during inversion with a homogeneous prior model. The calculation of a lot of simulations would become unnecessary. A problem when adding such a constraint is the effect of scale between EM39 and ERT measurements. Indeed, the volume investigated is different. The tests carried out in this master thesis were not successful. More time was necessary to change the code by applying a radius of influence (close to the horizontal range) of the imposed value and a certain degree of freedom for the inversion process.

Interpretation. All interpretations are going to be analyzed on results obtained with the same homogeneous prior model and the same variogram parameters (range of $8.4m$ and sill equal to 1), and on the conversion into TDS content. First profiles parallel to the sea (1, 6 and 4 with first electrode located to the south-west) will be presented and then profiles perpendicular to the sea (2, 5 and 3 with first electrode located to the south-east). When a depth is given, it will always refer to the vertical scale of the corresponding figure, given in $mTAW$. The orientation of each profile is shown on figure 7.6.

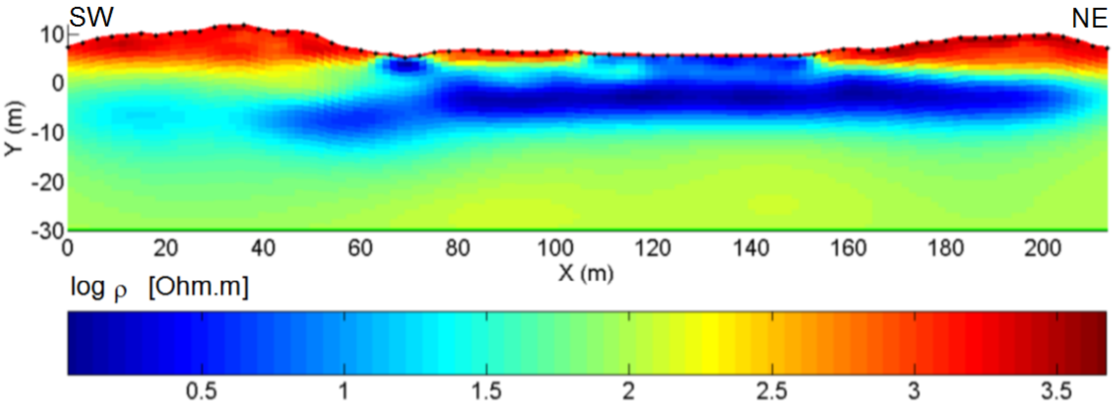

Figure 8.16: Inversion with a homogeneous prior model for profile 1 (scale in $\log \rho\,[Ohm.m]$).

Figure 8.16 shows several different resistivity zones, according to depth. First, we have a zone with high resistivity values (from about $10^{2.7} = 500\,Ohm.m$ up to more than $3000\,Ohm.m$), corresponding to the unsaturated dune sand near the surface. Since the quartz is not a good conductor, the current does not flow easily through this zone. This feature was already observed on the field: before the beginning of the measurements, contact resistance was assessed for each electrode to verify that the connection was good. For the electrodes placed in the dunes, this contact resistance was always higher than for electrodes located in the infiltration pond. A decrease in resistivity is observed deeper and corresponds to the saturated zone (dune aquifer). If we trust the water level measured in 2005, it lies around 4 to $4.5mTAW$ which corresponds to the transition from red to yellow in the figures. So, in this case, it seems that ERT is able to detect the water level approximately, located at resistivity values around 200 and $300\,Ohm.m$ (2.3 and 2.5 in logarithmic values).

Another zone that appears clearly is the zone located below $-12mTAW$. It consists of medium to coarse sands with shell debris (see chapter 6). Resistivity values are around $100\,Ohm.m$ (value chosen for the prior model), ranging from 50 to $160\,Ohm.m$. Below $-30mTAW$, we should find the Ypresian clay, but the depth of investigation is not great enough to detect the decrease in resistivity.

Between these two zones, we found the low resistivity zone (inferior to $3\,Ohm.m$) corresponding to the salt water that infiltrated the pond. An interesting observation can be made on the left part of the section (from abscissa 0 to $40m$). Between -5 and $-10mTAW$, we find a layer with resistivity value ranging from 15 to $30\,Ohm.m$. This is too low for sand with fresh water and too high for sand filled with salt water. This layer was described previously as having a higher content in fine materials (clay). This layer acts as a barrier to the vertical flow, engendering a lateral flow. This layer is certainly present in all the section; but, in this particular zone, the aquifer is not polluted by salt water, we can thus detect it.

The intrusion itself is detected between $40m$ and the end of the profile. The minimum value of resistivity is located at a depth of $-4mTAW$, above the clay layer. In the neighborhood of P11 and P12 (around abscissa $60m$), the intrusion seems to be slightly deeper as well as the clay layer. This is confirmed by the EM39 measurements (figure 8.8) where the clay is detected at $-7mTAW$. The clay layer is not a regular horizontal layer, but it is composed of several lenses, each overlapping the other. On figure 8.17, it seems that there is a small difference between the depth of the maximum from ERT and the EM39 measurements. We saw in the modeling part (chapter 7) that it could happen due to difficulty to notice a difference between salt water and clay when they are superimposed or juxtaposed. In addition, grid-cells are $1m$ thick, so we cannot expect a better precision. The results thus seem quite satisfying. If the intrusion goes

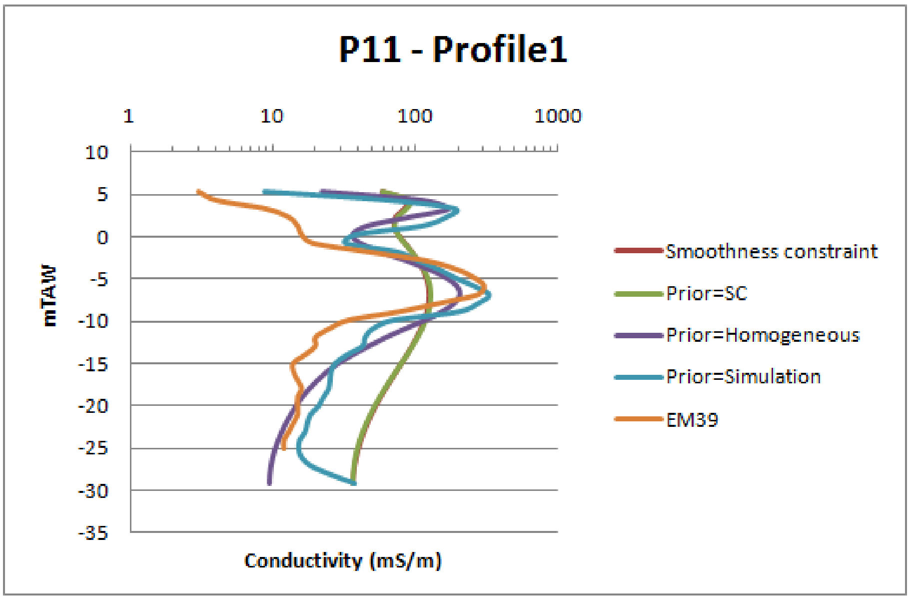

Figure 8.17: Comparison with borehole measurements made in P11.

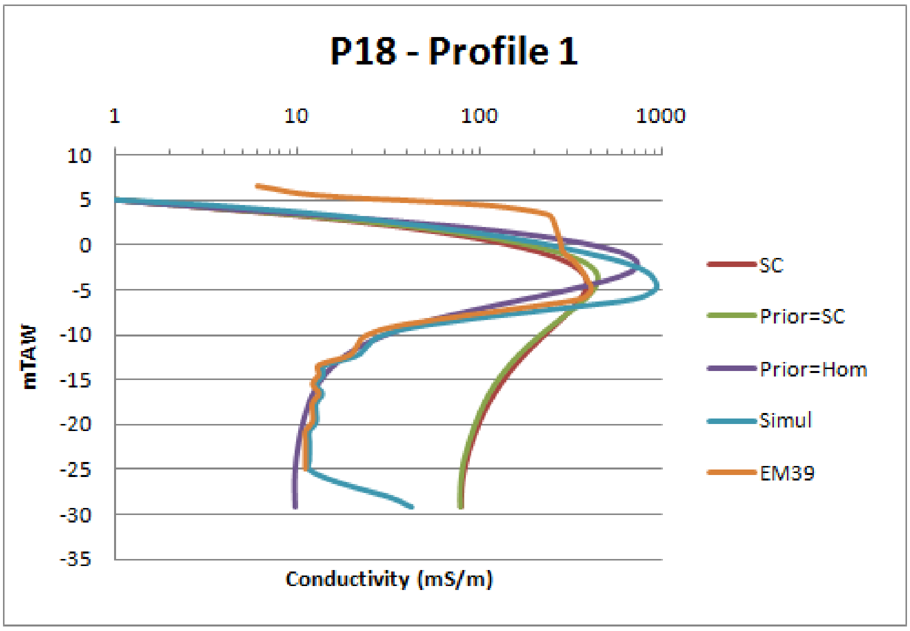

Figure 8.18: Comparison with borehole measurements made in P18.

further down the dune to the east (right side of the section), it is just because the entry of the pond is located around abscissa $120m$.

Resistivity values remain quite low near the surface in the pond, even if new intrusions are certainly very rare (only during spring tide near the spring equinox). A possibility is that a new intrusion occurred during the week before the measurements (end of February)[5]. It could have seemed more curious to find low resistivity values around abscissa $70m$, because this part is a long way from the entrance of the pond, and the probability is very low that a new intrusion reaches this location. On figure 8.8, we see at $3mTAW$ an increase in conductivity in the measurements from 2005 to 2010. This could correspond to a layer with higher clay content

---

[5] At the time of writing, the answer from Agency for Maritime Services and Coast- Division COAST about the tides in De Panne is still waited.

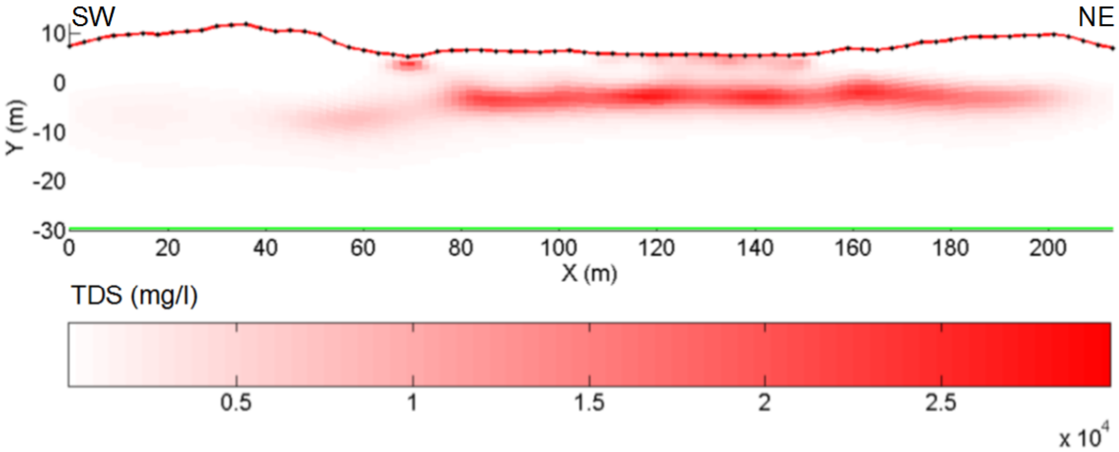

Figure 8.19: TDS content (mg/l) for profile 1.

described in Lebbe (1978). In some places, this layer (less continuous than the other one) could have a low hydraulic conductivity, acting also as a barrier to the vertical flow. The presence of salt water is no more detected in P11 in 2010 (the increase is only due to the clay content). However, at this depth, there is an increase in the inverted model(s) (figure 8.17). We can imagine that there remains some salt water at around 70m; during the inversion process, the correlation length given by the horizontal range also tends to increase the conductivity value in P11.

If we compute the variograms of the inverted model, we obtain a vertical range very close to the real one (between 7.5 and 9), which shows the faculty of the covariance matrix to regularize the solution vertically. The horizontal range is much bigger (around 70m), this parameter was thus underestimated. We saw previously that it is not a big issue. Similar observations are true for other profiles.

The TDS content section (figure 8.19) aims at highlighting the salt water intrusion compared to other variations in resistivity. The maximum value (26900 mg/l) is detected above the semi-permeable layer. The worldwide mean value for sea water is 35000 mg/l, but the North Sea has a salt content of about 27000 mg/l (Vandenbohede *et al.*, 2008b). According to these results, it seems that the salt concentration is still close to the one of sea water. We see that the salt content is smaller on the sides of the intrusions, where the infiltrated water is slightly older and is maybe more diluted. However, the comparison with EM39 shows that the maximum inverted conductivity value underestimate the measured one with EM39 in P11 and P12. A loss of resolution is also possible, but we will see in section 8.5 that the diagonal elements of the resolution matrix have similar values for all the intrusion as the depths are quite similar.

8.4.4 Profile 6

Profile 6 is located in the middle of the pond, parallel to profile 1 but further from the sea, and similar features can be observed on both of them. There are no wells on this profile to correlate the features. Results are shown on figure 8.20.

Again, we distinctly detect the unsaturated sands of the dunes and the transition at the water level. The shape of the intrusion is almost the same as in profile 1, with salt water going under the dunes in the eastern direction (right part of the section). Around abscissa 70 to 90m, we see that the resistivity value is low just behind the surface, then an increase is observed up to about 100 $Ohm.m$. We interpret again the presence of a clay lens around 2m that traps some salt water. At the same abscissa, the salt water intrusion appears to be slightly deeper. Since clay

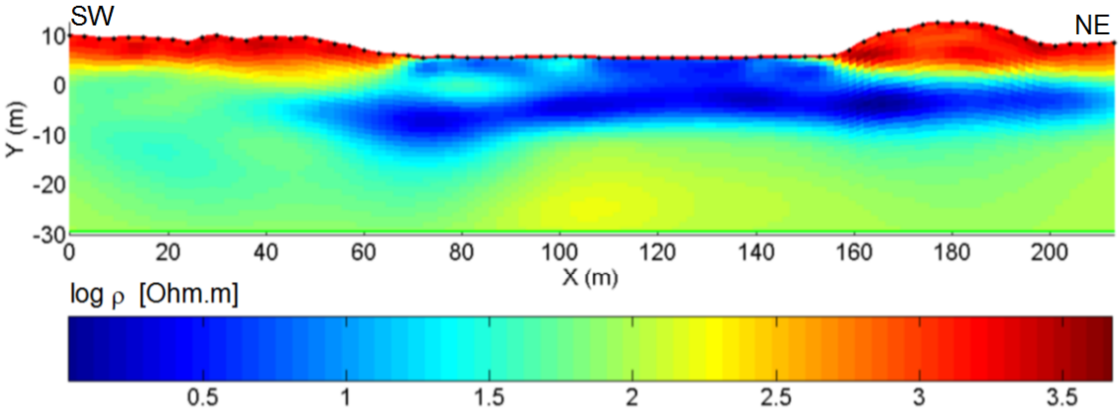

Figure 8.20: Inversion with a homogeneous prior model for profile 6 (scale in $\log \rho \, [Ohm.m]$).

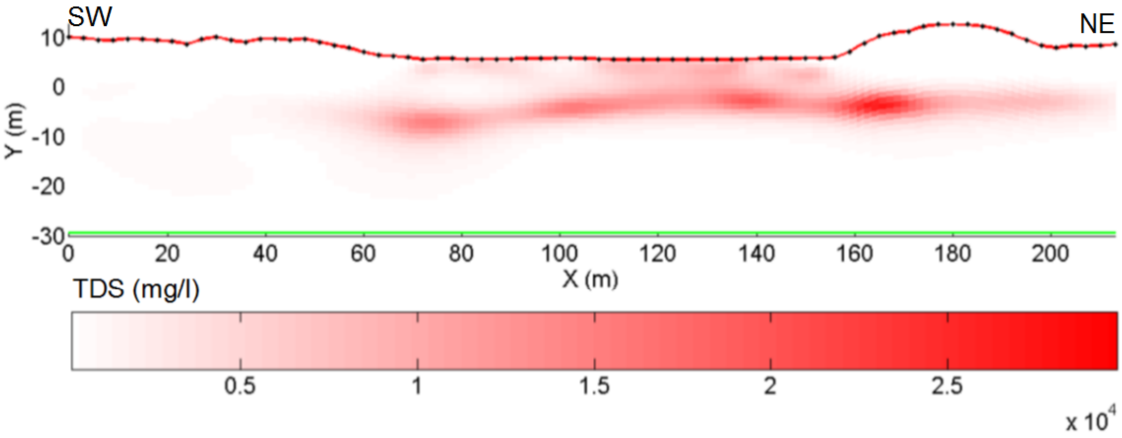

Figure 8.21: TDS content (mg/l) for profile 6.

lenses that composed this semi-permeable layer are not regular, at some locations, "holes" may exist between two lenses where hydraulic conductivity is slightly enlarged. If it is the case, salt water can be found deeper down the aquifer as observed in the section. There are few chances to explain it by an artifact of inversion. Indeed, the regularization should tend to a higher horizontal correlation and not to variations in depth of a same structure. This characteristic must originate from data information. In this section, the clayey layer is not clearly distinguished in the south-west direction. The same features were observable when the Wenner-Schlumberger data set was inverted. Unfortunately, no borehole was available to compare the two solutions.

The TDS content (figure 8.21) is globally smaller than in profile 1. It is quite logical as profile 6 is located further from the sea. The maximum value is equal to $26850 \, mg/l$. It might appear quite strange to observe several kinds of plumes and not a continuous intrusion (it was also observed on profile 1, even if it was less obvious). This phenomenon could be due to the precision obtained with our measurements, but the level of noise is the same as for profile 1. A natural explanation is also possible. In 2004, the dynamics of intrusion was such that the sea entered the pond once a month. After 2005, silting up of the inlet began and the number of intrusions decreased, the same can certainly be said about the surface concerned with infiltration. Thus, the intrusion scheme is not continuous but episodic; it could be reflected in the intrusion shape.

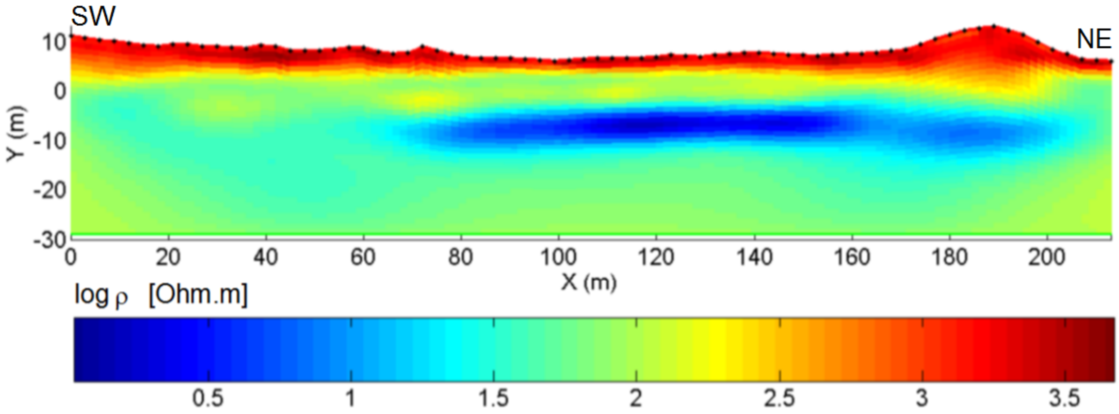

Figure 8.22: Inversion with a homogeneous prior model for profile 4 (scale in $\log \rho\,[Ohm.m]$).

8.4.5 Profile 4

Figure 8.22 shows the result for profile 4. It is also parallel to the sea, but all the electrodes are located in the dune area, it is located along the south-east limit of the pond. So, resistivity values above $1000\,Ohm.m$ are present everywhere on the surface. No intrusions from the surface can occur. The 10 first meters below the surface are not polluted by salt water and we can detect features in this zone more precisely than in other profiles.

For example, in the middle of the profile (abscissa 60 to $120m$), there is an alternation of layers with resistivity values above and under $100\,Ohm.m$, that we link to the clay content of the sand. A higher clay content is expected around $+2mTAW$ (small lenses responsible for salt water near the surface in the infiltration pond) and then around $-7mTAW$ (main clayey layer). It seems that the resistivity value in depth is slightly smaller than observed in profiles 1 and 6. The intrusion originates from the lateral flow coming from the center of the pond. The minimum resistivity is on the top of the semi-permeable clay layer. Under the dunes on the right part of the section (north-east), the intrusion seems less pronounced than in other parallel sections. In the southwestern direction, there is a small decrease in resistivity around $-10mTAW$, which could be due to the clay content.

Figure 8.23 displays a comparison between different inverted resistivity values and EM39 measurements for profile 4. It appears that the maximum in conductivity is found deeper with ERT (except with a Gaussian simulation used as a prior model) than with EM39 in this case. We could observe the same thing in the modeling section. The smallest resistivity value was detected at the limit between the clayey layer and the clean sand. The vertical resolution of the EM39 device is better, it can detect more precisely the variations. This profile is a good example to show that covariance matrix regularization was able to improve the results, even with the smoothness constraint solution as a prior model. Indeed, the corresponding curve is not superimposed to the one of the smoothness constraint solution, the given correlation length enables to find a vertical distribution closer to the real one. However, this solution is still worse than the one with a homogeneous prior model. The accordance with EM39 measurements is also very good for the Gaussian simulation used as a prior model. For this profile, it could be interesting to carry out 50 simulations.

The conversion into TDS content (figure 8.24) shows that the maximum value is smaller than for profiles in the middle of the pond ($18850\,mg/l$). This can be easily understood as the salt water that has flowed towards the dune has been infiltrated for a longer period than the water still under the infiltration zone. Diffusion and dispersion have played their roles to decrease the maximum salt content.

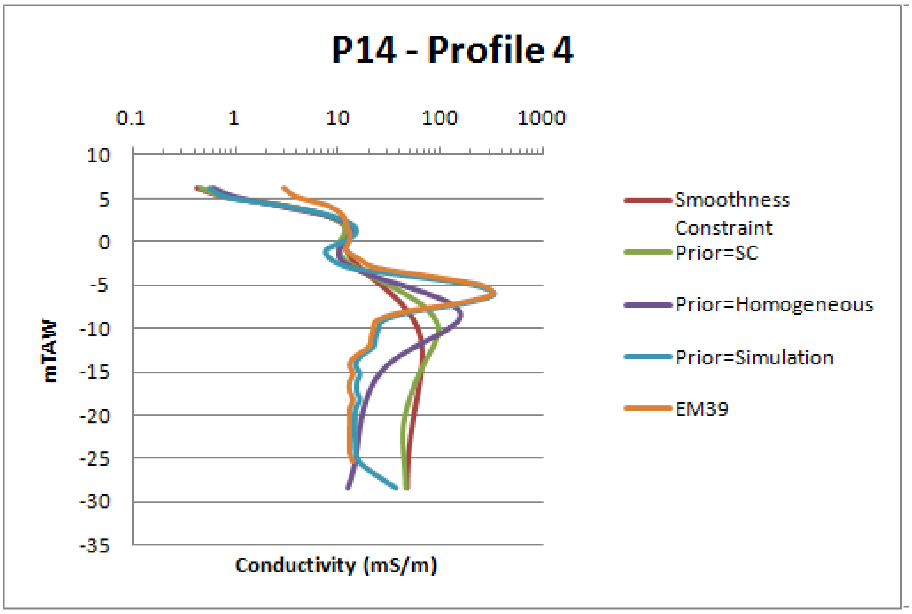

Figure 8.23: Comparison with borehole measurements made in P14.

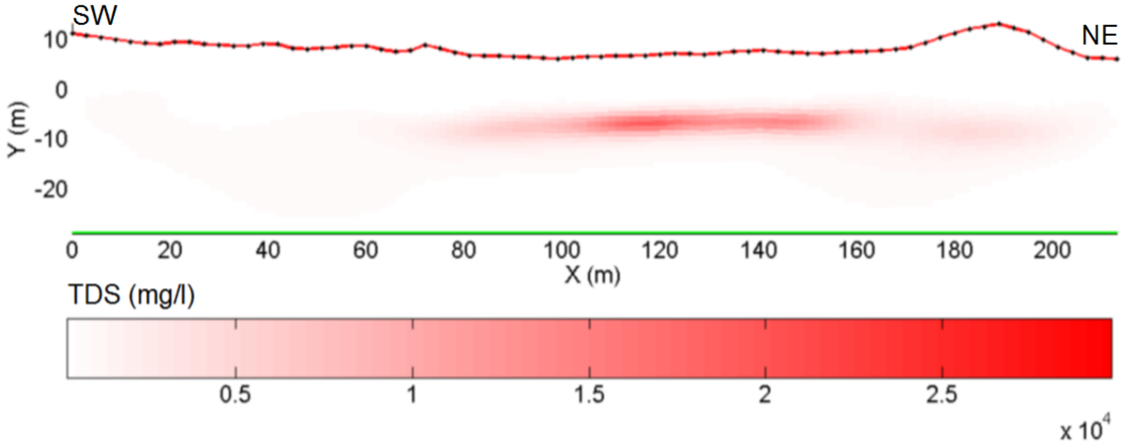

Figure 8.24: TDS content (mg/l) for profile 4.

To conclude with profiles parallel to the sea, we can say that the lateral flow led to find salt water at more than $40m$ under the dunes in the eastern direction (right part of the sections). On the western part, this phenomenon is more limited, because the limit of the pond is further from the entrance of the inlet. This lateral flow also acts landwards in the direction of the water catchment. Perpendicular profiles are going to show to what extent.

8.4.6 Profile 2

Profile 2 is located on the eastern part of the pond. Since the results were very similar for profile 5, the latter will not be shown (the reader can find them in appendix C). Then, we will move westwards with profile 3.

Figure 8.25 presents the results of inversion with a homogeneous prior model. Since this profile went on the beach, we observe a new zone on the profile. Abscissa $150m$ was the location of the bridge separating the dune area and the beach. Between this bridge and the end of the profile, electrodes were placed in the sands of the beach, during low tide. The low resistivity zone

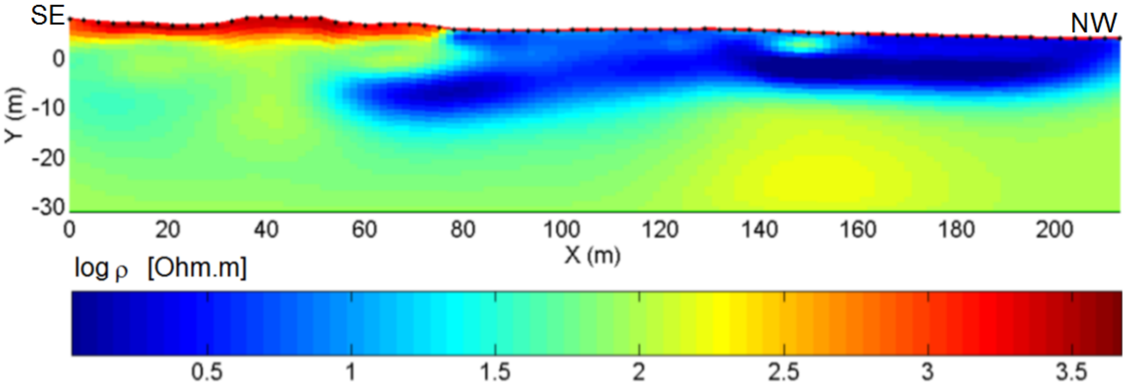

Figure 8.25: Inversion with a homogeneous prior model for profile 2 (scale in $\log \rho \, [Ohm.m]$).

is due to the salt water lens above fresh water in dynamic equilibrium. If we compare the depth of this zone with previous work (Lebbe, 1999 ; Vandenbohede & Lebbe, 2006a), we see that the depths are not the same. Indeed, the transition between salt and brackish water (dark to clear blue) is around $-5mTAW$ whereas it should be at about $-10mTAW$, according to log normal measurements. Identically, the transition between brackish and fresh water is located around $-9mTAW$, whereas it should be 4 or $5m$ deeper. Since covariance matrix regularization was applied to this section, with variogram parameters deduced from boreholes in the dune area, it is obvious that these parameters cannot represent the distribution of salt water under the beach due to the tides. The mechanisms responsible for both types of intrusion are different and so is the distribution of salt water. If we can assume the variograms to be quite correct in the pond, it is not the case on the beach and it leads to mistakes when interpreting the salt water lens since the vertical variations are in part controlled by the variogram parameters (as shown by our synthetic benchmark).

It would be better to study this lens separately, or to impose different variogram parameters on this zone[6]. It is important to avoid the misinterpretation of the transitions between salt and fresh water at the end of the profile (abscissa $200m$). If this transition is going upwards, it is because the sensitivity is low in this zone and not because fresh water flows upwards and flows out on the beach. Indeed, data was also taken further on the beach (one more roll-along, see chapter 7) and the same distribution of salt water was detected. The fresh water discharge is therefore situated further, near the low tide line (approximately $400m$ away from the bridge position) (Vandenbohede *et al.*, 2008b).

The bridge seems to produce an effect on the resistivity distribution. Indeed, if we have low resistivity values on the beach and in the pond near the surface, it should be quite logical to see also low resistivity values under the bridge. However, there is an increase in resistivity. The main reason is likely to be the presence of concrete in the structure of the bridge (pillar and footing, see figure 8.26). In addition, the dyke is very close to the profile and could also play a role (3D effect). However, under the bridge, it seems that the dyke was removed; but stone revetments were placed to protect the entrance of the inlet from erosion. The top of the revetments was covered by a layer of sand, $1m$ thick (Verwaest *et al.*, 2005). The very low resistivity value observed below $0mTAW$ at this location is also certainly an effect of the bridge, because there is no hydrogeological reason to find so high values at this place. We observe a direct connection between the salt water that infiltrated the pond and the salt water lens under the beach. This is due to the lateral flow coming from the pond towards the sea; it brings salt water out of the dune area.

---

[6] The algorithm is built to deal with several zones, however a solution has to be found to ensure some continuity between them.

Figure 8.26: Structure of the bridge.

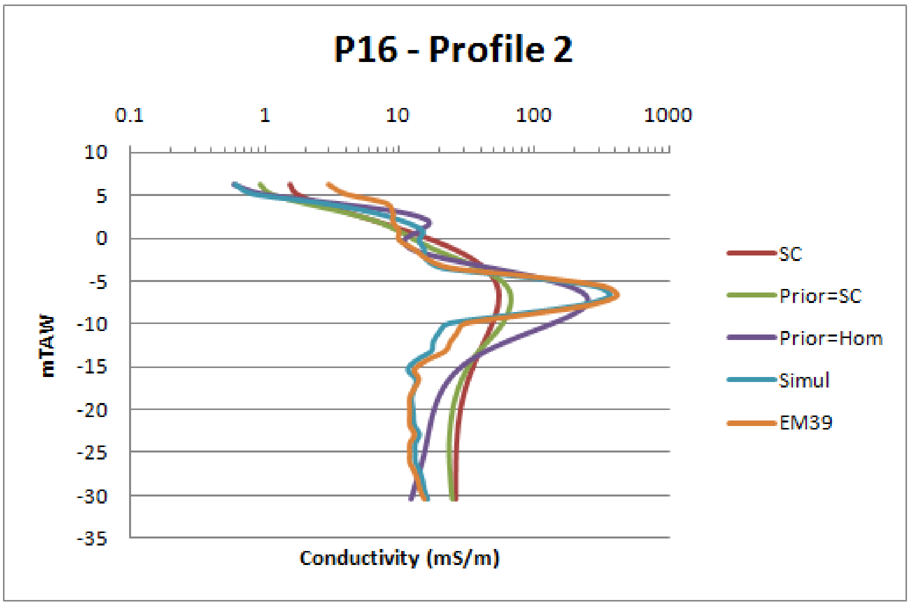

Figure 8.27: Comparison with borehole measurements made in P16.

In the infiltration pond, we see that the salt water intrusion fills almost all the surface of the pond, above the semi-permeable layer. The depth of the minimum resistivity value is found slightly deeper in P16 area. On figure 8.27, we see that the vertical variation measured with the EM39 device is quite well found in the inverted ERT model. We also see that between -10 and $-15mTAW$, the conductivity is slightly higher than deeper down the aquifer. It could be due to a slight vertical movement of the intrusion or the presence of the clay layer deeper down. Around abscissa $40m$ at $-10mTAW$, it seems that the clay layer is missing, or at least that the clay content is lower because resistivity values are around $100\,Ohm.m$. This could be the place where salt water flows deeper down the aquifer and goes back towards the sea due to the main gradient. Indeed, due to the water catchment, there is a water divide in the dune area located at about $350-400m$ from the dyke. Water in the dune area close to the sea should flow in this direction as it was modeled by Vandenbohede *et al.* (2008b).

Concerning the TDS content (figure 8.28), we see a higher value than the TDS content of the North Sea in the lens under the beach (more than $30000\,mg/l$). We know that the uncertainty is quite high due to the formation factor, the conversion law, the statistics used, the level of noise, etc.

In the pond, it was surprising to find higher salt content in a zone further from the entry of the pond (abscissa $80m$). However, salt water infiltrated just after the building of the inlets. At this time, sea intrusions were frequent. Later, intrusions became less common and the volume of new intrusions was smaller. It results in a higher dilution with the fresh water and a lower salt

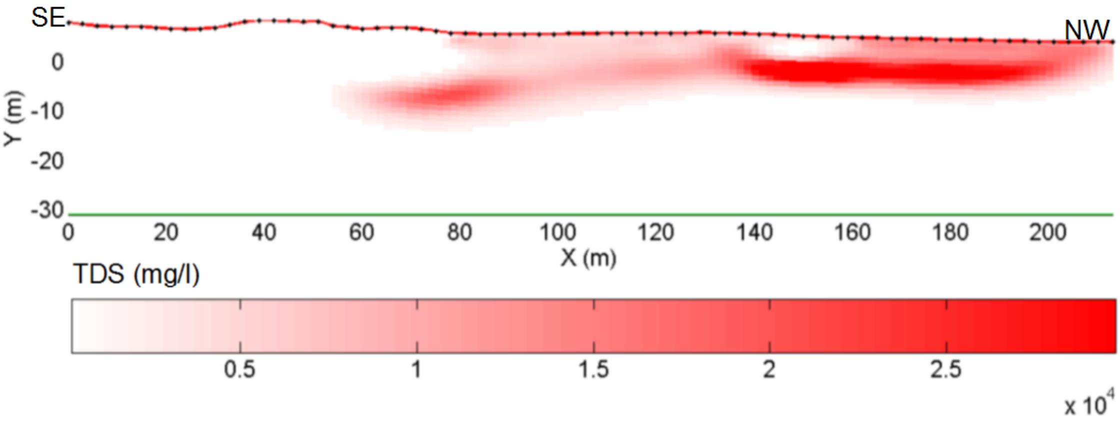

Figure 8.28: TDS content (mg/l) for profile 2.

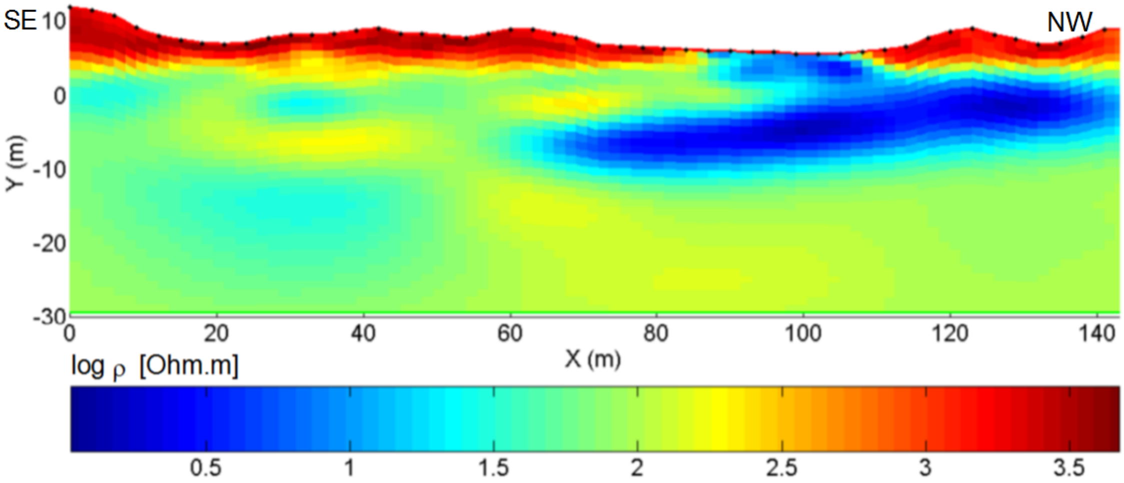

Figure 8.29: Inversion with a homogeneous prior model for profile 3 (scale in $\log \rho\,[Ohm.m]$).

content. This feature is confirmed when we compare the intersections of profile 2 with profile 4 (abscissa respectively $67m$ and $123m$), and profile 6 (abscissa respectively $88.5m$ and $115.5m$). If the salt content is globally higher in profile 6, at this particular place, the TDS content is higher in profile 4. It is thus very important to view this salt water intrusion in a 3D context and to avoid drawing simple and general trends.

8.4.7 Profile 3

Profile 3 is parallel to profiles 2 and 5, but has its both ends in the dune, towards the southwest. The inversion results are presented on figure 8.29 and the conversion into TDS content on figure 8.30. The observations are quite similar to other profiles. Near the surface, the sands of the dunes are unsaturated and resistivity values are high (more than $1000\,Ohm.m$). The water level is detected at about $4-5mTAW$. This is in accordance with water level measurements made on the site previously.

On the southeastern part of the profile (left part of the section), the dune aquifer seems to be slightly more heterogeneous. There is an alternation of clean sand (around $150\,Ohm.m$) and sand with higher clay content or clay lenses (around $30\,Ohm.m$). The semi-permeable layer may be less continuous in this zone and the intrusion could flow deeper down the aquifer if it reaches a more permeable zone.

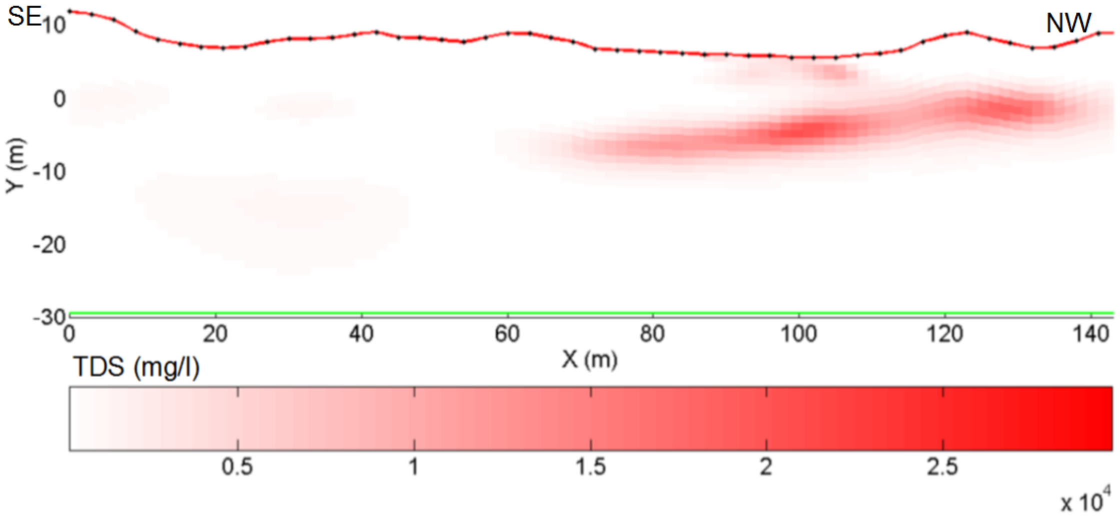

Figure 8.30: TDS content (mg/l) for profile 3.

On figure 8.30, we see that the salt content is lower in this part of the pond than anywhere else. The maximum value of TDS content is $20000\,mg/l$. It is quite logical as this part is further from the entrance of the inlet. Again, we see the lateral flow of salt water towards the sea. We found the intrusion shallower under the dunes in the right part than under the pond. This could be explained by the heterogeneity of the clay layer.

As explained before, 50 inversions were carried out with Gaussian simulations as prior models. The ensemble is analyzed in terms of the mean of all the inversions, and the distribution becomes less random in depth (figure 8.31). Indeed, each parameter in the low sensitivity zone is now the mean of the density probability function. Far away from conditioning data, the parameters correspond to the mean of the conditioning data distribution. In this case, we see that the intrusion around the well (abscissa $72m$) is disconnected from the rest of the intrusion, which is maybe not the best solution. In addition the maximum conductivity value ($1\,Ohm.m = 1000\,mS/m$) is much bigger than the measured one with EM39 (figure 8.9). It also seems that the horizontal range is of importance, because the influence of the borehole is about $30m$. It means that such a simulation could cause some problems when the horizontal range is unknown. It would not be an improvement if borehole imposed values influenced too much parameters in the middle or outside the pond. Finally, it signifies that the mean of all inversions based on simulations is closer and not always better to a solution which would use a homogeneous prior model (see figure 8.29).

8.4.8 Correlation between profiles

We have seen that ERT was able to image correctly the intrusion, to contribute to a better hydrogeological interpretation of the system, and to give a quantitative approach to determine the TDS content. To confirm the aptitude of 2D ERT to give reliable results in a moderate 3D context, a comparison between the vertical distribution of conductivity at some intersections of profiles perpendicular and parallel to the sea was carried out. The abscissae of intersections are given in table 8.4[7]. In addition, a qualitative appreciation is given. This appreciation is based on a visual comparison of the results; so, it is subjective. Figure 8.32 shows two examples of correlation between profiles.

---

[7] The intersection of profile 4 and profile 5 is located at the beginning of profile 5, the sensitivity is thus low even at small depth and it can explain a bad correlation.

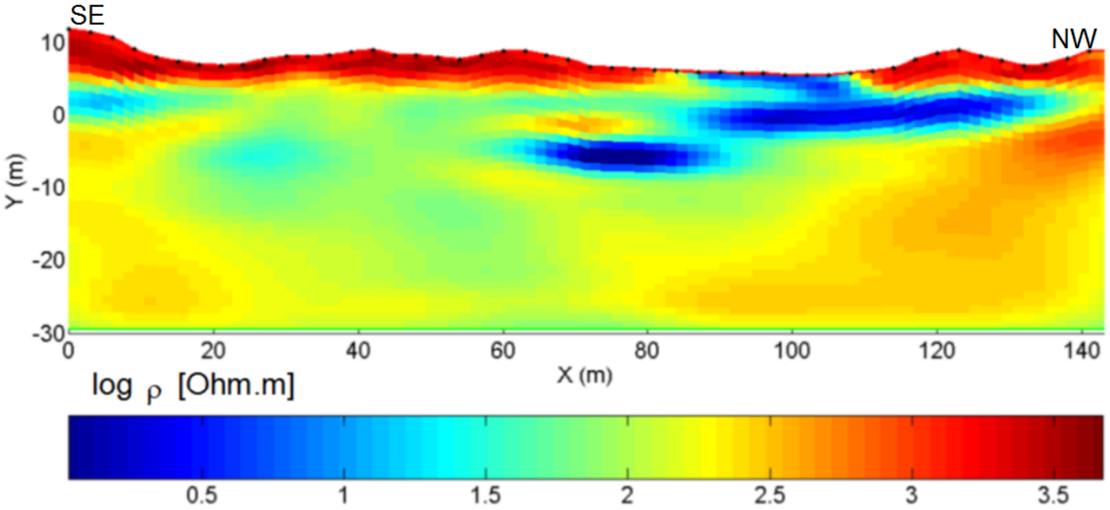

Figure 8.31: Mean of 50 solutions using a Gaussian simulations as a prior model for profile 3 (scale in $\log \rho \, [Ohm.m]$).

Couple of profiles	Abscissa of intersection (first) in m	Abscissa of intersection (second) in m	Quality of correlation	
			Depth of maximum	Value of maximum
P1 - P2	123	105	++	-
P1 - P5	106.5	43.5	++	++
P1 - P3	83	112.5	++	-
P6 - P2	115.5	88.5	+	++
P6 - P5	101	30	+	+
P6 - P3	78	96	+	+
P4 - P2	123	67	++	+
(P4 - P5)	101.5	7	++	-
P4 - P3	81	72	-	+

Table 8.4: Intersections between profiles and quality of correlation (++=excellent, +=good, -=bad).

On the whole, the results are satisfactory. Obviously, there are some differences when the results are coming from different profiles, the maximum conductivity value or its depth is sometimes a little bit different. The maximum conductivity values are quite different in the intersections between profiles 1 and 2 or profiles 1 and 3. Elsewhere, the results are quite similar. The depth of maximum conductivity is almost always the same, except in P14 (intersection of profiles 3 and 4).

8.5 Image appraisal tools

To analyze the resolution obtained for the investigated zone in our ERT images, different popular operators were calculated. It was done only for profile 1 since all the profiles are quite similar (the sensitivity matrix was available for each profile, it was easy to see that the distribution was always the same).

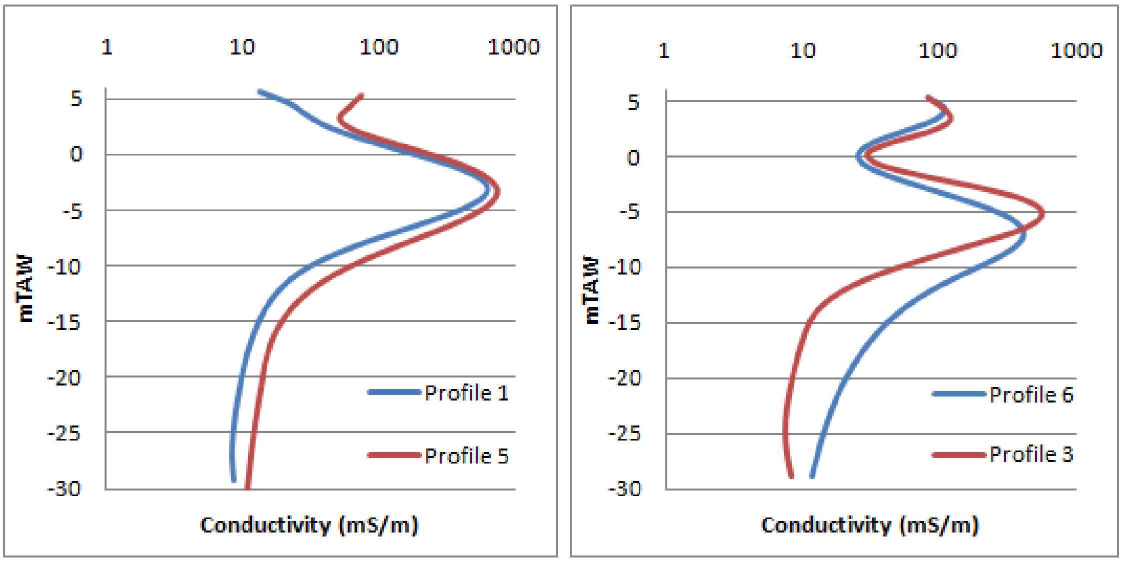

Figure 8.32: Correlation between profiles.

8.5.1 Resolution matrix

The concept of the resolution operator is defined to characterize the bias of an inverse problem solution (Aster *et al.*, 2005). Let us take the simple case of a least-square solution for a linear problem. We have

$$\mathbf{m}^* = (\mathbf{G}^T\mathbf{G})^{-1}\mathbf{G}^T\mathbf{d} \tag{8.6}$$

where $\mathbf{m}^*$ is the least-square solution. Data is such that $\mathbf{d} = \mathbf{Gm}$ (forward problem), thus we can write

$$\mathbf{m}^* = (\mathbf{G}^T\mathbf{G})^{-1}\mathbf{G}^T\mathbf{Gm} = \mathbf{Rm} \tag{8.7}$$

where $\mathbf{R}$ is called the resolution matrix and $\mathbf{m}$ is the true model. This matrix describes how a true model is found after the inversion process. Ideally, $\mathbf{R}$ should be an identity matrix. Analyzing the resolution matrix can give information about how some errors are introduced by the inversion process (Aster *et al.*, 2005).

In the case of the regularized problem of ERT using a geostatistical constraint, near the true model, equation 2.43 becomes (Kemna, 2000)

$$\mathbf{m}^* = (\mathbf{J}_k^T\mathbf{W}_\mathbf{d}^T\mathbf{W}_\mathbf{d}\mathbf{J}_k + \lambda\mathbf{C}_\mathbf{m}^{-1})^{-1}\mathbf{J}_k^T\mathbf{W}_\mathbf{d}^T\mathbf{W}_\mathbf{d}\mathbf{J}_k\mathbf{m} = \mathbf{Rm} \tag{8.8}$$

We can consider each line of $\mathbf{R}$ as a description of how the calculated model is smoothed by the inversion process. Ideally, each line should be very close to a Dirac impulsion located at the position of the considered parameter. A traditional way to assess the resolution of a parameter is to plot the diagonal of $\mathbf{R}$ and to see how it differs from 1. The smaller it is, the less resolved the parameter is.

One disadvantage of the resolution matrix is that it costs a lot of time to calculate it. Commercial programs such as RES2DINV do not give the possibility to calculate it. For example, the calculation time to get the resolution matrix of profile 1 was about 19hours on a calculation station working in 64bits with 4 processors.

Figure 8.33 shows the diagonal elements (logarithmic scale) of the resolution matrix for profile 1. We see that the resolution decreases with depth, as expected. Around $5m$ below the

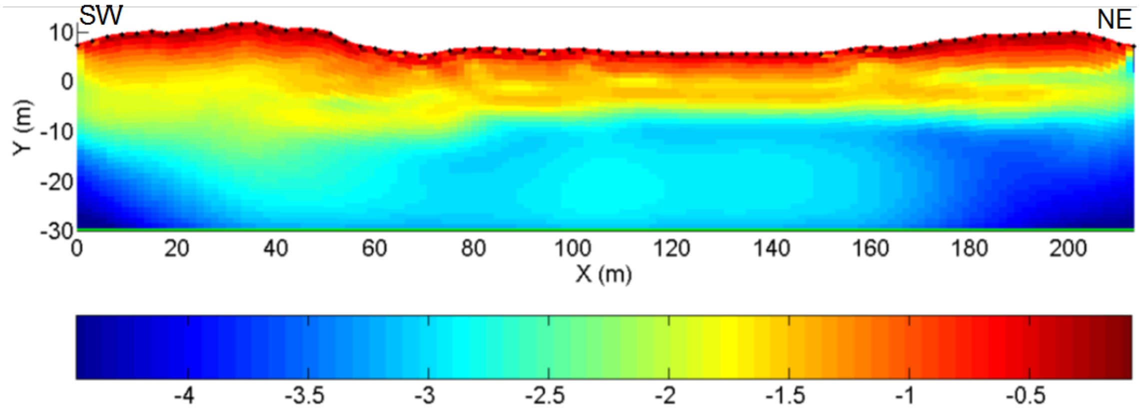

Figure 8.33: Diagonal elements of the resolution matrix. A logarithmic scale is used.

surface, the diagonal elements of the resolution matrix are already equal to 0.1. Around the depth of the intrusions, the value is only equal to 0.01. Only parameters near the surface are very well resolved. In depth, we see that the right and left sides of the section are slightly less resolved, it is due to the electrode array used to take the data, it did not enable to collect measurements influenced by this zone (this also explains the apparent upward freshwater discharge in figure 8.25). On a horizontal line, the resolution is quite constant.

This distribution can be easily understood. Three main things influence the resolution matrix: the way data was collected, the resistivity distribution and the regularization operator. First, all the electrodes were placed on the surface. Measures with low geometric factor investigated small volume of soil; it is thus not difficult to find the parameters with good resolution. To investigate in depth, higher geometric factors are used; distances between electrodes increase; a larger volume of soil and a higher number of parameters are concerned by one measurement. So, the resolution decreases. It would be possible to increase resolution in depth by doing measurements in boreholes. Then, during the inversion, a constraint on the model is used. Here, an estimation of the covariance matrix is determined, giving a correlation length in vertical and horizontal direction. The neighbors of a parameter influence the solution. It tends to obtain a solution that respects statistics, but has an influence on the resolution matrix.

8.5.2 Sensitivity matrix

Another image appraisal tool is the cumulative sensitivity matrix. If data uncertainty is taken into account, this matrix is defined as (Kemna, 2000)

$$\mathbf{S} = \mathbf{J}^T \mathbf{W}_\mathbf{d}^T \mathbf{W}_\mathbf{d} \mathbf{J} \tag{8.9}$$

It depends on both data weighting and parameters distribution. When the sensitivity of a parameter is high, it signifies that an increase or decrease of this parameter is going to influence strongly the data. In contrast, when the sensitivity of a parameter is low, its value has little influence on the data. Sensitivity is not synonymous with resolution. Indeed, a parameter can have a large sensitivity but a poor resolution.

However, in the case of ERT measurements made in the Westhoek, it seems that the distributions are quite similar. Figure 8.34 shows the relative sensitivity matrix. The sensitivity is high near the surface and decreases with depth. As salt water is a good current conductor, the sensitivity becomes very low under this zone. Indeed, current lines are concentrated in this high conductive zone. In contrast, on the left part of the section, where salt water is absent, higher sensitivity values are found. In this part, current lines are not concentrated due to low resistivity values.

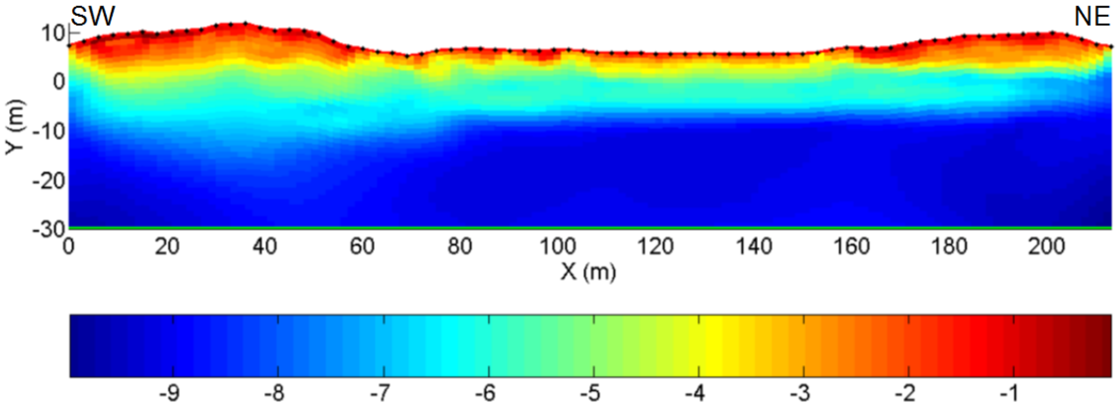

Figure 8.34: Relative sensitivity. A logarithmic scale is used.

In this case, we could use sensitivity as a good estimator of resolution. The advantage is that sensitivity is computed for each iteration of the inversion procedure and therefore available directly.

8.5.3 DOI index

The DOI index or Depth Of Investigation index was first defined by Oldenburg & Li (1999). Their aim is to change the reference model and to see where large differences occur in the inverted section. They suppose that such differences signify that the data does not constrain the model. The problem is to decide above which value of DOI the results cannot be interpreted. The value of DOI is defined as

$$DOI = \frac{|m_1 - m_2|}{|m_{ref1} - m_{ref2}|} \; with \; 0 \leq DOI \leq 1 \tag{8.10}$$

where m_{ref1} and m_{ref2} are two different reference models. In the case of covariance matrix regularization where a prior model is used, the starting model has little influence, m_{prior} was used instead of the starting model as a reference model. As a value of $100\,Ohm.m$ was chosen for the inversion, 10 and $1000\,Ohm.m$ were taken to determine the DOI index.

Figure 8.35 presents the DOI for profile 1. We directly detect two zones. Above $-10mTAW$, DOI values are low, except for some values in the dunes. It can be explained by the fact that the calculation is based on the logarithmic value. When resistivity values are high, like in unsaturated sands, a little change in the logarithm can lead to a high change in the resistivity value, it is what happened in the dunes. Low DOI indexes signify that these parameters are constrained by the data. We can thus assume that the detection of the intrusion is reliable.

The second zone is located below $-10m$, where we directly reach a DOI value of 1, with a small transition zone (3 or 4 cells). We know that under the salt water, sensitivity is low, it is quite logical to obtain high DOI index.

However, we can wonder if the calculation of the DOI is really relevant in our case. In the synthetic cases, we showed that when the sensitivity is low, the calculated model tends to the prior model. It is the reason why a homogeneous prior model was chosen, based on borehole data. We can thus hope that a value different from the prior signifies that data has a small influence on the parameter, even if the DOI index is close to 1. If it had not been the case, the value would have been equal to the homogeneous one. So, it should be possible to make a qualitative interpretation (small decrease in resistivity over here, small increase over there). Obviously, quantitative interpretations are more difficult. The same is true for the unsaturated

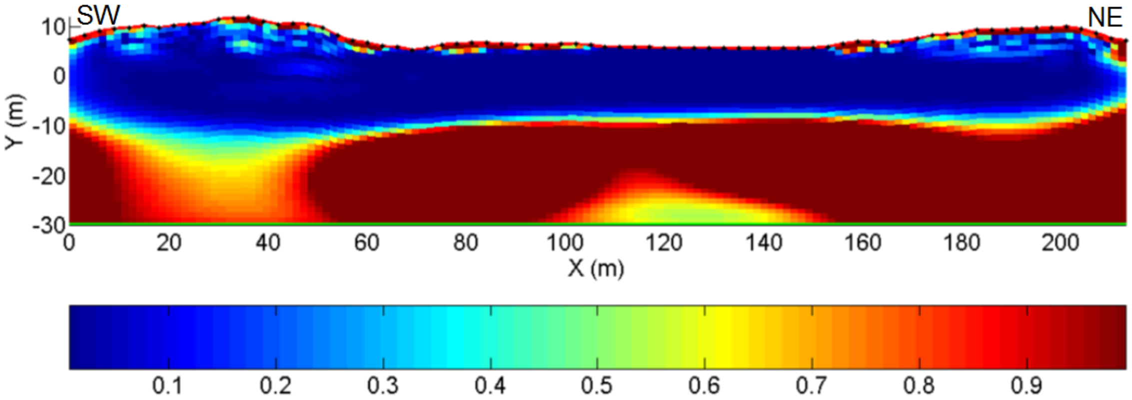

Figure 8.35: DOI index.

sand. Even if the DOI is high, we know that resistivity values are around $1000\,Ohm.m$ and it is sufficient for our interpretation.

8.5.4 Comparison with borehole data

The biggest difficulty with image appraisal tools is to find a cut-off value, below (above) which we cannot interpret the results or some kind of weighting/filtering scheme for the interpretation. As borehole data was available, it was interesting to compare calculated and measured values, and to see if image appraisal tools were able to reflect the correlation between both of them.

Figure 8.36 shows this type of comparison for P12. The same could be observed in P11 and P18. First, we see that there is a clear change under the salt water intrusion. Indeed, below the depth of the maximum conductivity value, sensitivity and resolution decrease rapidly, whereas DOI index tends quickly to 1. If we had to determine a depth of investigation based on these tools, we would certainly choose the depth of $-10mTAW$. Image appraisal tools seem to indicate where the prior constraint replaced the data constraint during inversion.

In this case, it is really difficult to define a cut-off value for the interpretation. Indeed, we saw during all the interpretation that a difference could exist between EM39 measurements and inversion results. The two curves are not superimposed, even if the trends are the same. This can be explained by the fact that it is more difficult to find an intrusion zone with this sharper shape than a smooth traditional interface as in Nguyen *et al.* (2009). It is the reason why the latter authors managed to define a sensitivity cut-off value for the interpretation, whereas it seems quite difficult in this case. Indeed, the fit is quite good at all depth. What we could do is to define a threshold value of image appraisal tools, indicating where the prior model takes over the data. According to figure 8.36, it would be 5.10^{-7} for the relative sensitivity, 10^{-2} for the diagonal element of the resolution matrix and 0.1 for the DOI.

Thus, these image appraisal tools failed to show the benefits of a prior model closed to the true one in depth. Indeed, we see that below $-20mTAW$, EM39 measurements and inverted ERT model are close to each other. It is logical as the prior model was chosen to obtain such results. One of the aims of this master thesis was to include prior information to constrain the model, it seems that a good prior model can help to obtain a good resolution in depth, even if it does not appear in image appraisal tools. Therefore, it is not necessary to find a threshold value when the prior model is adapted.

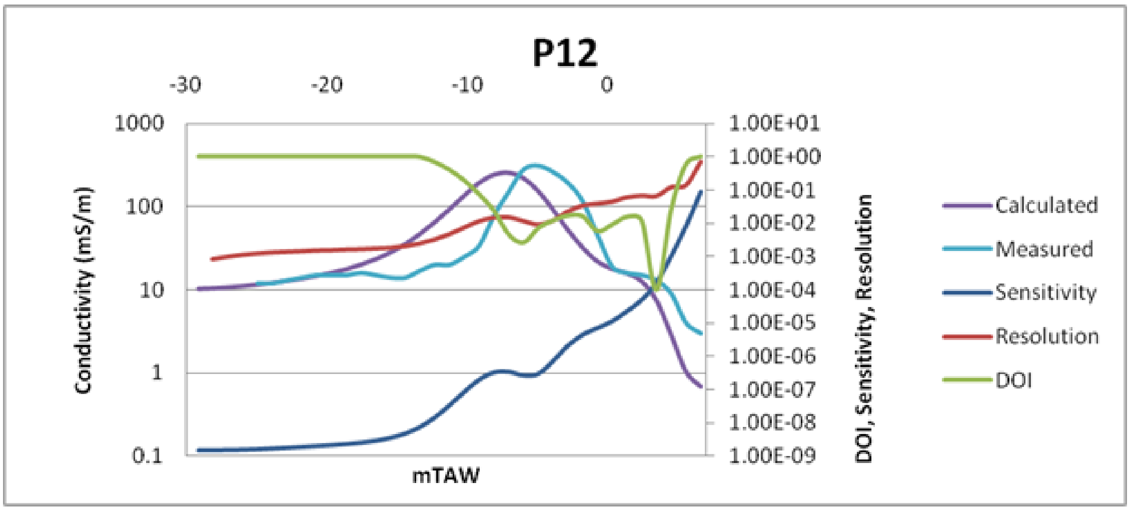

Figure 8.36: Image appraisal tools compared with borehole data.

8.6 Conclusion

The previous sections showed that the ERT campaign carried out in the Westhoek nature reserve enables to describe with much more accuracy and lateral resolution the sea water infiltration that occurred in the eastern pond than with EM39 measurements alone. To combine both types of geophysical data give us the opportunity to apply a geostatistical regularization, which leads to significant improvements compared to the traditional smoothness constraint solution.

Image appraisal tools and comparison with borehole measurements showed that the results are reliable, especially in the first fifty to twenty meters, i.e. until the depth of the salt water intrusion. In consequence, it was possible to make a quantitative interpretation of the results. The limits of the intrusion were detected in all directions. Towards the sea, there is a lateral flow that connects the intrusion with the salt water lens under the beach. Westwards (towards the other pond), salt water is found under the dunes, but not far from the perimeter of the pond (about $20m$). In the opposite direction, salt water is detected further from the limit of the pond. Indeed, low resistivity values are found until the end of the profiles parallel to the sea (1 and 6), salt water thus flowed at least 50m eastwards. Finally, the more worrying border, i.e. the limit located landward, since salt water could enter the water catchment pumping zone, is not a threat at the moment. The lateral flow brought salt water as far as 20 to $30m$ from the limit of the pond.

Orders of magnitude of the TDS content were deduced from resistivity values. At some places, this TDS content is almost equal to the one of the North Sea. Elsewhere, diffusion and dispersion led to reduce the salt content. In any case, it clearly appeared that lithological heterogeneity played a great role in the salt content distribution as well as the dynamic of intrusion. The intrusion is not a big plume, but is composed of several smaller plumes interconnected in a 3D complex network.

Chapter 9

Conclusions and perspectives

The four objectives of this master thesis were:

- the characterization (qualitative and quantitative) of a hydrogeological system affected by salt water intrusions/infiltrations;
- the development of algorithms to solve inverse problems, more specifically to implement regularization functionals taking advantage of borehole information;
- the quantification of the resolution of the solution;
- the possible update of the hydrogeological model according to the geophysical exploration.

The exploration plan developed on the site of the Westhoek, based mainly on electrical resistivity tomography and new EM39 measurements, was able to provide a good estimate of the state of water salinity due to artificial infiltration in the eastern inlet. Six profiles (3 parallel and 3 perpendicular to the sea) allowed us to have a detailed description of the intrusion in these directions and in depth. The depth and the lateral extensions were determined thanks to profiles going further from the pond than boreholes placed on the perimeter. In the eastern direction, salt water is found at least $50m$ away from the limit of the pond. In the western direction, the lateral extension is smaller, about 20 to $25m$. Landwards, the lateral flow was already proved by EM39 measurements. ERT allows us to confirm this movement and to show that salt water was not very far from the wells. Salt water is found $20 - 25m$ away from the limit of the infiltration pound, only ten meters further than P14 and P16. ERT also gave evidence for a lateral flow towards the sea, whereas no well was drilled to see it by another way.

In addition, the depth of the intrusion was determined almost everywhere. Heterogeneity in the first meters below the surface and in the semi-permeable clay layer was imaged and the influence of the lithology on the distribution of salt water was highlighted. These features explain why salt water is sometimes found slightly deeper or shallower in the aquifer.

A simple law was used to convert resistivity into orders of magnitude of TDS content. The distribution of TDS content on the different profiles showed the complexity of the intrusion shape due to an episodic infiltration scheme. It is important to have a general 3D view of the intrusions to understand the distribution of salt water in the dune aquifer. At some place, the salt content remains very close to the one of the North Sea. Elsewhere, diffusion and dispersion decreased the maximum value of TDS.

Since borehole data was available all around the pond, we tried to use them to constrain the inversion in an innovative way. As the possibility to impose resistivity values already enabled to constrain the inversion near boreholes, it was interesting to see the benefit of a tool enlarging this influence to all the sections. To achieve this, variograms were built to model borehole data. Assuming the stationarity, it allows us to calculate the covariance matrix of the model and to use it to regularize the inversion scheme.

Characteristics, drawbacks and benefits of this type of regularization were first shown on three synthetic cases. The role of the prior model was clearly highlighted and its importance in depth was demonstrated. It appeared that a small number of prior models, having a geological and a statistical validation could be used: a smoothness constraint inversion result, a homogeneous model, a Gaussian simulation. The first one often leads to a solution too close to the prior model. The third one needs a lot of inversion to obtain reliable results. In addition, several tests have shown that the sill value does not have to be known with a high precision. Indeed, better model misfits were obtained with an increased sill value. However, the synthetic cases also proved that a good estimate of the vertical range is necessary to find reliable results. The horizontal range is of lower importance. At the same depth, the sensitivity is often similar and data contains enough information to retrieve the continuity between structures. An underestimation of this parameter is not harmful to inversion results.

Inversions carried out with data collected in the Westhoek nature reserve permitted us to fully appreciate the improvement brought by the covariance matrix regularization. If smoothness constraint solutions were certainly sufficient for a simple qualitative interpretation of the intrusions, comparisons with EM39 measurements proved that the new type of regularization was able to give highly better results, concerning both resistivity value and the depth of intrusion. Inversions with covariance matrix as regularization tool was always better and enable a quantitative interpretation of geophysical results. Thanks to this development, prior information can be used to constrain the inversion everywhere, not only around boreholes.

Three image appraisal tools were calculated to try to quantify the resolution of geophysical imaging. If the results can be easily understood by the data collecting scheme and the inversion process, it appears that it was difficult to correlate these indexes with inverted and measured resistivity. A possible reason is the shape of the intrusion which is quite complex with an increase in resistivity where the sensitivity decreases. It was impossible to choose a cut-off value of these indexes to define zones where interpretation is possible. However, a threshold value show when the prior model takes over the data. In addition, all the indexes failed when showing the benefits of using prior information in a prior model. Indeed, an adapted prior model and the geostatistical regularization allow a better resolution. It does not appear in image appraisal tools, but it is visible in the comparison with borehole data.

It seems that phenomena predicted by modeling are actually observed in reality, both in EM39 and ERT measurements. The lateral flow that was modeled from previous studies was observed with ERT. Moreover, ERT measurements let us think that heterogeneity in the clay layer should lead to vertical flow of salt water deeper in the aquifer, and then towards the sea. There are few chances that the salt water will reach the water divide, thanks to lateral flow, and enter the water catchment. However, it could be useful to monitor the lateral flow towards the dunes with ERT in the next years and to explore the western pond with the same technique.

The results obtained for the Westhoek site proved the usefulness to develop new regularization tools, because the smoothness constraint solution cannot always lead to a good solution. It is interesting to use all the prior information available to constrain the inversion process. The first step was to calculate a covariance matrix, but it is possible to go further in this direction. It is already possible to define several zones where variogram parameters are different. More development could be done to improve the current algorithm. It might be possible to apply it on data collected on a profile such profile 2 of this study.

Another possible improvement of the inversion algorithm would be to allow the users to define the direction of anisotropy. At the moment, it is supposed (also for the smoothness constraint regularization) that minimum and maximum ranges are necessarily in vertical (horizontal) and horizontal (vertical) direction. However, we could have a different situation. Obviously, it would be very difficult to detect it with only few boreholes, but it would be interesting to have an algorithm capable of using the covariance matrix regularization in each possible situation. It is not difficult to do so, it is just a rotation of the main axis.

A very interesting progress could be to develop another tool to constrain the inversion, parallel to geostatistical regularization. This tool could be used to impose, up to a certain level, resistivity values determined by borehole measurements. In this way, it should be feasible to impose these values and to use another regularization. We showed that we could realize this by using conditioned Gaussian simulation. However, it cost a lot of time to obtain reliable results also in depth. In consequence, it is illusory to use this type of prior model in engineering applications. In contrast, if a prior model and borehole data are implemented separately, the prior model could remain homogeneous. In this way, it should be possible to obtain a good solution with only one realization, and thus, a similar calculation time.

Another perspective is to develop an algorithm similar to the one of Johnson *et al.* (2007). They also incorporate a geostatistical constraint, but by another way. Indeed, they do not use the covariance matrix regularization but a variogram misfit to constrain the inversion. In this way, they want their calculated model to respect the variogram up to a defined level. At the end of the inversion process, they have a model fitting the data and the statistics. However, they give less freedom to their model. It could be harmful in our cases, because the upper part of the section is well resolved; we want to avoid distorting it to verify an estimation of the statistics.

An interesting perspective for further research work is to try to uncouple the different effects responsible for changes in resistivity values best: salt content, temperature, saturation and formation factor (i.e. type of rock or sediments). It would be very interesting to have a general framework in which each parameter could be taken into account. Obviously, it is utopian to think that it could be possible to invert the data and to obtain all these parameters, since the inverse problem is already severely ill-posed, whereas they have similar effect on the data. It would be necessary to use all the data available in boreholes, but also to use other geophysical methods which could identify clay and sands filled with salt water for example. In this case, we tried to use induced polarization to identify clay. Unfortunately, the salt content was too high to provide good results. However, in other cases, such approach could be successful. To combine several geophysical method, at different scales, is very exciting work. Geostatistical approach could be very helpful to build such framework.

In this master thesis, a variogram-based technique to regularize the inversion process was used. It is a two-point correlation method and it enabled to describe the heterogeneous medium. However, for more complex medium, with multimodal distributions and curvilinear structures, a geostatistical framework based on multiple-point geostatistics could describe the geological heterogeneity better. At the moment, few studies (Trainor *et al.*, 2007) have combined multiple-point geostatistics and near-surface geophysics. It is also an interesting prospect that we hope to explore soon.

Bibliography

[1] Amidu S. A. & Dunbar J. A. 2008. An evaluation of the electrical-resistivity method for water-reservoir salinity studies. *Geophysics*, 73, (4), G39-G49.

[2] Archie G. E. 1942. The electrical resistivity log as an aid in determining some reservoir characteristics. *Transactions AIME*, 146, 54-62.

[3] Aster R. C., Borchers B. & Thurber C. 2005. *Parameter estimation and inverse problems.* Amsterdam, Elsevier Academic Press, 301pp.

[4] Baeteman C. 1985. Development and evolution of sedimentary environments during the Holocene in the Western coastal plain of Belgium. *Eiszeitalter und Gegenwart*, 35, 23-32.

[5] Baeteman C. 1991. Chronology of coastal plain development during the Holocene in West Belgium. *Quaternaire*, 2, (3-4), 116-125.

[6] Baeteman C. 1999. The Holocene depositional history of the IJzer palaeo-valley (Western Belgian coastal plain) with reference to the factors controlling the formation of intercalated peat beds. *Geologica Belgica*, 2, (3-4), 39-72. http://popups.ulg.ac.be/Geol/docannexe.php?id=2365 Viewed : February 25, 2010.

[7] Baeteman C. 2005. *Geological map of Belgium : Holocene deposits of the coastal plain - De Panne - Oostduinkerke 11/7-8 - Nieuwpoort - Leke 12/5-6 - Middelkerke - Oostende 12/1-2.* 1/25000. Brussels, Belgian geological survey, 2 sheets.

[8] Belligoi T., Bouhon O., Delvoie S., Gerard B. & Hermans T. 2008. *Saline tracer test monitored by electrical resistivity tomography in a fractured aquifer zone.* Student work realized within the context of the "Applied geophysics course", University of Liege, Liege, unpublished, 74pp.

[9] Boulvain F. 2010. *Une introduction à le géologie de la Wallonie.* Course notes, University of Liege, Liege, 179pp. http://www2.ulg.ac.be/geolsed/geolwal/geolwal.htm Viewed : March 15, 2010.

[10] Carter E. S., White S. M. & Wilson A. M. 2008. Variation in groundwater salinity in a tidal salt marsh basin, North Inlet Estuary, South Carolina. *Estuarine, coastal and shelf science*, 76, 543-552.

[11] Cassiani G., Bruno V., Villa A., Fusi N. & Binley A. M. 2006a. A saline trace test monitored via time-lapse surface electrical resistivity tomography. *Journal of applied geophysics*, 59, 244-259.

[12] Cassiani G., Binley A. & Ferré T. 2006b. Unsaturated zone processes. In : Vereecken H., Binley A., Cassiani G., Revil A. & Titov K. (Eds.) *Applied hydrogeophysics.* Nato Science Series, Serie IV, Earth and environmental sciences, 71, Dordrecht, Springer, 75-116.

[13] Chasseriau P. & Chouteau M. 2003. 3D gravity inversion using a model of parameter covariance. *Journal of applied geophysics*, 52, 59-74.

[14] Cheng A.H.-D. & Ouazar D. 2004. *Coastal aquifer management: monitoring, modeling, and case studies.* Boca Raton, Lewis Publishers, 296pp.

[15] Columbia University's Center for Climate Systems Research (CCSR). 2006. *Mapping the Future of World Population.* New-York, Columbia University. http://www.populationaction.org/Publications/Reports/Mapping_the_Future_of_World_Population/Interactive_Map.shtml Viewed : May 31, 2010.

[16] Dahlin T. & Zhou B. 2004. A numerical comparison of 2D resistivity imaging with ten electrode arrays. *Geophysical prospecting*, 52, 379-398.

[17] Databank Ondergrond Vlaanderen (DOV). 2010. *DOV informeeret u over de ondergrond in Vlaanderen.* Vlaamse Milieumaatschappij. http://dov.vlaanderen.be/dov/DOVInternet/startup.jsp Viewed : March 15, 2010.

[18] De Franco R., Biella G., Tosi L., Teatini P., Lozej A., Chiozzotto B., Giada M., Rizzetto F., Claude C., Mayer A., Bassan V. & Gasparetto-Stori G. 2009. Monitoring the saltwater intrusion by time lapse electrical resistivity tomography: The Chioggia test site (Venice Lagoon, Italy). *Journal of applied geophysics*, 69, 117-130.

[19] Denys L. & Baeteman C. 1995. Holocene evolution of relative sea-level and local mean high water spring tides in Belgium - a first assessment. In: Van de Plassche O., Chrzastowski M. J., Orford J. D., Hinton A. & Long A. J. (Eds.) Coastal evolution in the Quaternary, *Marine geology*, IGCP Project 274, 124, 1-19.

[20] Geotomo software. 2005. *Res2Dinv : 2D Resistivity and IP inversion.* Malaysia, Geotomo software. http://www.geoelectrical.com/downloads.php Viewed : September 29, 2008.

[21] Gneiting T., Sasvári Z. & Schlather M. 2000. *Analogies and correspondences between variograms and covariance functions.* Washington, NRCSE, Technical report series, 56, 18pp. http://www.nrcse.washington.edu/pdf/trs56_covar.pdf Viewed : April 5, 2010.

[22] Goldman M. & Kafri U. 2006. Hydrogeophysical applications in coastal aquifers. In : Vereecken H., Binley A., Cassiani G., Revil A. & Titov K. (Eds.) *Applied hydrogeophysics.* Nato Science Series, Serie IV, Earth and environmental sciences, 71, Dordrecht, Springer, 233-254.

[23] Hayley K., Bentley L. R., Gharibi M. & Nightingale M. 2007. Low temperature dependence of electrical resistivity: Implications for near surface geophysical monitoring. *Geophysical research letters*, 34, L18401, 5pp.

[24] Jacobs P., De Ceukelaire M., Moerkerke G. & Polfliet T. 1998. *Geologische Kaart van Belgie, Vlaams gewest. Kaartblad (4-5-11-12). Blankenberge - Westkapelle - Oostduinkerke - Oostende.* 1/50000. Brussel, Belgische Geologische Dienst : Ministerie van de Vlaamse Gemeenshap, Afdeling Natuurlijke Rijkdommen en Energie, 1 map, 1 plate of sections, 4 transparent plastic overlays.

[25] Jacobs P., De Ceukelaire M., Moerkerke G. & Polfliet T. 2002. *Toelichting bij de Geologische Kaart van België, Vlaams gewest. Kaartblad (4-5-11-12). Blankenberge - Westkapelle - Oostduinkerke - Oostende.* 1/50000. Brussel, Belgische Geologische Dienst : Ministerie van de Vlaamse Gemeenshap, Afdeling Natuurlijke Rijkdommen en Energie.

[26] Johnson T. C., Routh P. S., Clemo T., Barrash W. & Clement W. P. 2007. Incorporating geostatistical constraints in nonlinear inversion problems. *Water resources research*, 43, W10422, 18 pp.

[27] Kaufman A. A. & Keller G.V. 1983. *Frequency and transient Soundings*. Amsterdam, Elsevier, 685pp.

[28] Kemna A. 2000. *Tomographic inversion of complex resistivity : Theory and application*. Osnabrück, Der Andere Verlag, 176pp.

[29] Kemna A., Vanderborght J., Kulessa B. & Vereecken H. 2002. Imaging and characterisation of subsurface solute transport using electrical resistivity tomography (ERT) and equivalent transport models. *Journal of hydrology*, 267, 125-146.

[30] Koestel J., Kemna A., Javaux M., Binley A. & Vereecken H. 2008. Quantitative imaging of solute transport in an unsaturated and undisturbed soil monolith with 3-D ERT and TDR. *Water resources research*, 44, W12411, 17pp.

[31] Laboratoria Van Vooren. 2005. *Monitoring slufters De Panne, peilputten aanlegen, rapport*. Laboratoria Van Vooren, confidential report.

[32] LaBrecque D. J., Miletto M., Daily W., Ramirez A. & Owen E. 1996. The effects of noise on Occam's inversion of resistivity tomography data. *Geophysics*, 61, (2), 538-548.

[33] Lebbe L. 1978. *Hydrogeologie van het duingebied ten westen van De Panne*. PhD Thesis, Ghent, University of Ghent, 164pp. (+figures), unpublished.

[34] Lebbe L. 1999. Parameter identification in fresh-saltwater flow based on borehole resistivities and freshwater head data. *Advances in water ressources*, 22, (8), 791-806.

[35] Legrand, R. 1968. *Le Massif du Brabant*. Mémoires pour servir à l'explication des cartes géologiques et minières de la Belgique, 9, 1-148.

[36] Loke M. H. 2002. *Res2Dmod : 2D Resistivity and IP Forward Modelling*. Malaysia, Geotomo software. http://www.geoelectrical.com/downloads.php Viewed : September 29, 2008.

[37] Loke M. H. 2004. *Tutorial : 2-D and 3-D electrical imaging surveys*, 136pp. http://www-geo.phys.ualberta.ca/~unsworth/UA-classes/223/loke_course_note.pdf Viewed : March 3, 2010.

[38] Luyten K. 2003. *Grondwatermodellering van dichtheidsafhankelijke grondwaterstroming rond de waterwinning van De Panne*. Master thesis, Ghent, University of Ghent, 199pp., unpublished.

[39] Manheim F. T., Krantz D. E. & Bratton J. F. 2004. Studying ground water under Delmarva coastal bays using electrical resistivity. *Ground water – Ocean issue*, 42, (7), 1052-1068.

[40] Marcotte D. 2009. *Géologie et géostatistique minière (partie géostatistique)*. Course notes, Montréal, Ecole polytechnique de Montréal. http://geo.polymtl.ca/~marcotte/glq3401geo.html Viewed : April 15, 2009.

[41] Maréchal R. 1992. *Deuxième atlas de Belgique. Planche II.3, Commentaire*. Géologie du Quaternaire : lithologie des terrains superficiels. Bruxelles, Service géologique de Belgique.

[42] Martínez J., Benavente J., García-Aróstegui J. L., Hidalgo M. C. & Rey J. 2009. Contribution of electrical resistivity tomography to the study of detrital aquifers affected by seawater intrusion-extrusion effects: The river Vélez delta (Vélez-Málaga, southern Spain). *Engineering geology*, 108, 161-168.

[43] McNeill, J.D. 1980. *Electromagnetic terrain conductivity measurement at low induction numbers.* Geonics Limited technical note TN-6, 13pp. http://geonics.com/pdfs/technicalnotes/tn6.pdf Viewed : February 6, 2010.

[44] McNeill, J.D. 1986. *Geonics EM39 borehole conductivity meter - Theory of operation.* Geonics Limited technical note TN-20, 18pp. http://geonics.com/pdfs/technicalnotes/tn20.pdf Viewed : February 6, 2010.

[45] Møller I., Sørensen K. I. & Auken E. 2006. Geoelectrical methods. In: Kirsch R., Rumpel H.-M., Scheer W. & Wiederhold H. (Eds.) *Groundwater resources in buried valleys: a challenge for geosciences.* Hannover, BurVal Working group, 77-88. http://www.burval.org/final/pdf/077-088.pdf Viewed February 26, 2010.

[46] Nguyen F. 2009. *Modélisation et inversion en géophysique.* Course notes, Liege, University of Liege, unpublished.

[47] Nguyen F., Kemna A., Antonsson A., Engesgaard P., Kuras O., Ogilvy R., Gisbert J., Jorreto S. & Pulido-Bosch A. 2009. Characterization of seawater intrusion using 2D electrical imaging. *Near surface geophysics*, 7, 377-390.

[48] Nielsen L., Jørgensen N. O. & Gelting P. 2007. Mapping of the freshwater lens in a coastal aquifer on the Keta Barrier (Ghana) by transient electromagnetic soundings. *Journal of applied geophysics*, 62, 1-15.

[49] Oldenburg D.W. & Li Y., 1999. Estimating depth of investigation in DC resistivity and IP surveys. *Geophysics*, 64, (2), 403-416.

[50] Pannatier Y. 1996. *VarioWin : Software for spatial data analysis in 2D.* New-York, Springer-Verlag, 91pp.

[51] Parasnis D. S. 1988. Reciprocity theorems in geoelectric and geoelectromanetic work. *Geoexploration*, 25, 177-198.

[52] Perkin R. G. & Lewis E. L. 1980. The practical salinity scale 1978 : Fitting the Data. *IEEE Journal of oceanic engineering*, 5, (1), 9-16.

[53] Remy N. 2008. *Stanford Geostatistical Modeling Software.* Palo Alto, Stanford University.

[54] Replogle J. A., Clemmens A. J. & Jensen M. E. 1996. Irrigation Systems. In : Mays L. W. (Ed.) *Water resources handbook*, New-York, Mc Graw-Hill, 22.1-22.31.

[55] Risch M. & Robinson B. 2001. Use of borehole and surface geophysics to investigate ground water quality near a road deicing salt storage facility, Valparaiso, Indiana, USGS *Water resources investigations report*, 00-4070. http://pubs.er.usgs.gov/usgspubs/wri/wri004070 Viewed : May 31, 2010.

[56] Robert T., Dassargues A., Brouyère S., Kaufmann O., Hallet V. & Nguyen F. 2009. Assessing the contribution of electrical resistivity tomography (ERT) and self-potential (SP) methods for a water well drilling program in fractured/karstified limestones. Submitted to *Journal of applied geophysics.*

[57] Sasaki Y. 1994. 3-D inversion using the finite-element method. *Geophysics*, 59, 1839-1848.

[58] Slater L., Binley A.M., Daily W. & Johnson R. 2000. Cross-hole electrical imaging of a controlled saline tracer injection. *Journal of applied geophysics*, 44, 85-102.

[59] Tarantola A. 2005. *Inverse problem theory and methods for model parameters estimation.* Philadelphia, Society for Industrial and Apllied Mathematics, 342pp.

[60] Telford W. M., Geldart L. P. & Sheriff R. E. 1990. *Applied geophysics.* Cambridge, Cambridge University Press, 770pp.

[61] Todd D. K. & Mays L. W. 2005. *Groundwater hydrology*, Third edition. Hoboken, John Wiley & Sons, 636pp.

[62] Trainor W. J., Knight R.J. & Caers J.K. 2007. Multiple-point geostatistics and near-surface geophysics for modeling heterogeneity in a coastal aquifer, *AGU Fall meeting abstracts*, H42B-04. http://adsabs.harvard.edu/abs/2007AGUFM.H42B..04T Viewed : February 26, 2010.

[63] Van Meir N. & Lebbe L. 1998. Simulations of evolution of salt-water distribution in young dunes near the French-Belgian border. In : Proceedings, *Salt water intrusion meeting*, 15^{th}, Ghent. Ghent, Belgium, Flemish journal of natural science, 79, 105-113.

[64] Van Meir N. & Lebbe L. 2003. Deriving TDS values in coarse sediments from long normal and electromagnetic logs. *Ground water*, 41, (1), 33-40.

[65] Vandenbohede A. & Lebbe L. 2002. Numerical modeling and hydrochemical characterization of a fresh-water lens in the Belgian coastal plain, *Hydrogeology journal*, 10, 576-586.

[66] Vandenbohede A. & Lebbe L. 2006a. Occurrence of salt water above fresh water in dynamic equilibrium in a coastal groundwater flow system near De Panne, Belgium. *Hydrogeology journal*, 14, 462-472.

[67] Vandenbohede A. & Lebbe L. 2006b. *Monitoring van het grondwater van de slufter te De Panne.* Universiteit Gent. Opdrachtgever : Administratie Waterwegen en Zeewezen, 57pp., confidential report.

[68] Vandenbohede A., Lebbe L., Gysens S., Delecluyse K. & DeWolf P. 2008a. Salt water infiltration in two artificial sea inlets in the Belgian dune area. *Journal of hydrology*, 360, 77-86.

[69] Vandenbohede A., Lebbe L. & Courtens C. 2008b. *De Panne - Natuurreservaat - De Westhoek : Monitoring grondwater slufters. Fase 2. 2e tussentijds rapport.* Universiteit Gent. Opdrachtgever : Ministerie van Mobiliteit en Openbare Werken, Agentschap voor Maritieme Dienstverlening en Kust, Afdeling Kust, 55pp., confidential report.

[70] Vandenbohede A., Lebbe L. & Courtens C. 2009. *De Panne - Natuurreservaat - De Westhoek : Monitoring grondwater slufters. Fase 2. 3e tussentijds rapport.* Universiteit Gent. Opdrachtgever : Ministerie van Mobiliteit en Openbare Werken, Agentschap voor Maritieme Dienstverlening en Kust, Afdeling Kust, 11pp., confidential report.

[71] Verwaest T., De Wolf P., Herrier J.-L. & Leten M. 2005. Windows in the dunes - the creation of sea inlets in the nature reserve de Westhoek in de Panne. In : Herrier J.-L., Mees J., Salman A., Seys J., Van Nieuwenhuyse H. & Dobbelare I. (Eds.), *Proceedings "Dunes end Estuaries 2005" - International Conference on Nature Restoration Practices in European Coastal Habitats*, Koksijde, Belgium, 19-23 September 2005, vol. 19. VLIZ Special Publication, 433-439. http://www.vliz.be/imisdocs/publications/73836.pdf Viewed : 31 May, 2010.

[72] Waxman M. H. & Smits L. J. M. 1968. Electrical conductivities in oil-bearing shaly sands, *Society of Petroleum Engineers Journal*, 8, 107-122.

Appendix A

EM39 measurements

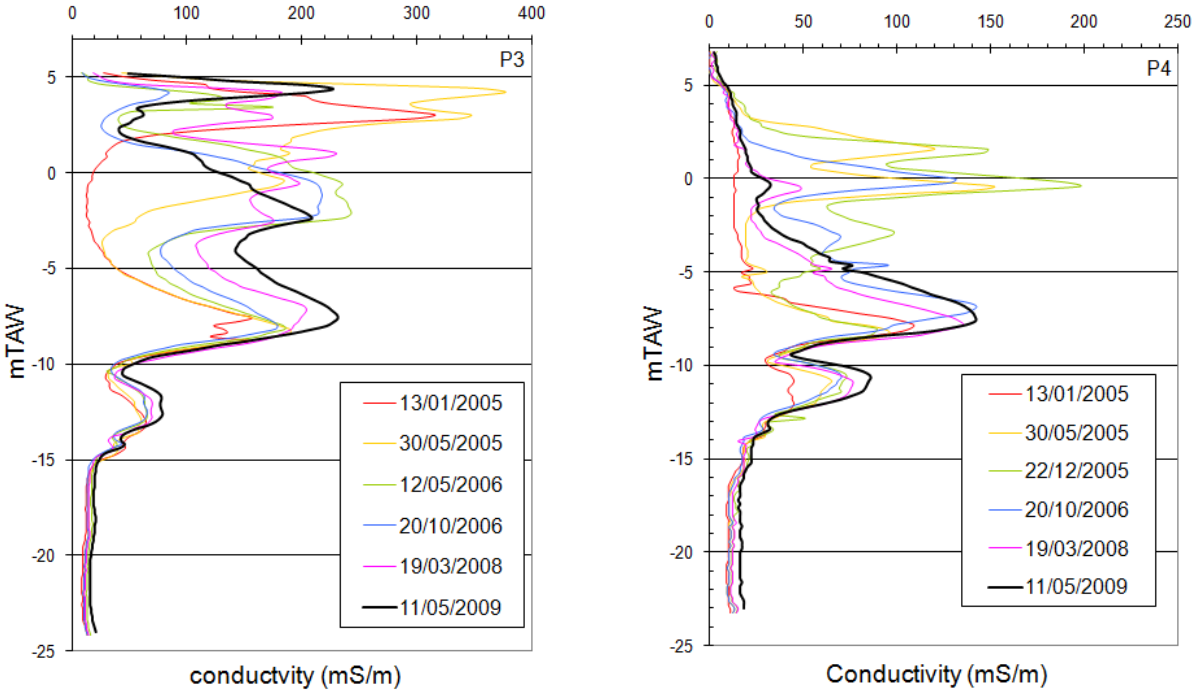

Figure A.1: EM39 conductivity data in P3 and P4 (modified after Vandenbohede *et al.*, 2009).

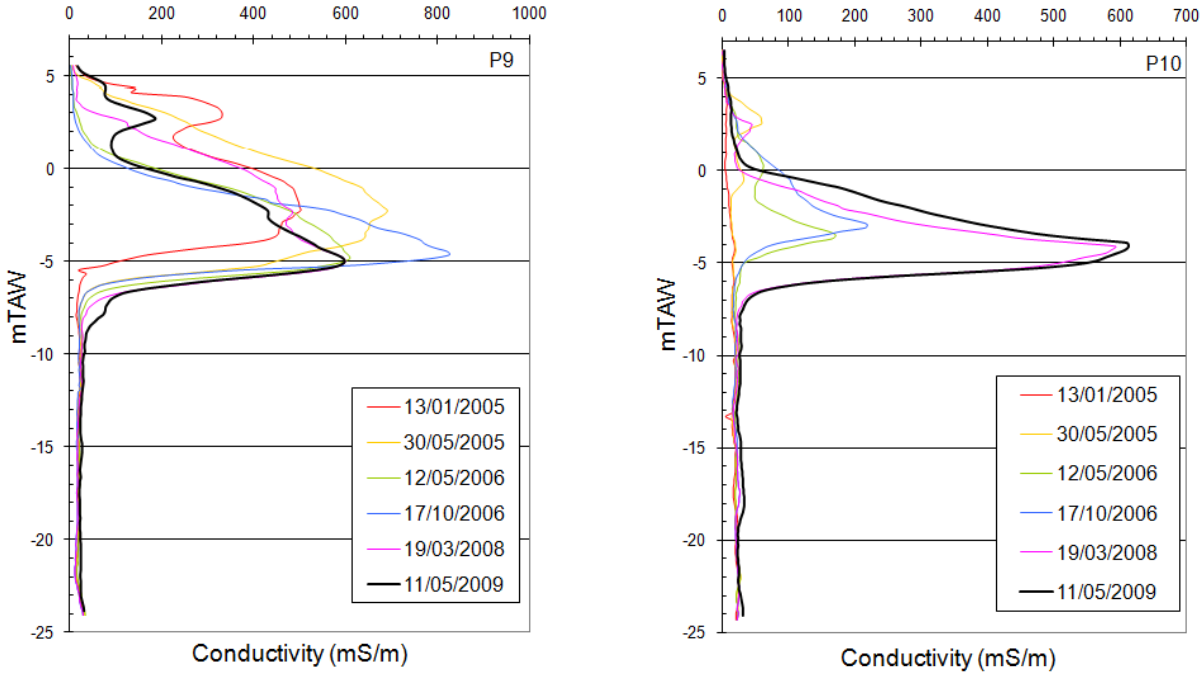

Figure A.2: EM39 conductivity data in P9 and P10 (modified after Vandenbohede *et al.*, 2009).

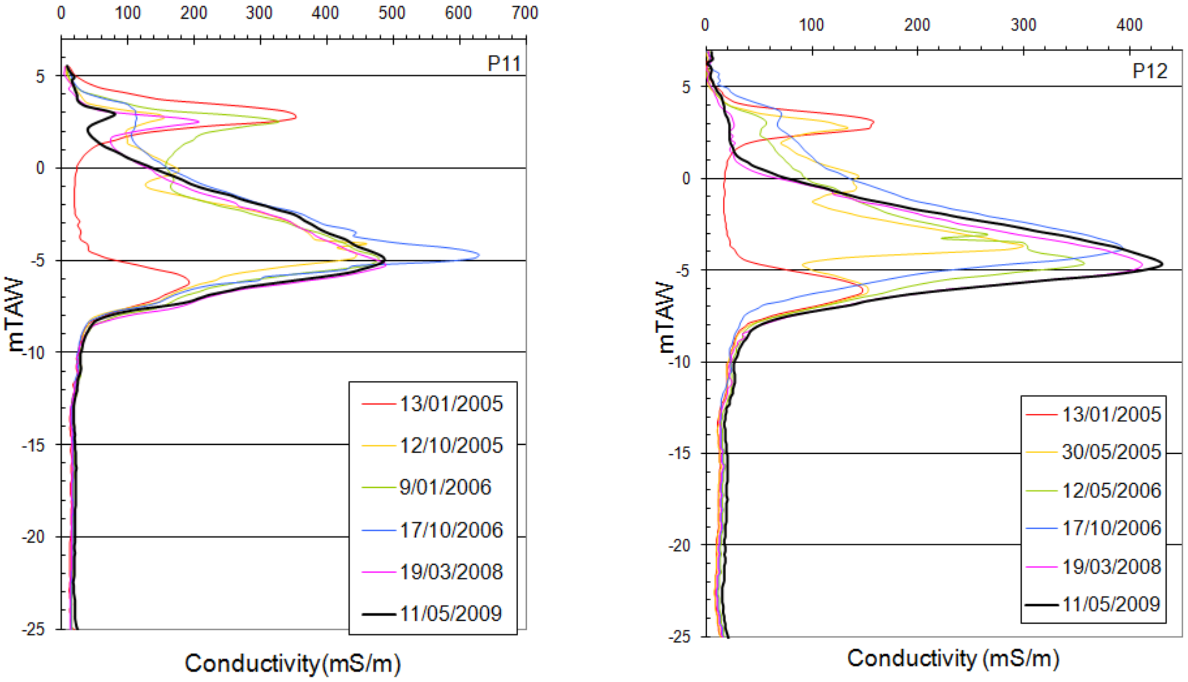

Figure A.3: EM39 conductivity data in P11 and P12 (modified after Vandenbohede *et al.*, 2009).

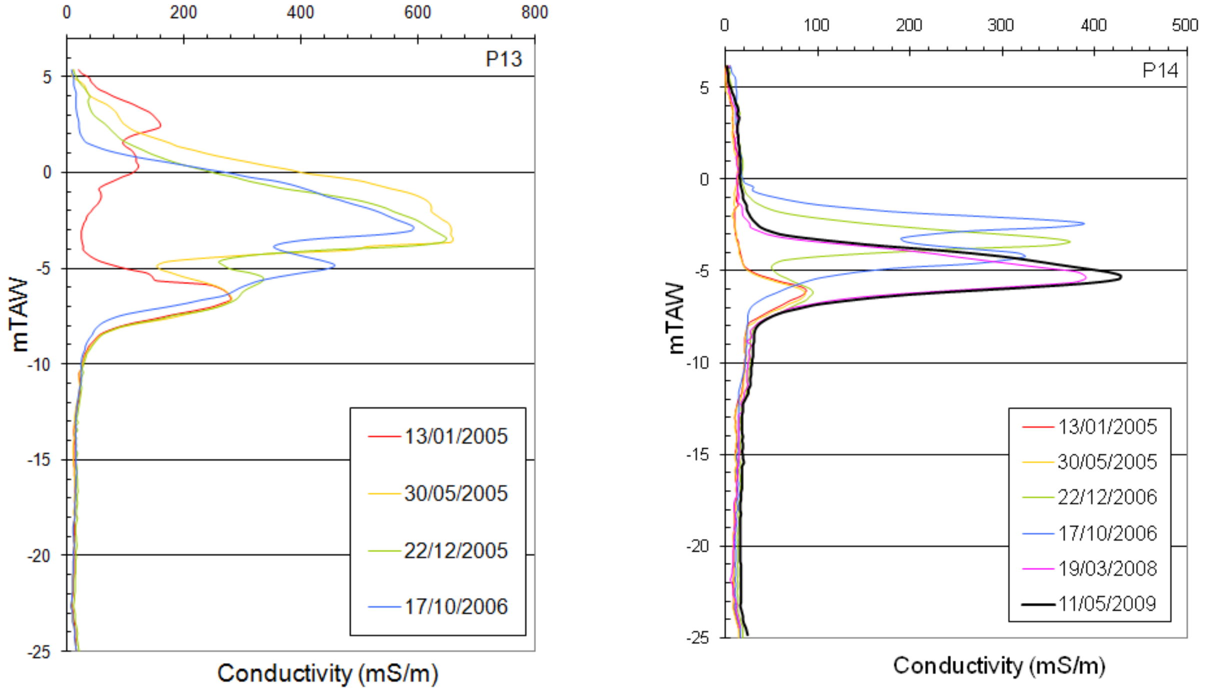

Figure A.4: EM39 conductivity data in P13 and P14 (modified after Vandenbohede *et al.*, 2009).

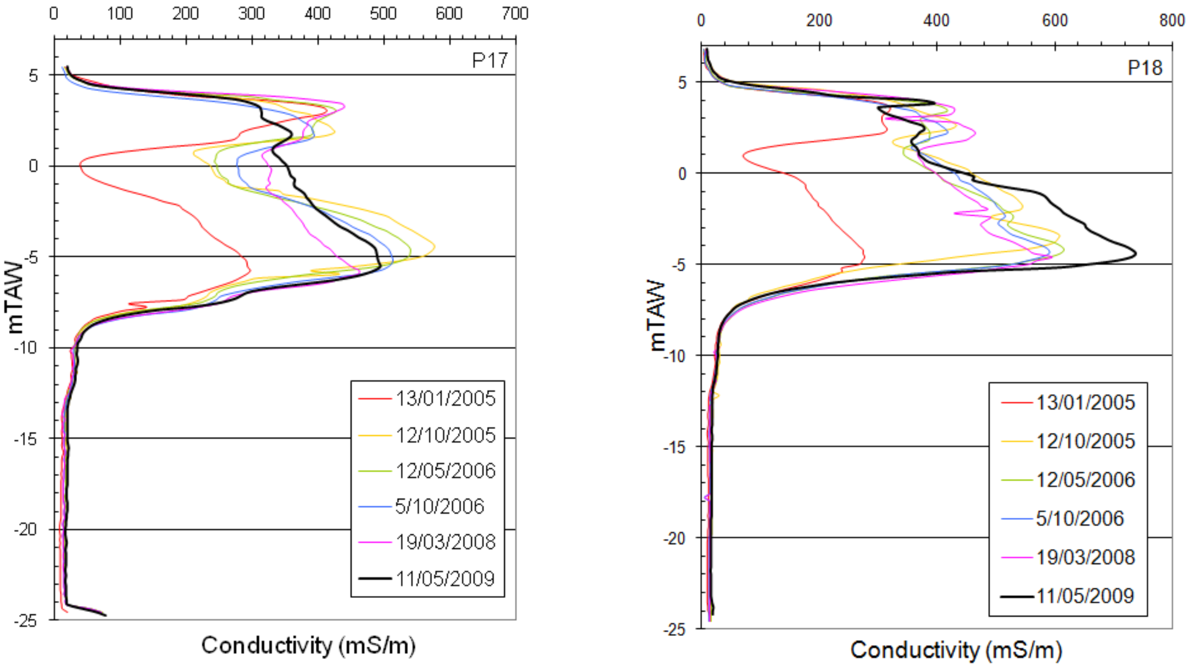

Figure A.5: EM39 conductivity data in P17 and P18 (modified after Vandenbohede *et al.*, 2009).

Appendix B

Variograms

Figures B.1 to B.5 present variogram for each well. The points above $|h| = 15m$ do not have to be taken into account, as they correspond to a distance greater than half of the field length (about $30m$)

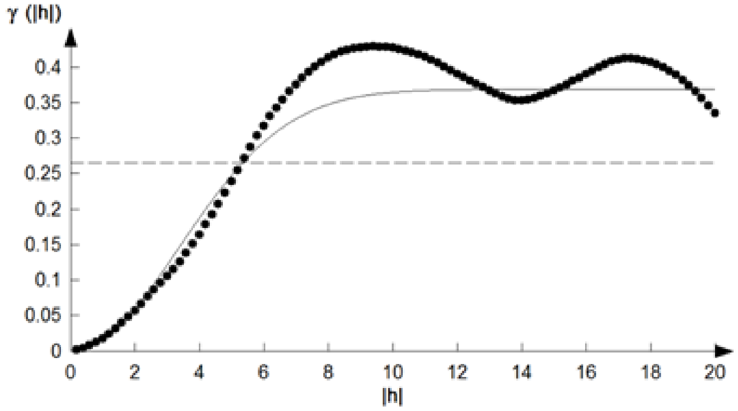

Figure B.1: Variogram of P11 data.

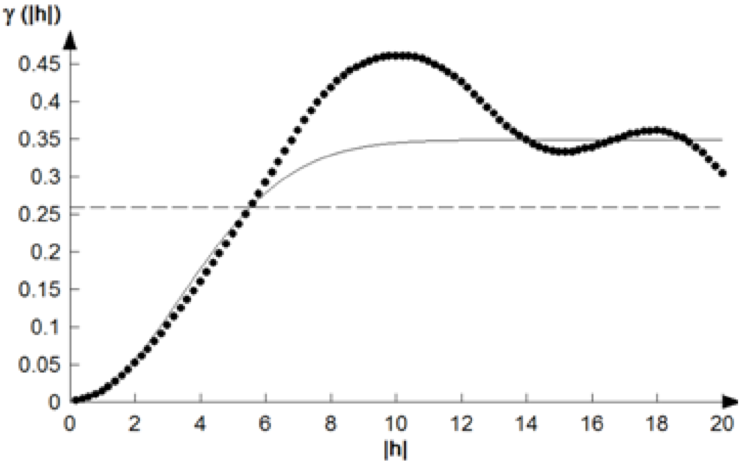

Figure B.2: Variogram of P12 data.

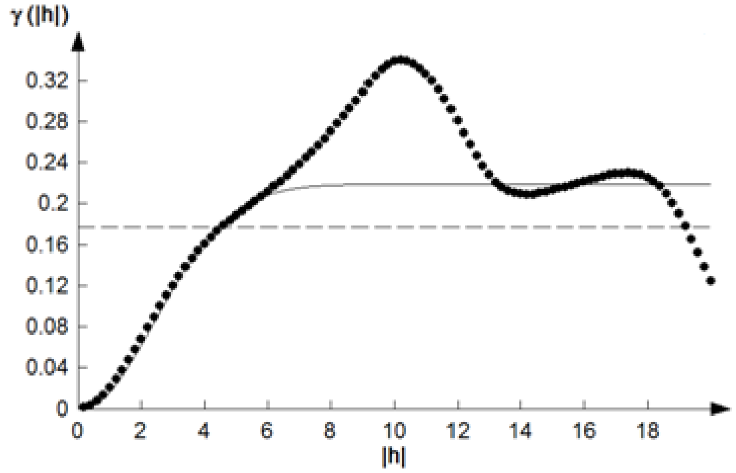

Figure B.3: Variogram of P14 data.

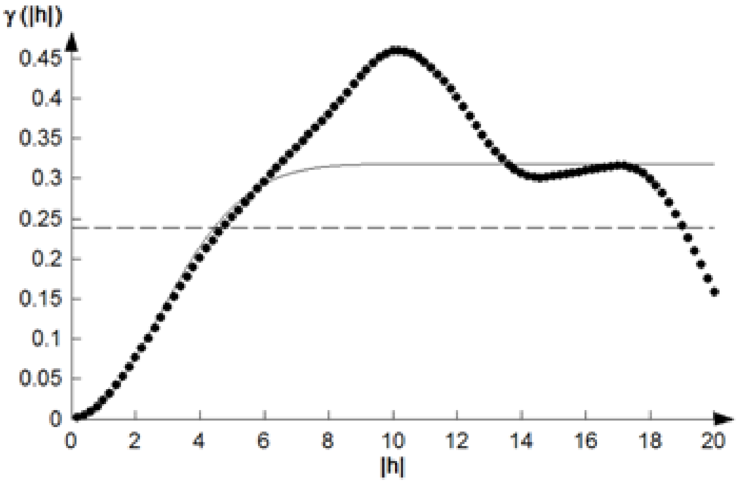

Figure B.4: Variogram of P16 data.

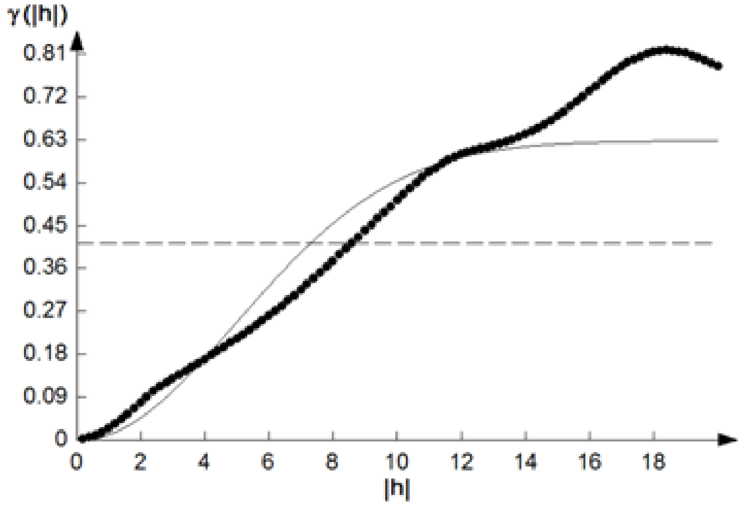

Figure B.5: Variogram of P18 data.

Appendix C

Profile 5

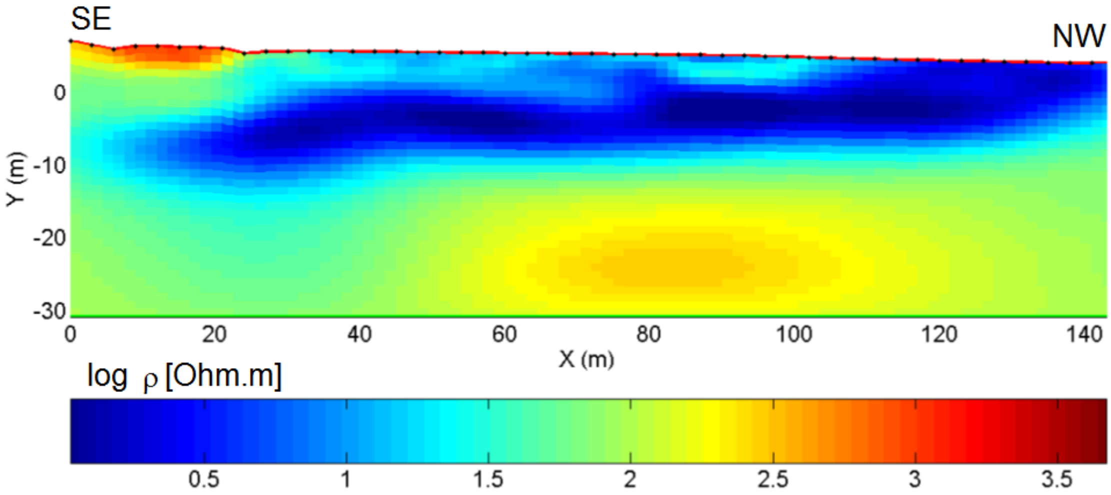

Figure C.1: Homogeneous prior model solution for profile 5 (scale in $\log \rho[Ohm.m]$).

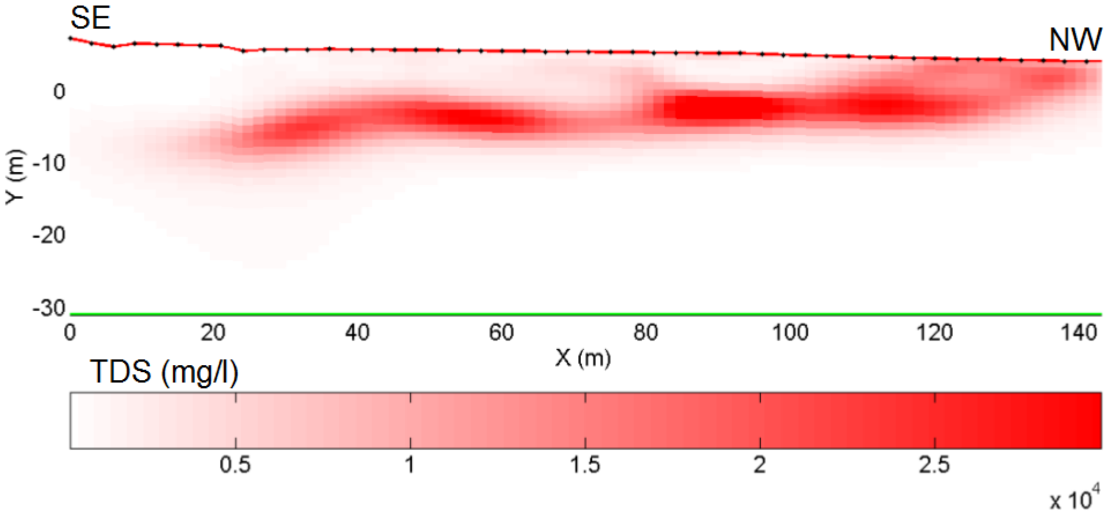

Figure C.2: TDS content (mg/l) for profile 5.

Abstract

Two artificial sea inlets were built in the nature reserve "The Westhoek". Consequently, sea water infiltrated in the dune aquifer filled with fresh water and exploited by a water company. Due to the presence of a clayey layer with a low hydraulic conductivity, the vertical flow of salt water was stopped, leading to a horizontal flow outside the infiltration ponds. Electrical resistivity tomographies were carried out, in addition to borehole electromagnetic measurements. The latter were used to calculate a vertical variogram, characteristic of the study site. Then, a geostatistical constraint was imposed as a regularization tool to solve the inverse problem, with a covariance matrix based on the variogram. The important points of this type of regularization were first highlighted by several synthetic cases. The main conclusions were that the choice of a homogeneous prior model seemed judicious in this case, whereas the lack of information to determine the horizontal variogram was not a major issue. Inversion results enabled to determine the extension of the salt water plume laterally, in depth, but also in terms of total dissolved solid content (TDS). These observations are in agreement with the hydrogeological situation of the site. A comparison with borehole data showed that the results are much more satisfying than a traditional smoothness constraint used as a regularization tool. Prior information included in the inversion process enabled to improve the resolution, even if traditional image appraisal tools failed to quantify this contribution.

Keywords : salt water intrusion, Belgian coast, electrical resistivity, electromagnetic method, geostatistical constraint, inversion process, resolution.

Résumé

Deux bras de mer artificiels ont été creusés dans les dunes de la réserve naturelle du Westhoek. Par conséquent, de l'eau de mer s'est infiltrée dans l'aquifère d'eau douce située au sein des dunes et exploitée pour la production d'eau potable. A cause de la présence d'une couche argileuse peu perméable, le mouvement vertical de l'eau salée a été stoppé, entrainant un flux horizontal vers l'extérieur du bassin d'infiltration. Des tomographies électriques ont été réalisées en complément de mesures électromagnétiques en forage. Ces dernières ont été utilisées pour calculer un variogramme vertical caractéristique du site. Ensuite, une contrainte géostatistique a été imposée comme outil de régularisation pour résoudre le problème inverse, par l'intermédiaire de la matrice de covariance basée sur le variogramme. Les points majeurs d'une telle régularisation ont d'abord été mis en évidence par plusieurs cas synthétiques. Il en est ressorti principalement que le choix d'un modèle *a priori* homogène semblait judicieux dans ce cas et que l'absence d'information sur le variogramme horizontal est un moindre mal. Les résultats d'inversion ont permis de déterminer l'extension du plume d'eau salée que ce soit latéralement, en profondeur ou en termes de contenu solide dissous (TDS). Ces observations sont en accord avec la situation hydrogéologique. Une comparaison avec les données de forage a montré que les résultats sont beaucoup plus satisfaisants qu'une régularisation traditionnelle par lissage du modèle (smoothness constraint). L'information *a priori* utilisée dans le processus d'inversion a permis d'améliorer la résolution, même si les outils traditionnels d'évaluation de la qualité de l'image ne sont pas capables de quantifier cette contribution.

Mots-clés : intrusion d'eau salée, côte belge, résistivité électrique, méthode électromagnétique, contrainte géostatistique, processus d'inversion, résolution.